Doctoral Dissertation
Doctoral Program in Civil and Environmental Engineering
(XXXV cycle)

Boundary heterogeneities in thermal convection: Urban Heat Islands and the Rayleigh-Bénard problem

by

Francesca Bassani

Supervisors:

Prof. Jost-Diedrich	Graf von Hardenberg	PoliTo
Prof. Davide	Poggi	PoliTo
Prof. Luca	Ridolfi	PoliTo
Dr. Valeria	Garbero	ARPA Piemonte
Dr. Massimo	Milelli	CIMA Foundation

Doctoral Examination Committee:

Carlo Camporeale	Politecnico di Torino
Gabriel Katul	Duke University
Antonio Parodi	CIMA Foundation
Paolo Perona	École Polytechnique Fédérale de Lausanne
Pietro Salizzoni	École Centrale de Lyon

Politecnico di Torino – 2023

Declaration

I hereby declare that the contents and organization of this dissertation constitute my own original work and do not compromise in any way the rights of third parties, including those relating to the security of personal data.

Francesca Bassani
2023

* This dissertation is presented in partial fulfillment of the requirements for **Ph.D. degree** in the Graduate School of Politecnico di Torino (ScuDo).

A babbo Paolo

Abstract

The widely studied topic of *thermal convection* has attracted the interest of the scientific community for centuries. In particular, the exploration of convective heat transfer in the field of environmental fluid dynamics is of key relevance for our Planet and humanity, due to the current critical times which are strongly affected by climate changes. Extreme and undesired events continue to influence our lives and risk to alter significantly the natural environment. Such phenomena are approached from multiple viewpoints, like numerical weather prediction and climate models, field campaigns and exploration of long climatic datasets. Actually, convective phenomena represent key processes which need to be better understood and sometimes better parameterized in numerical models. In this context, a remarkable and non-negligible aspect concerns the boundary conditions affecting such convective dynamics e.g., the geometrical and thermal complexity of an urban agglomeration or the different properties characterizing land and oceans.

Within a wide range of possible boundaries, this work focuses on a subset of particular boundary conditions involved in convection: thermal anomalies.

Cities represent a notable example of this situation. Actually, urban areas are characterized by different thermal properties with respect to the surrounding natural landscapes, due to their materials, geometry and human activities. The mutual action of those peculiarities make any city a thermal heterogeneity affecting the temperatures occurring in the area. Particularly, the urban air temperatures are warmer than the rural ones and this effect is known as Urban Heat Island (UHI). *Part I* of this thesis focuses on the definition, analysis and characterization of the UHI effect. One crucial existing gap in literature regards the identification of "urban" and "rural" meteorological sites to be used for UHI quantification, a problem which is still an open question. We develop a novel and as much as possible objective approach to face this problem. After establishing the definition, we capitalize the findings for a dual purpose. First, to fully characterize the effects produced by urban thermal heterogeneities with respect to their surrounding areas, in the specific case of the city of Turin, from a ground-level point of view and considering vertical atmospheric profile. Second, to validate a numerical weather prediction model which adopts a new urban parameterization, capable of capturing the UHI effect.

Part II of this work investigates what can be considered as an idealization of the subject of *Part I*: thermal anomalies applied on the boundaries of a Rayleigh-Bénard (RB) problem. Historically, its conceptual clearness has allowed scholars to widely explore its dynamics so far. Still, several issues remain open, e.g., the effects produced on the heat fluxes by non-homogeneous boundary conditions. Furthermore, the reduction of computational times in recent years has favoured the development of various modifications of the classical scheme, in which a fluid is confined between two plates kept at different temperatures. Our investigation on this topic is associated with the possibility to idealize hot spots like cities in a numerical system where ideally any configuration can be imposed at the boundaries. Thus, we evaluate the effects produced on convection by thermal heterogeneities, which we model through sinusoidal patterns set (i) in phase and (ii) in counter-phase between the top and the bottom plates. In the first case, the convection patterning results strongly affected by the boundary anomalies unless the scale of the perturbations is comparable to the natural scale of the system (i.e., under thermally-uniform boundaries). In the second case, the convection develops even if the two plates are characterized by a global null temperature difference. This counter-intuitive result is due to the alternation of purely convective zones and stable zones, where the bottom surface is cold while the top one is hot.

Contents

Abstract **v**

Introduction **3**

Part I – Urban Heat Islands **11**

1 The novel Mean Temperature Difference method to define urban-rural stations in UHI analysis **3**
1.1 Introduction . . . 3
1.2 The MTD metric . . . 5
1.3 Application to Turin, Italy . . . 7
1.3.1 Data and stations . . . 7
1.3.2 Results . . . 9
1.4 Discussion . . . 14
1.4.1 Applicability . . . 14
1.4.2 Comparison with other methods . . . 16
1.5 Conclusions . . . 19

2 Characterization of the Urban Heat and Dry Island effects in the Turin metropolitan area **21**
2.1 Introduction . . . 21
2.2 Area of study and data . . . 23
2.2.1 Near-surface instruments . . . 24
2.2.2 Radiometers for vertical measurements . . . 25
2.3 Ground-level analysis . . . 26
2.3.1 Temperature and Urban Heat Island . . . 26
2.3.2 Absolute Humidity and Urban Dry Island . . . 30
2.3.3 Influence of wind . . . 34
2.4 Vertical analysis and boundary layer Heat Island . . . 35
2.5 Conclusions . . . 40

3 Evaluating the urban canopy scheme TERRA_URB in the COSMO model for selected European

cities **43**
3.1 Introduction . . . 43
3.2 Model Description . . . 47
3.2.1 Surface-Layer Turbulence Scheme . . . 47
3.2.2 Land Surface Scheme TERRA . . . 48
3.3 Experiments . . . 51
3.4 Results . . . 55
3.4.1 Turin . . . 56
3.4.2 Naples and Moscow . . . 59
3.5 Conclusions . . . 61

Part II – The Rayleigh-Bénard problem **63**

4 Rayleigh-Bénard convection with thermal boundary inhomogeneities **65**
4.1 Introduction . . . 65
4.2 Numerical model . . . 66
4.2.1 Tested configurations . . . 67
4.3 Results . . . 67
4.3.1 3D . . . 67
4.3.2 2D . . . 72
4.3.3 Effects on the Nusselt number . . . 75
4.4 Conclusions . . . 75

5 Alternate convection arising in a 2D Rayleigh-Bénard system **77**
5.1 Introduction . . . 77
5.2 Model configuration . . . 79
5.3 Results . . . 80
5.4 Conclusions . . . 92

Conclusions **93**

Appendices **97**

A Appendix A: Supplementary material for Chapter 1 **99**
A.1 Duration of the period considered in the analysis . . . 99
A.2 Temporal resolution of the selected period . . . 100
A.3 Minimum number of stations . . . 101
A.4 Application of MTD to another domain: the city of Cuneo . 103

B Appendix B: Supplementary material for Chapter 2 **107**
B.1 Ground-level stations 108
B.2 Vertical profiles 112

C Appendix C: Supplementary material for Chapter 3 **115**
C.1 The "urban double-counting effect" 115
C.2 Characteristics of the stations used for model validation . . 116
C.3 Figures of Naples and Moscow domains 118

D Appendix D: Supplementary material for Chapter 4 **123**

References **131**

Introduction

When we think about convection, one of the first memories coming up to each person is probably related to some Science class, in which we learned that if a pot of water is boiled on a stove, fluid particles start moving up and down. Growing up, we have discovered that convection processes account for a large part of the environment around us and they strongly interact with our lives. In fact, convective motions are caused by the action of a force hard to ignore, the gravity, upon variations of density in a fluid [1]. Plenty of phenomena and motions of the fluid systems in the known universe result from convection, especially regarding fluids very familiar to us: water and air, among the key elements of the nature surrounding us.

Albeit changes in a fluid's density may be caused by several factors – leading to different types of convection (e.g., electroconvection [2]) – here the focus is on *convective heat transfer*, or *thermal convection* (hereinafter simply referred as convection). This is the topic where the notions of heat transfer and fluid mechanics intertwine to study how flow fluid responds to changes in temperature (density) [3].

For instance, for boiling water in a pot, the colder (and denser) water on top is pulled down by gravity and falls, while the hotter less dense water rises up and takes its place (Fig. 1a). Another example, most likely not as in everyday life as the boiling pot, is a hot air balloon, which is lifted by the hotter air fueled at its base (also thanks to the Archimedes' principle). The heated air molecules move upward and get trapped inside the balloon, while the cool air is pushed downward, causing the balloon to rise up further (Fig. 1b).

Generally speaking, nature is rich of flows driven by temperature differences. From astrophysics to geophysics, from oceans to atmosphere circulations, thermal convection embodies the challenging and continuous understanding of the natural environment that has always fascinated researchers.

Astrophysical occurrences include stellar interiors [4, 5], gaseous giant planets [6] and the outer layer of the Sun [7] (e.g., Fig. 1c). Closer to home, we find examples of geophysical occurrences in the Earth's outer core [8, 9] and in mantle convection [10, 11]; regarding the oceans, examples include the open oceanic convection [12], the thermohaline circulation [13] and sea breezes [14] (Fig. 1d).

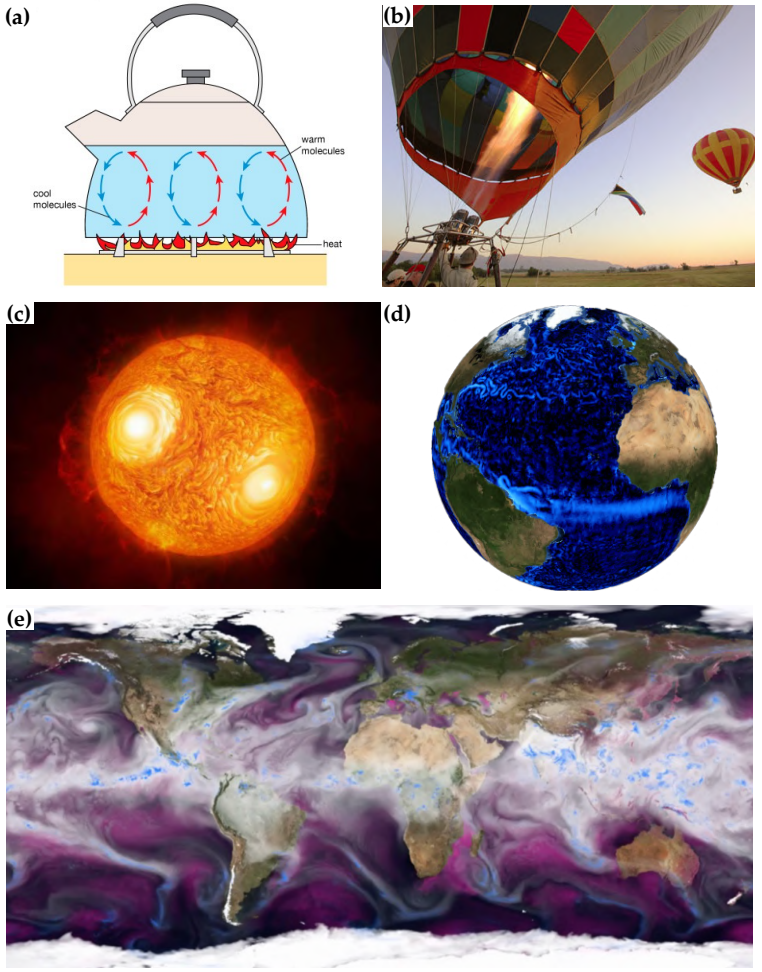

Figure 1: Examples of convection. **(a)** Boiling water (© Enciclopædia Britannica, Inc.). **(b)** Hot air balloon (© Patrick Beaudry). **(c)** The red star Antares' convection currents (© ESO/M. Kornmesser). **(d)** Simulated high-resolution ocean-surface circulations (from ESA). **(e)** Large-scale atmospheric circulation (Mats Bentsen © 2015 BCCR/ECMWF/-NASA/MET Norway).

As regards the atmospheric circulation, it is fair to say that mankind's will to understand it originated in Archimedes' times. The motions of the atmosphere have always intrigued scholars worldwide, not only because of their challenging mathematical framework, but also because they interact with so many environmental processes and fields, including air pollution, hydrology, agricultural-aeronautical-mesoscale meteorology, weather forecasting,

climatology [15] and nowadays the bursting topic of climate change.

By mentioning these examples, it emerges that such a widely investigated topic and the phenomena closely related to it deal with an entire spectrum of scales [1], ranging from the smaller eddies of turbulence (i.e., within the atmospheric boundary layer and clouds) to the larger planetary scales (Fig. 1e).

Regardless of the subject area and of the scales of interest, convective heat transfer is often affected by thermal heterogeneities at the boundaries, which play a key role on the way convection develops in natural systems. Thermal heterogeneities may be caused by geometrical, physical and/or dynamical factors and therefore their occurrence – at every scale and in different fields – has been extensively explored. For instance, either the different thermal properties characterizing land and oceans, as well as the topography of the surface, do strongly affect both the formation and the occurrence of atmospheric circulations [16]. This is a crucial topic in terms of weather forecasting and prediction of extreme events [17].

Other contributions have investigated the effects produced by thermal heterogeneities on porous media [18] – which are essential to deal with geological strata, nuclear waste disposal, geothermal reservoirs, and the storage of heat-generating materials [19].

Another example deals with mantle convection, where the study of thermal heterogeneities is of great relevance for a better understanding of the dynamics of the tectonic plates and the volcanic eruptions (e.g., [20–22]).

Albeit the relevance of the topic, there still are several unresolved points and open questions, in particular regarding the impact of thermal heterogeneities on environmental issues. E.g., the non-trivial identification of the conditions affecting extreme storms and rainfalls that can lead to large hail or tornadoes [23], or the choice of the proper thermodynamic conditions to cope with turbulent pipe flows at supercritical pressure, concerning the ongoing dual threats of climate change and ozone depletion [24, 25].

In the context of environmental fluid dynamics, the current work focuses on other two crucial aspects of thermal convection with non-homogeneous boundaries – that compose *Part I* and *Part II* of this thesis – by addressing and trying to disentangle some existing gaps, which are explained in the following.

The first increasingly significant issue deals with one of the most common and typical example of thermal heterogeneities affecting the convection around us: cities. Increasing attention is being devoted to this topic because

of its huge relevance for our Planet and its population: we build and shape the cities in which we live, work and operate, we influence them with our movements and actions and, in turn, they greatly influence the climate. Cities are the most inhabited places of Earth: nowadays, more than the 55% of the world's population lives in urban areas, a proportion that – according to the World Urbanization Prospects provided by the United Nations [26] – is expected to increase to 68% by 2050. Furthermore, being the cities among the most evident examples of the human modifications on Earth, with their great contribution to changes of atmospheric compositions and climate, it is becoming more and more important to understand, describe, model and possibly predict the impact of urban environments on (i) undesired, extreme natural events, (ii) all the man-made infrastructures and (iii) the health and comfort of populations.

Within this scenario, cities are a fascinating example of thermal heterogeneities affecting atmospheric circulation. Actually, urban areas are characterized by complex geometries (buildings, roads, urban canyons, etc.) and surfaces with a greater thermal inertia than the surrounding rural lands [27]; the joint action of these factors, combined with the anthropogenic heat emissions and the human activities, well summarize that urban environments are hot spots which greatly influence the convection of the overlying atmosphere, namely the atmospheric boundary layer. The idea that a city can be seen as a thermal heterogeneity with respect to its nearby natural environment was already in the thoughts of Luke Howard, the first who provided evidence that air temperatures are higher in a city than in its surrounding countryside [28]. From that time on, this phenomenon has been addressed as "Urban Heat Island" effect, or simply UHI, and has been considerably studied worldwide, over a broad selection of cities and areas in the five inhabited continents (e.g., Hongkong, China [29], Kampala, Uganda, [30], Melbourne, Australia [31], Montreal, Canada [32], London, England [33]).

In the long existing literature on this topic, the UHI effect has been commonly quantified as the difference between urban and rural air temperatures, referring to pairs of urban and rural measurement sites [34–36]. It is clear that such difference is crucial in determining the UHI intensity and requires an accurate selection of which stations can be defined "urban" and "rural". Despite the multitude of researches on the Urban Heat Island phenomenon, this distinction is still a subject of unresolved debate, which has obvious consequences on the assessment of the UHI effect. Thus, we highlight diagnosis problems referring to its definition and quantification,

which need to be addressed and clarified.

These matters are examined in detail in *Part I* of this thesis. A novel and objective method is proposed to overcome the difficulties related to the definition of urban and rural stations. Once the definition is established, two case studies over the city of Turin are presented to characterize the effective impacts of such a thermal heterogeneity on the territory and the atmosphere, through (i) a data-based approach and (ii) numerical simulations.

The second topic examined in this work – covered in *Part II* – concerns one of the simplest, most explored and paradigmatic models of convection: the Rayleigh-Bénard (RB) problem, after the theory of Lord Rayleigh [37] and the experiments of Henri Bénard [38]. The classical RB system involves an incompressible fluid between two horizontal, rigid plates kept at fixed temperatures, where the bottom layer is hotter than the top one (therefore, convective motions start). The study of such configuration has attracted large interest to scholars so far and its main interest is of theoretical nature: in fact, during the evolution from the stationary state to the fully developed turbulent regime, RB convection shows a rich scenario of different structures. Furthermore, the problem is of practical importance for many engineering applications and natural phenomena [39].

It has to be said that, despite the noticeable advances of the past decades in the reduction of computational times, the effects of non homogeneous boundaries on both plates seem not to have attracted the attention of researchers so far. By addressing this topic, the present work tries to fill that gap in literature. In particular, the classical RB scheme is numerically studied by introducing a quite novel modification of the boundary conditions: they are no longer thermally uniform as in the standard model, but undergo thermal anomalies. Here, they are simulated by sinusoidal waves and the considered fluid is air.

The investigation of the effects induced by the boundary thermal inhomogeneities is positioned between the large-scale structures emerging from turbulent convection [40] and the possibility to idealize some complex features of the real world, such as urban agglomerations. In fact, in a thermally uniform RB configuration, the large-scale structures are known to cluster together and form specific patterns characterized by similar high or low temperatures and by typical wavelengths [41]. Understanding if and how the thermal heterogeneities impact such clustering phenomenon is not only of theoretical interest, but could also be useful to generalize the effects produced by hotter and colder boundaries in the atmospheric environment.

Actually, in the context of the present work, it is important to notice the parallelism existing between the hot spots represented by cities with respect to the rural surroundings (due to the UHI effect) and the clustering phenomenon of thermal plumes (in RB simulations). Let us imagine to be on top of a tower or a skyscraper and to look down onto a hypothetical city: depending on its architecture, the view will portray the alternating phases between buildings and streets, that is usually referred as urban canyons. If we consider a larger scale, e.g., moving the observer from a skyscraper to an airplane or even higher, those features will be no more recognizable and the picture will be about several and separate agglomerations of urban areas (cities) spaced by some rural lands. Indeed, both examples are nothing but thermal heterogeneities that affect the corresponding scales. At the scale of urban canyons, the heating of the surface undergoes a complex spatial pattern mainly due to the geometry, radiative and thermal properties of surface facets [27]. This greatly influences the intra-urban variability of temperatures. At the larger scale, where cities and natural lands alternate, the spatial heterogeneity is reflected in clear differences between the urbanized and the non-urbanized areas. The main ones are: geometric properties, openness to the sunlight and sky, radiative properties (e.g., albedo and emissivity of the different impervious and natural surfaces), thermal properties (thermal conductivity and admittance), soil moisture and aerodynamic properties, such as the roughness length and the shelter from wind. Thus, differences between these properties in urban and rural areas underline different urban and rural temperatures, which are clearly reflected on the overlying air.

Figure 2 shows a schematic representation of the bridge which connects *Part I* and *Part II* of this thesis: the thermal heterogeneities studied through the Urban Heat Island phenomenon can be idealized as the thermal anomalies imposed at the boundaries of a Rayleigh-Bénard model.

To sum up, albeit from distinct perspectives and approaches, the two main themes addressed in this work concern the impact of thermal heterogeneities on the convection over air and – as will be discussed and clarified along the manuscript – they share common features in terms of clusters of hot air masses.

As a consequence, the two parts into which the thesis is divided are straightforward.

Part I includes Chapter 1, 2 and 3 and it deals with the Urban Heat Island effect, caused by a city that represents a heterogeneity with respect to its natural surroundings. Thanks to the availability of one of the most dense

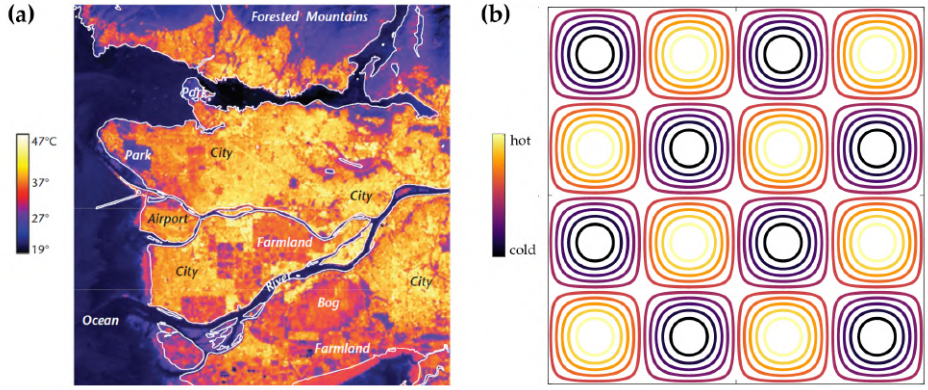

Figure 2: **(a)** Thermal images of surface brightness temperature for Vancouver, Canada, at daytime (September 3, 2010), showing the different temperatures between cities, its suburbs and the surrounding farmlands (Source: © Oke et al. (2017), chapter 7 [27]). **(b)** Schematic representation (with isotherms) of sinusoidal temperature patterns imposed on one boundary of a 3D Rayleigh-Bénard scheme.

meteorological networks of Italy, namely the weather stations of ARPA Piemonte, this topic has been investigated through an extensive data-based approach.

Chapter 1 develops a new method to identify urban and rural stations needed in the Urban Heat Island analysis.

Chapter 2 applies the findings of Chapter 1 to characterize in detail the UHI of Turin, both at the ground-level and up to the boundary layer height.

Chapter 3 originates from a collaboration between ARPA Piemonte and the Consortium for Small-scale Modeling (COSMO) [42]. In the context of UHI investigation, our contribution helped the members of the Consortium to validate the new urban parameterization TERRA_URB recently implemented in the Numerical Weather Prediction model COSMO, by adopting meteorological data from Turin.

Part II, including Chapter 4 and 5, regards the investigation of Rayleigh-Bénard convection under non-homogeneous thermal boundary conditions.

Chapter 4 deals with a systematic analysis of nonuniform temperature conditions, simulated by changing the wavelengths of sinusoidal perturbations, both in 3D and in 2D horizontally-periodic domains of different aspect ratios. Either no-slip and free-slip velocity boundary conditions are explored to fully characterize the phenomena.

Chapter 5 introduces a 2D model where alternating boxes of convection

and conduction coexist. Differently from the standard RB convection, which is triggered by a temperature gradient between the two plates, the model analyzed in this Chapter involves a global zero thermal difference characterizing the bottom and top surfaces. Our preliminary results show that horizontal and vertical motions still occur due to the particular anomalies imposed at the boundaries.

Apart from Chapter 5, for which a scientific article is in preparation, Chapters 1 to 4 are partially derived from our peer-reviewed publications.

Part I

Urban Heat Islands

1

The novel Mean Temperature Difference method to define urban-rural stations in UHI analysis

The work presented in this chapter has been partially derived from Bassani et al. (2022) [43].

1.1 Introduction

The meteorological phenomenon known as Urban Heat Island (UHI) is one of the main effects produced by increasing urbanization [44, 45] and a significant example of anthropogenic climate modification [46]. UHI refers to the warmer temperatures experienced by a city with respect to its rural surrounding area, mainly due to the different thermal properties between urbanized and natural lands, anthropogenic heat emissions, human-induced pollution and limited wind blowing among buildings [34, 47, 48]. In the long and well-documented urban heat island literature [35], UHI has been commonly quantified as the difference, in terms of air temperatures, between pairs of urban and rural measurement sites [34, 36] or between a spatial average of several urban and/or several rural stations [49]. This difference is crucial in determining the UHI intensity and requires choosing a non trivial definition of which stations are "urban" and "rural". In his work, Stewart (2007) highlighted the difficulty in the definition of the urban-rural dichotomy, because the demarcation between "urban" and "rural" is artificial and many relevant local-scale aspects should be taken into account [50]. Recent studies tried to address this critical issue by proposing new methods that (i) highlight different thermal behaviors in urban-rural pairs – e.g., the approaches based on the thermal day-to-day variation [51–56] or the mean daily excursion [57] – or (ii) identify the stations called "peri-urban", i.e. those located close to the urban-rural interface, by focusing on the

day-to-day warm and cold transitions [58].

Another important approach to classify the stations is the Local Climate Zones (LCZs) Classification System proposed by Stewart&Oke (2012) [59]. By using criteria concerning aspects that control the local surface climates, this climate-based tool classifies the landscape (i.e., a local-scale area of land) in 17 regions characterized by uniform surface cover, structure, material and human activity. The classification covers both built and natural environments and each zone is characterized by a distinctive near-surface temperature regime.

Despite the variety of methods, a key point is that all of them need a preliminary classification of the stations. In order to overcome this possible source of arbitrariness, a novel method, called the "Mean Temperature Difference" (hereinafter MTD) is proposed. The MTD is a data-based approach aiming to recognize and differentiate the thermal behavior of the urban context with respect to its surrounding less populated area. The former is different – in terms of thermal response – from the latter, mainly because of its predominantly impervious land cover type and the presence of sheltering constructions, which trap heat during the day and release it during the night resulting in higher night-time temperatures.

The strength of the proposed MTD method is the capability to objectively identify these different thermal behaviors, without assuming *a priori* which sites pertain to the urban and rural categories. In this sense, the MTD approach can complete and be of support to the Local Climate Zones Classification. In fact, as stated by Stewart&Oke (2012) [59], the intention of the LCZs is not to supplant the categories "urban" and "rural" in the heat island issues, but to provide a more conscious and constrained use of these categories when describing the local conditions of the stations.

Starting from a group of stations – heterogeneous in terms of LCZs – and adopting the Principal Component Analysis [60] as a clustering method, the proposed approach is able to objectively and clearly identify the different thermal behavior of the stations. It allows a clear distinction of what is the typical "urban" pattern, the different "rural" one and also what does not fall into either categories. No choice about whether a site is "urban" or "rural" is made *a priori* and no parameters to calibrate enter the procedure, so that its results are clear, immediate and easy to apply. This makes the method objective, totally data-based and unrelated to any preliminary landscape classification.

To show the features of the proposed method, it is applied it to the city of Turin (Italy) and its surrounding area, which is characterized by a quite

complex morphology (orographic and hydrographic heterogeneity, different land uses, etc.), making it suitable to test the proposed metric.

The present chapter is organized as follows. Section 1.2 describes the MTD metric. Section 1.3 reports the results of the application of the proposed method to Turin area. In Section 1.4 the applicability of the MTD and its comparison with existing methods to select proper urban-rural pairs are discussed. Finally, some conclusions are drawn.

1.2 The MTD metric

The idea behind the MTD metric is to detect similar behaviors among stations and it is based on two main steps: (i) the evaluation of a metric characterizing the thermal behavior of each measurement site, and (ii) the adoption of the Principal Component Analysis [61, 62], in order to capture common performances of such metric and to cluster the stations into distinct groups.

In the following, the first step is described. The variable considered for each weather station S is the monthly-averaged hourly temperature $T^S_{i,M}$, where subscripts $i = 1, 2, .., 24$ and $M = Jan, Feb, ..., Dec$ refer to the hours and months, respectively. For example, the monthly temperature value at 01:00 hours for January (i.e., $T^S_{1,Jan}$) refers to the climatological average over all years of all the temperatures of January registered at 01:00. The metric MTD is defined, for each hour i, each month M and each station S, as:

$$\mathrm{MTD}^S_{i,M} = T^S_{i,M} - \overline{T^S_{i,M}} - \langle T^S_{i,M} - \overline{T^S_{i,M}} \rangle \tag{1.1}$$

in which the overbar refers to a temporal average over all months and hours of $T^S_{i,M}$, and $\langle \cdot \rangle$ represents the spatial mean among all stations included in the study area (i.e., $\langle \cdot \rangle = \sum_j (T_{i,M})_j / N_S$, where j ranges from 1 to the number of stations N_S). The first two terms at the right-hand side of Eq. (1.1) define the anomaly of temperatures at each hour and month compared to their temporal average for that station. The last two terms remove the mean anomaly across all stations for that hour and month. Positive values of MTD indicate that the station S, at a certain hour and month, is characterized by higher air temperature anomalies than the mean of the other stations, while the opposite occurs for negative MTD.

In the second step of the proposed method, the MTD values are organized in a matrix to which the Principal Component Analysis (PCA) is applied. The matrix (hereinafter **MTD**) has dimensions 288xN_S: its rows contain the values $\mathrm{MTD}_{i,M}$ corresponding to the 24 hours for every month (24x12=288),

and each column refers to a station S: therefore, **MTD** defines a cloud of 288 points in a N_S-dimensional space. PCA is commonly used in the atmospheric science and it is considered a robust tool in climatology and meteorology (e.g., [63–65]). As described by Wilks (2011) [62], this mathematical technique aims at reducing the dimensionality of a large set of data to another data set, which contains a linear combination of the original variables. The analysis can be conducted on the correlation matrix or on the covariance matrix. PCA applied to the correlation matrix weights all the standardized variables equally, because all have variance equal to the unity; instead, the analysis on the covariance matrix emphasizes the principal components having the largest variances [62]. Therefore, PCA is performed on the covariance matrix of **MTD** so that the information about the variance is included in the clustering of stations. PCA arranges the original dimensions of the data matrix **MTD** onto a new orthogonal space, such that the new axes are oriented in the directions explaining largest variance in the data. These new directions are called principal components and they are chosen in such a way that the greatest variance of the data lies along the first direction (namely, the first principal component), the second greatest variance on the second direction, and so on. The principal components correspond to the eigenvectors of the covariance matrix of **MTD**, while the eigenvalues are a proxy of the variance explained along each principal direction. It follows that, ordering the eigenvalues in descending order from largest to smallest, it is likely that the subspace mapped by the first m principal directions explains most of the variability of the data contained in the **MTD** matrix. That is, it is sufficient to consider this m-dimensional subspace to describe the main features of the original N_S-dimensional space. The quality of the description provided by the m-th subspace can be assessed by comparing the sum of the m eigenvalues – corresponding to the m eigenvectors considered – and the cumulated variance explained by all the eigenvectors, computed as the sum of all eigenvalues. Typically, in the present application the first two principal components (i.e., m=2) were sufficient to describe the thermal behavior of the stations, allowing to cluster them on a simple plane. As a consequence, the interpretation of the analysis is straightforward and objective.

1.3 Application to Turin, Italy

1.3.1 Data and stations

Turin is located in the North-West region of Italy, centered at latitude 45.071 N and longitude 7.687 E. The metropolitan area of Turin has a population of almost 1.5 million inhabitants, covering an area of about 600 km^2. The city is at about 100 km (air distance) far from the highest peak of the Alps, at a mean elevation above the sea level of 250 meters and it is surrounded by hills up to 600 m high in the Eastern sector, as shown in Fig. 1.1a.

The Po river flows in the South-East of the city and separates the most urbanized area, which is mainly located on the western bank of the river, from the hills in the East (see Fig. 1.1a). The Köppen Climate Classification [68] puts Turin into the Humid Subtropical Climate, namely Cfa (C = warm temperature, f = fully humid, a = hot summer). According to this, the climate in Turin is warm and temperate with significant rainfall all over the year. The 11 stations considered in the analysis (see Tab. 1.1) provide hourly near-surface temperature data. They belong to the network of the Regional Agency for the Protection of the Environment of Piedmont Region (Arpa Piemonte) and are distributed around the city of Turin, with about 20km as maximum distance from the city center (see Fig. 1.1a). For this study, the selected stations are chosen on the basis of the longest temporal series available, from January 1^{st}, 2007 to December 31^{st}, 2020 (14 years).

Table 1.1: Weather stations for the temperature measurements used in the analysis, sorted alphabetically by their short names, with lat-lon coordinates in decimal degrees, elevation above the sea level (a.s.l., meters) and Local Climate Zones types and definitions (from [59]).

Station name	Station short name	Lat (N)	Lon (E)	Elevation (m a.s.l.)	LCZ type and definition
Consolata	*LCZ2con*	45.0758	7.6783	290	2: Compact midrise
Rivoli	*LCZ6riv*	45.0800	7.4989	362	6: Open low-rise
Alenia	*LCZ8ale*	45.0797	7.6108	320	8: Large low-rise
Vallere	*LCZ8val*	45.0181	7.6750	239	8: Large low-rise
Venaria Ceronda	*LCZ8vec*	45.1353	7.6325	253	8: Large low-rise
Reiss Romoli	*LCZ8rer*	45.1125	7.6708	270	8: Large low-rise
Santena-Banna	*LCZBsan*	44.9447	7.7819	238	B: Scattered trees
Venaria La Mandria	*LCZBvem*	45.1750	7.5592	337	B: Scattered trees
Bauducchi	*LCZDbau*	44.9610	7.7086	226	D: Low plants
Carmagnola	*LCZDcar*	44.8861	7.6861	232	D: Low plants
Caselle	*LCZDcas*	45.1856	7.6508	300	D: Low plants

According to the Local Climate Zones (LCZ) map (see Fig. 1.1b), provided for Europe at 100m spatial resolution by Demuzere et al. (2020)

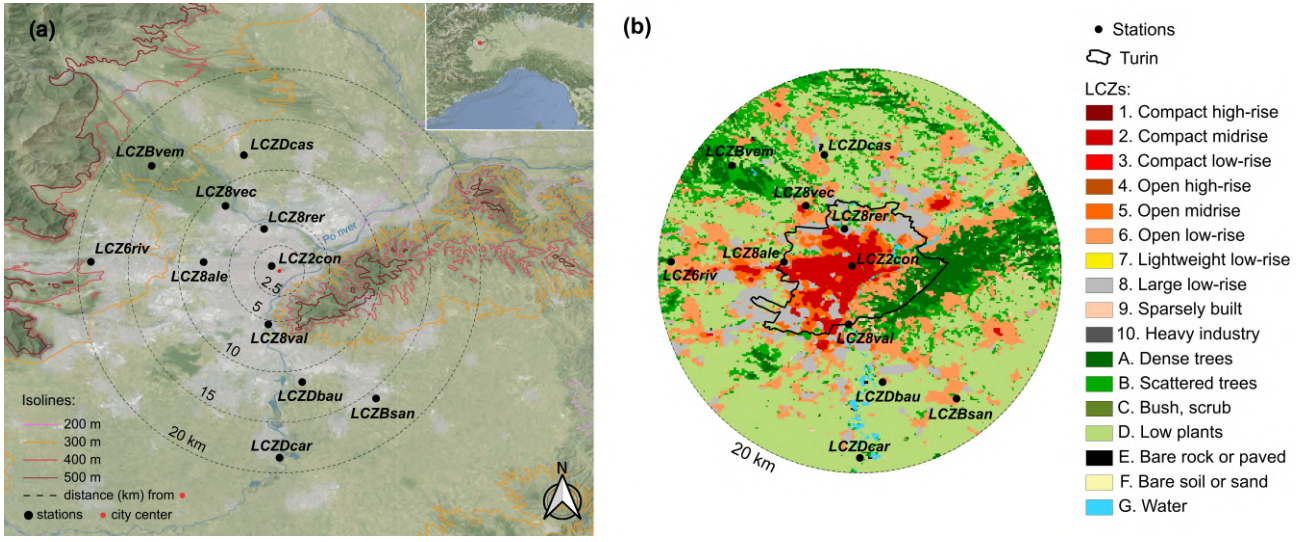

Figure 1.1: Panel **(a)**: terrain map of the metropolitan area of Turin (North-West of Italy, in the inset), with the principal rivers highlighted in blue and the urbanized area represented in gray. The distance in kilometers of each weather station (black dots) from the city center (red dot, Piazza Castello: lat 45.071 N, lon 7.687 E) is marked with the black dashed isolines, while the colored continuous isolines indicate the elevation above the sea level (meters). Panel **(b)**: LCZ map of the studied area, from [66] (WUDAPT database, [67]).

[66, 69] (WUDAPT database, [67]), six stations fall under the "Built types" category of [59]: Consolata (*LCZ2con*), Rivoli (*LCZ6riv*), Alenia (*LCZ8ale*), Vallere (*LCZ8val*), Venaria Ceronda (*LCZ8vec*) and Reiss Romoli (*LCZ8rer*). The stations of Santena-Banna (*LCZBsan*), Venaria La Mandria (*LCZBvem*), Bauducchi (*LCZDbau*), Carmagnola (*LCZDcar*) and Caselle (*LCZDcas*) are categorized as "Land cover types" by Stewart&Oke (2012) [59], as shown in Tab. 1.1.

However, the LCZ classification is sometimes the result of unsupervised choices and may lead to assignments which not always match the analysts' expertise. In the following section, the stations are reexamined in light of the MTD approach. It emerges that sometimes the LCZs are too local to fully characterize the thermal behavior of the sites and do not consider the effects induced by local surrounding conditions or the large-scale context around a station, e.g., the distance to the city center or the proximity to the reliefs.

1.3.2 Results

The MTD patterns obtained from Eq. (1.1) are shown in Fig. 1.2. The emerging patterns already feature common behavior among groups of stations at a first glimpse. Firstly, three stations – Consolata (*LCZ2con*), Reiss Romoli (*LCZ8rer*) and Alenia (*LCZ8ale*) – show a central cold area, characterized by negative MTD values during daytime, while at night hours the temperature anomalies are positive (see the first row of Fig. 1.2). Secondly, the stations Caselle (*LCZDcas*), Rivoli (*LCZ6riv*) and Vallere (*LCZ8val*), displayed in the second row of Fig. 1.2, do not show a well defined hot/-cold blob. Finally, in the remaining panels of Venaria Ceronda (*LCZ8vec*), Venaria La Mandria (*LCZBvem*), Bauducchi (*LCZDbau*), Santena-Banna (*LCZBsan*) and Carmagnola (*LCZDcar*) an inverse pattern clearly emerges, characterized by positive MTD values during daytime and negative ones during night times.

Figure 1.3 shows the results of the applications of the Principal Component Analysis to the **MTD** matrix, allowing the different behaviors of the stations to be distinguished. As described in Section 1.2, the first two principal components clearly emerge. In Fig. 1.3a the percentage of the explained variance is plotted on the left y-axis, while its cumulative values are represented as the right ordinate. The first two principal components (p.c.) explain most of the variance in the data (about $\simeq 92\%$) and so they are sufficient to cluster the stations: in particular, the first p.c. accounts for $\simeq 74\%$, while the second p.c. for about 18%. The projection of each station

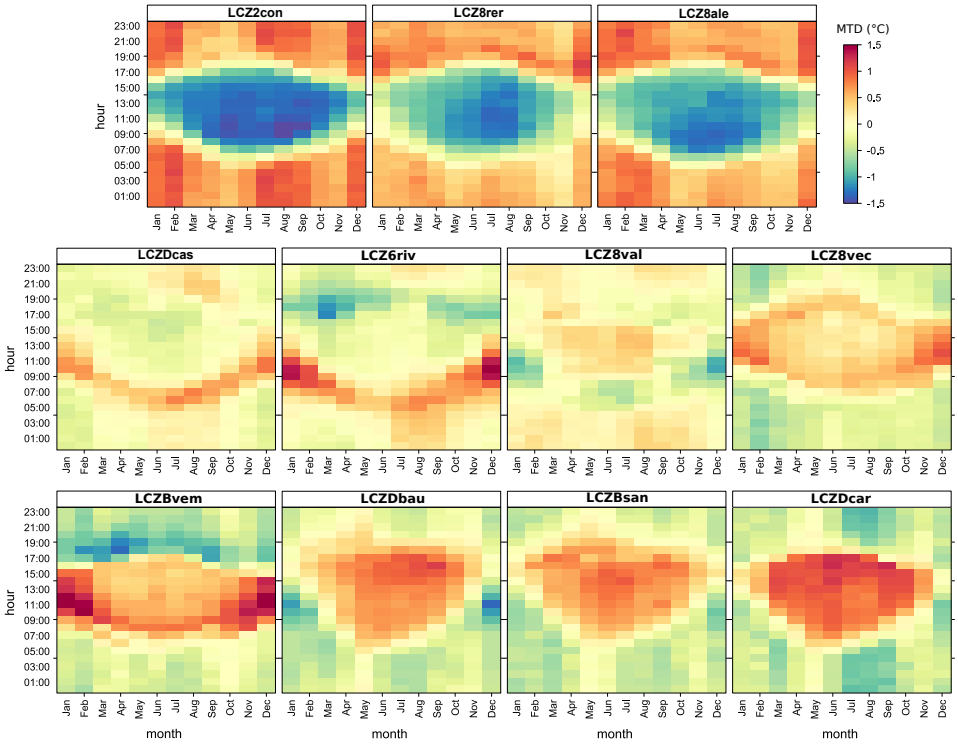

Figure 1.2: Mean Temperature Difference (MTD): each panel, labeled with the short name associated to each weather station S, represents the $\mathrm{MTD}^{S}_{i,M}$ computed with Eq. 1.1 (hours i are reported on the y-axis and months M on the x-axis).

onto the first and the second principal components are reported along the x- and y-axis of Fig. 1.3b, respectively.

The physical meaning of these principal components is clear looking at panels (c) and (d) of Fig. 1.3, showing the two signals. Let us focus on the signal described by the first principal component (Fig. 1.3c). It is characterized by negative temperature anomalies during daytime hours and positive ones during evening and night. This is the typical pattern embedded in the Urban Heat Island phenomenon: in the morning and early-afternoon, the UHI is low and can even become negative in some cases [70], resulting in the so-called daytime Urban Cool Island [71]. Then, when the solar radiation decreases, the urban area retains more heat and cools more slowly than the rural surroundings [72], resulting in positive anomalies of temperatures. We deduce from this pattern that the first principal component – which corresponds to the highest eigenvalue ($\simeq 74\%$ of explained variance) – refers to the most evident characteristic differentiating

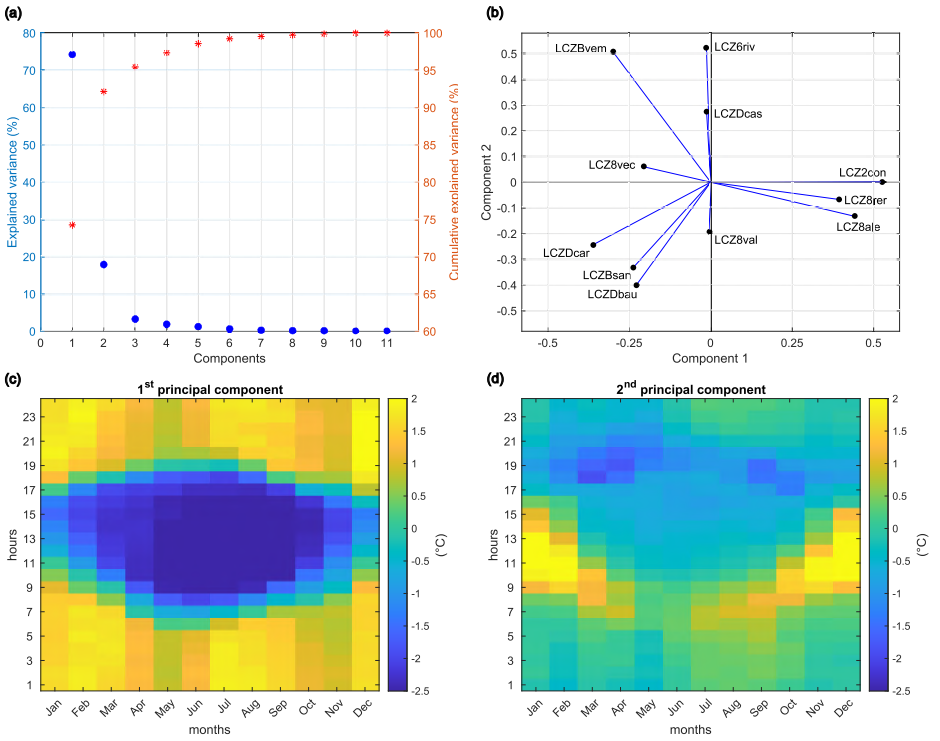

Figure 1.3: PCA on the matrix **MTD**: **(a)** percentage of explained variance for each of the 11 components (blue dots, left axis) and their cumulative values (red asterisks, right axis); **(b)** space of the first (x-axis) and second (y-axis) principal components; **(c)**,**(d)** representation of the two principal components of the MTD (color scales in degrees Celsius).

the stations: urban vs. rural thermal behavior. The projection of each station onto the first principal component (x-axis of Fig. 1.3b), either it is positive or negative, determines whether a site is characterized by one or the other thermal behavior: the stations of Consolata (*LCZ2con*), Reiss Romoli (*LCZ8rer*) and Alenia (*LCZ8ale*) are characterized by substantially positive values, while negative projections correspond to Venaria La Mandria (*LCZBvem*), Venaria Ceronda (*LCZ8vec*), Carmagnola (*LCZDcar*), Santena-Banna (*LCZBsan*) and Bauducchi (*LCZDbau*). Instead, an almost null projection onto the first p.c. means that the thermal behavior cannot be assigned to urban or rural patterns. This is the case of Rivoli (*LCZ6riv*), Caselle (*LCZDcas*) and Vallere (*LCZ8val*).

The general pattern described by the first p.c. (Fig. 1.3c) can be made station-specific by multiplying it by the projection of the station of

interest onto the first principal component, thanks to the fact that the principal components form an orthonormal base. As an example, consider two stations characterized by a positive and a negative projection onto the first p.c., namely Consolata (*LCZ2con*, positive) and Carmagnola (*LCZDcar*, negative), and examine one temporal slot, e.g., 01UTC in January. We define $E^{PC}_{i,M}$ as the value corresponding to the considered instant in time (hour $i = 1$ and month $M = Jan$), derived from the representation of the first principal component ($PC = 1$) in Fig. 1.3c: $E^{PC=1}_{1,Jan} = 1.63$. The value of the projection of Consolata onto the first principal component is 0.54 (see Fig. 1.3b). The MTD associated with this station is $\mathrm{MTD}^{LCZ2con}_{1,Jan} = 0.90°\mathrm{C}$ (see panel *LCZ2con* in Fig. 1.2), and it can be obtained by multiplying $E^{1}_{1,Jan}$ by 0.54: $\mathrm{MTD}^{LCZ2con}_{1,Jan} \simeq 1.63 \cdot 0.54 = 0.88°\mathrm{C}$. The centesimal digits missing for obtaining the exact value 0.90°C (in Fig. 1.2) derive from the additional contribution of the other principal components. To sum up, at 01UTC in January the temperature at Consolata is $\simeq 0.90°\mathrm{C}$ warmer than the average of all other stations. This behavior reflects the UHI effect and it is mainly due to the urban characteristics of this site, which is confirmed also by its LCZ class. Instead, the station of Carmagnola is characterized by a negative projection onto the first principal component, equal to -0.35 (Fig. 1.3b): $\mathrm{MTD}^{LCZDcar}_{1,Jan} \simeq 1.63 \cdot (-0.35) = -0.57°\mathrm{C}$. As above, a good approximation of the actual $\mathrm{MTD}^{LCZDcar}_{1,Jan} = -0.38°\mathrm{C}$ displayed in Fig. 1.2 would be obtained adding $E^{2}_{1,Jan} \cdot (-0.25)$, where (-0.25) is the projection of Carmagnola onto the second principal component (Fig. 1.3b).

The previous example shows that the correspondence between the projection of the stations onto the first principal component and their thermal pattern is very clear. A first group, characterized by positive projections (*LCZ2con*, *LCZ8rer* and *LCZ8ale*), resembles exactly the signal shown in Fig. 1.3c, where warmer temperatures are experienced during night. Therefore, its thermal behavior is associated with a typical urban pattern in the UHI effect, as already discussed by [57] and [73]. The LCZ-based classification assigned to the stations belonging to this group confirms these findings, since the combined effect of buildings and the mostly paved surface cover – typical of LCZ classes number 2 and 8 – greatly influences the surface energy and radiation balance [74].

A second group of stations exhibits the opposite temperature pattern with respect to the one shown in Fig. 1.3c, having a negative projection onto the first p.c.: *LCZBvem*, *LCZ8vec*, *LCZDcar*, *LCZBsan* and *LCZDbau*. We associate this thermal pattern with the rural surroundings of the city, characterized by colder temperatures during the night and by higher early

morning heating rate than over the city [71, 75]. As before, some considerations can be drawn in light of the LCZs assignment. In agreement with the authors' expertise, the described rural thermal pattern is coherent with the land cover types B (scattered trees) and D (low plants) associated with the stations of Santena-Banna (*LCZBsan*), Venaria La Mandria (*LCZBvem*), Bauducchi (*LCZDbau*) and Carmagnola (*LCZDcar*). Note that *LCZBsan*, *LCZDbau* and *LCZDcar* were adopted as rural stations also in [57] and [73]. However, the LCZs assignment of Venaria Ceronda (*LCZ8vec*), namely the "Large low-rise" built type, seems too local to fully characterize its rural thermal pattern emerging from PCA. Actually, the LCZ class number 8 would relate this station to a mostly paved surface with few or no trees, but the PCA shows that its thermal behavior is instead more aligned with the rural class.

Figure 1.3b also shows that the projection onto the first principal component is almost zero for *LCZ6riv*, *LCZDcas* and *LCZ8val*. This means that for these three stations the contribution of the first principal component ($E_{i,M}^{PC=1}$) weights less than the second p.c. and, therefore, the signal characterizing these sites looks like panel (d) of Fig. 1.3. Before focusing on the meaning behind the second principal component, the near-absence of the projection onto the first principal component in *LCZ6riv*, *LCZDcas* and *LCZ8val* reveals that Rivoli, Caselle and Vallere exhibit an intermediate thermal behavior with respect to the other stations characterized by substantially positive or negative projections. Note that this intermediate behavior is not necessarily homogeneous among these stations. PCA only highlights that their thermal pattern differs from all other sites characterized by positive or negative projections and, therefore, these three stations should be considered carefully for UHI studies. It is also important to point out that also the LCZs assignment for *LCZ6riv*, *LCZDcas* and *LCZ8val* is questionable and appears too local to take into account the real conditions affecting the temperatures measured by the sensors. The site of Rivoli (*LCZ6riv*) is designated as "Open low-rise" built type, but its thermal behavior is not classified as urban by the PCA probably because of the proximity to the reliefs and the distance from the city of Turin. Caselle station (*LCZDcas*) is assigned to the "low plants" land cover type D, but the PCA does not classifies it as rural. Actually, *LCZDcas* is located in the perimeter area of an airport, at about 200 m from the airstrip and only 600 m far from the closest town and the effective presence of low plants is true in the immediate surroundings of the site only. Finally, the "Large low-rise" built type associated with the station of Vallere (*LCZ8val*) does

not show an urban thermal behavior, because it is located close to a park. Therefore, the LCZs assignments are not always able to clearly distinguish the urban and rural thermal patterns, since we observed that same LCZ type corresponds in some cases to different thermal behaviors.

Let now focus on the signal described by the second principal component (Fig. 1.3d), which explains about the 18% of the total variance and captures other aspects (with respect to the first component) related to the stations. This signal is characterized by positive anomalies of temperature after sunrise and negative ones when the solar radiation decreases. We note that southern sites, such as Vallere (*LCZ8val*), Bauducchi (*LCZDbau*), Santena-Banna (*LCZBsan*) and Carmagnola (*LCZDcar*), are characterized by a negative projection onto the second principal component, meaning that these stations experience a later warming in the morning and an earlier cooling in the evenings. This behavior can be ascribed to the different thermal regime existing between the northern and southern portion of the considered area. In the North, the stations are closest to the reliefs and more subject to ventilation, while in the South their location in the Po valley yields to a more frequent inversion in the usual vertical temperature gradient. The colder air near the ground induces a delay in the warming up in the morning and an earlier cooling down in the evening, and it is associated with foggy conditions, as frequently observed in that area [76]. In particular, the Southern stations registered a mean (over the 14 years of the analysis) of 88 foggy days/year, while the Northern ones 17 days/year only [77]. Therefore, we suggest that the second principal component is related to the geographical position of the stations, mainly to their elevation – and so proximity to reliefs – and latitude. The high correlation between the projection onto the second principal component and (i) the elevation of the sites (Pearson's coefficient of correlation $\simeq 0.86$) and (ii) their latitude (correlation $\simeq 0.75$) supports our hypotheses.

1.4 Discussion

1.4.1 Applicability

The Urban Heat Island intensity varies from city to city and its quantification is largely affected not only by the geography and climate of the site, but also by the datasets available to researchers. In this context, the proposed method is conceived to be general and applicable even when the data are not as rich as it is for the case study analyzed here.

The first matter to address is the temporal scale of the UHI analysis.

In the last decades, different scales were focused on, ranging from climatic scales (e.g., [78, 79]) to seasonal analyses – e.g., summer heat waves [80] or waves in winter months [81] – to the negative effects of UHI during night hours in health and welfare studies [82]. There is no single choice, but the selection of the time scale has to agree with the aims of the specific Urban Heat Island study of interest.

If there is no particular purpose other than the characterization of the thermal behavior of stations, the annual time scale represents the most appropriate choice to fully grasp the thermal pattern. In any case, one of the main advantages of the proposed MTD is to be as general as possible and, therefore, adaptable to any temporal scale of interest.

Once the time scale has been chosen – we considered the annual scale in the Turin case study described in the previous section – a second question concerns the duration of the available measures. In order to test this aspect, we applied the MTD method by increasingly reducing our range of data (i.e., 14 years, 13 years, and so on) and we observed that only one year of observations is enough for the MTD to work. In Appendix A we show that the first principal component of the PCA exhibits the same thermal pattern associated to an urban or rural behavior as in Section 1.3. It follows that the metric MTD appears capable of exploiting the data very effectively, even if obviously the longer the period of observations is, the more the results will not be affected by the particular conditions observed in the considered 12 months.

The time resolution of measures is another key aspect. In the Turin test case, we adopted the hourly time step, which is one of the most widely used in UHI literature [36, 83, 84]. However, the robustness of the MTD has been tested also against a coarser temporal resolution: by considering a 3 hour time step (e.g., [85] used this sampling time). In this study, we consider a subset of our original data with temperature measurements at 00, 03, 06, 09, 12, 15, 18 and 21 UTC. Again, the method proves to work very well, since the resulting clustering of stations is equal to that obtained with the hourly temperatures (results are shown in Appendix A).

An important question about the applicability of the MTD concerns the minimum number of weather stations required for the method to work. Turin has a relatively consistent number of measurement sites, but this may not be the case for other cities. In order to test this point, we performed a detailed sensitivity analysis, by re-evaluating the MTD performances using different subsets of the original 11 stations (see Appendix A). By excluding the stations identified as rural by our method (in Section 1.3), the PCA still

identifies an urban thermal behavior and a different one. On the contrary, when considering the rural stations only, the main pattern described by the signal is different and cannot be related to urbanity/rurality. This result is a warning that the considered stations are not a good choice in selecting urban/rural pairs for UHI.

Finally, we evaluated the method on a different dataset and geographic domain: the city of Cuneo, in North-Western Italy. Cuneo is located at a higher mean elevation above the sea level (about 550 m a.s.l.), has a smaller number of inhabitants than Turin (about 60000) and has only two weather stations available, namely Cuneo Camera di Commercio *LCZ2ccc* and Cuneo Cascina Vecchia *LCZ6ccv* (see Appendix A). In the surroundings of the city, the station of Boves *LCZDbov* (575 m a.s.l.) is the only one suitable for this kind of analysis. In addition, the hourly temperatures are available for 18 months only (from July 2019 to December 2020). The Köppen Climate Classification [68] puts Cuneo into the Temperate Oceanic Climate, namely Cfb. Being at the foot of the Alps, Cuneo receives more snow during winter than Turin [77]. Even in this completely different domain, the MTD works very well (see Appendix A): *LCZ2ccc* is deemed as urban, *LCZDbov* as rural and *LCZ6ccv* exhibits an intermediate behavior between the other two.

The minimum number of stations for the application of our method is two, namely the intrinsic number to the Urban Heat Island definition, provided that the selected sites exhibit a different thermal behavior (highlighted in the signal of the PCA) in terms of urbanity or rurality.

1.4.2 Comparison with other methods

The proposed method aims to cluster common behaviors among the available measurement stations, in order to detect the most representative urban-rural pairs for Urban Heat Island quantification in the studied area. The example of Turin shows that the MTD turns out to be an effective metric able to grasp the main differences – in terms of thermal behavior – among the stations.

Given the widely recognized difficulty of the proper selection of urban-rural pairs, the metric which we propose can complement the methods already existing in literature, and provides an additional tool in the UHI research topic for the landscape classification. In this line, it is instructive to compare the results (for the Turin area) of our approach with those of three consolidated methods: (i) the Day-to-Day variation introduced by Karl *et al.* (1995) [51] and further developed by Gough (2008) [52], (ii) the mean daily excursion described by Milelli (2016) [57] and (iii) the ratio

between warm and cold day transitions recently presented by Gough (2020) [58].

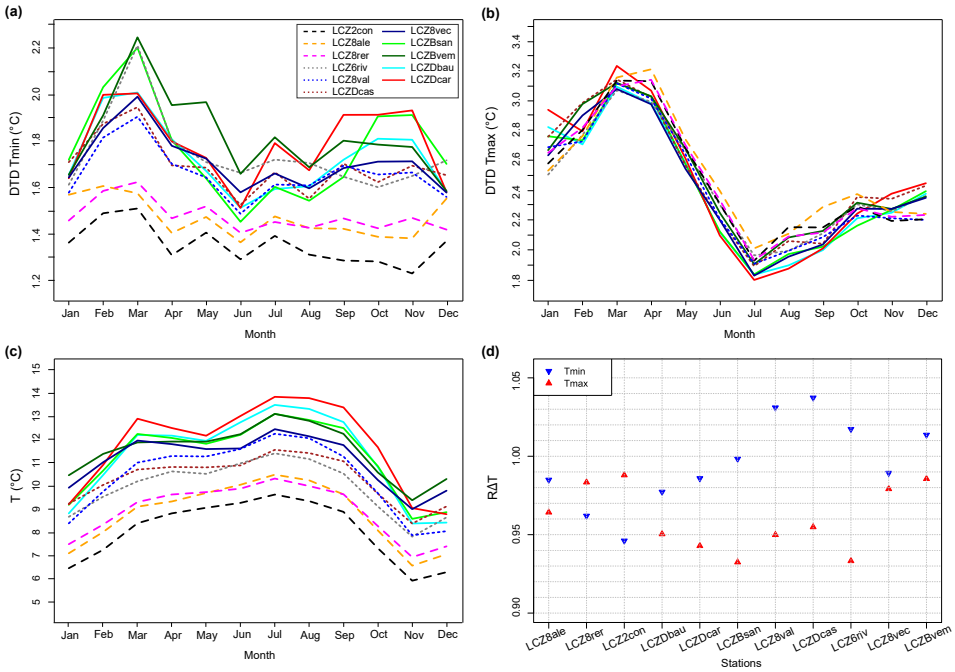

Figure 1.4: Panels **(a)** and **(b)**: Day-To-Day (DTD), i.e., the average monthly DTD variation of nighttime ($T_{\min}$ in **(a)**) and day ($T_{\max}$ in **(b)**) temperatures [56]. The different line styles refer to the thermal behaviors characterizing the stations, obtained through the Mean Temperature Difference (MTD). The dashed lines correspond to stations with positive projection onto the first principal component of the PCA, associated with an urban thermal pattern; the continuous lines refer to stations which projection onto the first p.c. is negative (rural thermal pattern); the dotted lines correspond to the stations characterized by an almost null projection onto the first p.c. Panel **(c)**: mean daily excursion of temperature, i.e., the monthly average of $T_{\max} - T_{\min}$ [57]; this panel refers to the same legend reported in **(a)**. Panel **(d)**: warm to cold transition ratio (RΔT) for the minimum (downwards blue triangles) and maximum (upwards red triangles) temperature of the day [58].

The Day-To-Day (DTD) temperature variation detects urban stations when a site exhibits increasing day-to-day variation in the daytime maximum temperature. Figures 1.4a-b show the results of this metric: DTD is evaluated as the absolute difference between the temperatures of adjacent days for a given period of time (e.g., month) and is calculated both for daily temperature minimum (nighttime, DTD $T_{\min}$) and daily temperature maximum (daytime, DTD $T_{\max}$). According to Oke (1981,1982) [74, 86], urban stations exhibit lower nocturnal temperature variability because ur-

banized areas trap the radiative energy, inducing a slower convective heat loss than the surrounding rural areas. Therefore, the effects of urbanization are associated with the lowest DTD $T_{\min}$. Results shown in Fig. 1.4a highlight a first cluster corresponding to the three urban stations – i.e., Consolata (*LCZ2con*), Reiss Romoli (*LCZ8rer*) and Alenia (*LCZ8ale*) – and this classification is consistent with what we found by the proposed MTD method. The DTD metric for $T_{\min}$ identifies a second cluster characterized by higher values of the day-to-day variation, but it is quite difficult to separate possible intermediate behaviors, at least in an objective way. It follows that the DTD method classifies all other stations – Venaria La Mandria (*LCZBvem*), Venaria Ceronda (*LCZ8vec*), Carmagnola (*LCZDcar*), Santena-Banna (*LCZBsan*), Bauducchi (*LCZDbau*), Rivoli (*LCZ6riv*), Caselle (*LCZDcas*) and Vallere (*LCZ8val*) – as rural and, differently from our MTD approach, seems unable to grasp the intermediate behavior. As described by Anderson *et al.* (2018) [56], even smaller differences between the sites emerge when we consider DTD $T_{\max}$ (see Fig. 1.4b).

The second term of comparison we consider is the mean daily excursion proposed by Milelli (2016) [57], calculated as the difference between the monthly averaged maximum and minimum temperatures (Fig. 1.4c). Here, the three stations Consolata (*LCZ2con*), Reiss Romoli (*LCZ8rer*) and Alenia (*LCZ8ale*) are clearly marked by a limited daily excursion, indicating a non-sufficient cooling during the night and therefore – according to the UHI definition – they are related to a urban landscape. This is in agreement with what detected with the MTD metric. However, even in this case a non clearly distinguished group of stations shows an intermediate behavior, i.e., a gradual transition from the low to the high daily excursion groups emerges. See for example the stations of Caselle (*LCZDcas*), Rivoli (*LCZ6riv*), Vallere (*LCZ8val*) and Venaria Ceronda (*LCZ8vec*) in Fig. 1.4c.

Finally, the application of the ratio between the warm and cold transitions is shown in Fig. 1.4d. By considering Canadian temperatures, Gough (2020) [58] found a metric sensitive to what he called "peri-urban" landscapes, in particular focusing on the warm to cold transition ratio, RΔT, calculated for minimum temperatures $T_{\min}$. Figure 1.4c illustrates the results both for $T_{\min}$ and $T_{\max}$. Gough (2020) [58] identified the threshold for $T_{\min}$ (i.e., RΔT= 1.05) above which a group of stations is deemed peri-urban. If we adopt this threshold, no station falls above this limit; therefore, in the case of Turin, the value RΔT= 1.05 appears not to be adequate to detect intermediate thermal behaviors. This is not surprising because of the different climate in Canada. Using the outcomes of our MTD approach,

a new *ad hoc* threshold equal to 1.016 would allow one to classify Vallere (*LCZ8val*), Caselle (*LCZDcas*) and Rivoli (*LCZ6riv*) in a different thermal behavior, which we call intermediate since it differs from the urban and rural but has no internal coherence. However, a slightly different value (lower or higher than 1.016) would provide very different results: e.g., if RΔT= 1.01 also the station of Venaria la Mandria (*LCZBvem*) would pertain to the intermediate behavior, while for RΔT= 1.02 the only stations with an intermediate pattern would be Vallere (*LCZ8val*) and Caselle (*LCZDcas*). Note that RΔT ($T_{\min}$) for the remaining stations – ascertained as urban (Alenia (*LCZ8ale*), Reiss Romoli (*LCZ8rer*) and Consolata (*LCZ2con*)) and rural (Bauducchi (*LCZDbau*), Carmagnola (*LCZDcar*) and Santena-Banna (*LCZBsan*)) according to the MTD – form two well separated groups and therefore clearly differentiate from the intermediate landscapes, as in [58].

1.5 Conclusions

In a nutshell, the consolidated methodologies, when are applied to the Turin area, agree on the classification of the urban and rural stations, and identify the same urban-rural sites detected by our Mean Temperature Difference method. However, likely due to the complexity of the Turin landscape, the attribution of intermediate thermal behaviors is not straightforward and the consolidated methods seem not to be able to give an objective and unique characterization of this pattern. In contrast, the proposed Mean Temperature Difference seems to be suitable in this area: in light of the Principal Component Analysis, the three stations Rivoli (*LCZ6riv*), Caselle (*LCZDcas*) and Vallere (*LCZ8val*) are characterized by near-zero projections onto the first principal component. In this way, the subjectivity is minimized, since no thresholds or graphic interpretations are needed, differently from the other methods existing in literature. In fact, since the first principal component is associated with the urbanity or rurality of a site, a missing projection onto this component implies a thermal behavior which is neither clearly urban or rural, but rather an intermediate one which is not necessarily characterized by an internal coherence. This observation is also confirmed by the different Local Climate Zones associated to the stations *LCZ6riv*, *LCZDcas* and *LCZ8val*. Their thermal behavior is not captured by the first principal component, but it is synthesized by the second p.c. emerging from the PCA, which is associated to other geographically-based features characterizing the stations.

To summarize, the combined use of MTD metric and PCA represents a

robust tool to characterize the sites in the Urban Heat Island context. The method has been proven (i) to well reproduce the thermal behavior of the metropolitan area of Turin, (ii) to agree with existing and widely validated methods for the distinction between the urban and rural stations, and (iii) to be easily interpretable.

Aware of the impossibility to totally eliminate some kind of subjectivity in the task of selecting urban-rural pairs, we aim at providing an additional tool to discern the landscape categories for the Urban Heat Island quantification. The metric which we suggest can be combined with the existing methods, especially when the study area does not offer a trivial categorization into urban or rural stations.

2

Characterization of the Urban Heat and Dry Island effects in the Turin metropolitan area

The work presented in this chapter has been partially derived from Milelli, Bassani, et al. (2023) [87].

2.1 Introduction

As already introduced in Chapter 1, the Urban Heat Island (UHI) occurs when a city experiences warmer temperatures than its nearby rural areas. This phenomenon amplifies the heat-stress hazard and increases the heat-related mortality in the cities [88]. The 2018 Revision of World Urbanization Prospects [89] reports that the urban population will increase in the next decades; therefore the topic of urban-related hazards is becoming more and more important in the scientific community [36, 46, 48, 90]. An adequate characterization of urban/rural differences is essential to understand the thermal and moisture characteristics of the urban environment and the related human stress [91].

Also the humidity content can be modified by the presence of an urban area: the reduced amount of vegetation and water and, conversely, the large areas of impermeable land surface produce a moisture drop which results in an Urban Dry Island (UDI) over the city, particularly during the day [92, 93]. The UHI is affected by a number of meteorological parameters, primarily wind and cloud cover [94]. The former is a proxy of air mass transport and air mixing, which are responsible for smoothing temperature differences, the latter directly affects short- and long-wave radiation.

All these topics have been studied all around the world – in different climates, different cities of various size and population density – with respect to the so-called urban canopy layer (UCL) Heat Island or UHI_{UCL} (e.g., [34, 72, 95–98]). The UHI_{UCL} (after Oke et al., 2017 [27]) corresponds

to the layer between the urban surface and roof level and it is the most studied form of UHI because ground sensor networks are widely available. Differently, the urban boundary layer (UBL) Heat Island (UHI_{UBL}) refers to the characteristics of the volume of air between the top of the UCL and the top of the UBL, and to the corresponding volume (in height) above the rural surrounding areas. In this case, it is less frequent to find comprehensive studies on the subject, since the observations (coming from LiDAR, wind profiles, radiometers, radiosondes) are not so commonly available. Field campaigns such as BUBBLE (Basel Urban Boundary-Layer Experiment) in Switzerland [99], or METROMEX (Metropolitan Meteorological Experiment) in St. Louis [100], or the one in Oklahoma City [101] are extremely valuable examples. There are some studies characterizing the UHI_{UCL} in Italian cities, such as Rome [96, 102–104], Bologna [105], Padua [106], Florence [107], Milan [108] and Bari [109]. Regarding Turin – the fourth city in Italy by inhabitants, located in the Northwest region of the Italian peninsula – an attempt was made by [57] for a time-limited set of data. A more recent study about the Urban Heat Island of Turin between 2003 and 2016 described an UHI intensity of the order of 0.5-1.5°C, but focusing on annual means only [110]. In the present work the UHI of Turin is further investigated on hourly base by adopting a different set of weather stations.

It has to be noted that Turin is a peculiar case to study for several reasons. First of all, it is well known that the climate and topography of cities together with their geographical location influence the formation of the UHI [27]. In this sense, the city of Turin represents a case that deserves particular attention: its closeness to the Alps on the west, to the hills on the east and the presence of four rivers make the city very interesting from a meteorological point of view. In addition, the availability of three microwave radiometers in the Turin area – one in the city center and two in the rural surroundings – allows to study the three-dimensional structure of the boundary layer over the city and over the rural surroundings.

The goal of this work is to describe the characteristics of the Urban Heat Island effects over Turin. To this end, we will focus on four urban features: (i) the UHI_{UCL} by ground-level temperature measurements, (ii) the concomitant occurrence of UDI effect by ground-level humidity measurements, (iii) the impact of wind on UHI/UDI formation, and (iv) the UHI_{UBL} by using the vertical temperature profiles provided by radiometers. In order to choose the urban-rural pairs necessary to the UHI quantification, we capitalized our previous findings of Chapter 1 [43] and considered five

ground-level stations: three urban and two rural. The latter two allowed us to highlight the differences between the rural light wooded area North of Turin and the rural area South of the city, located in an open grassland with scattered trees.

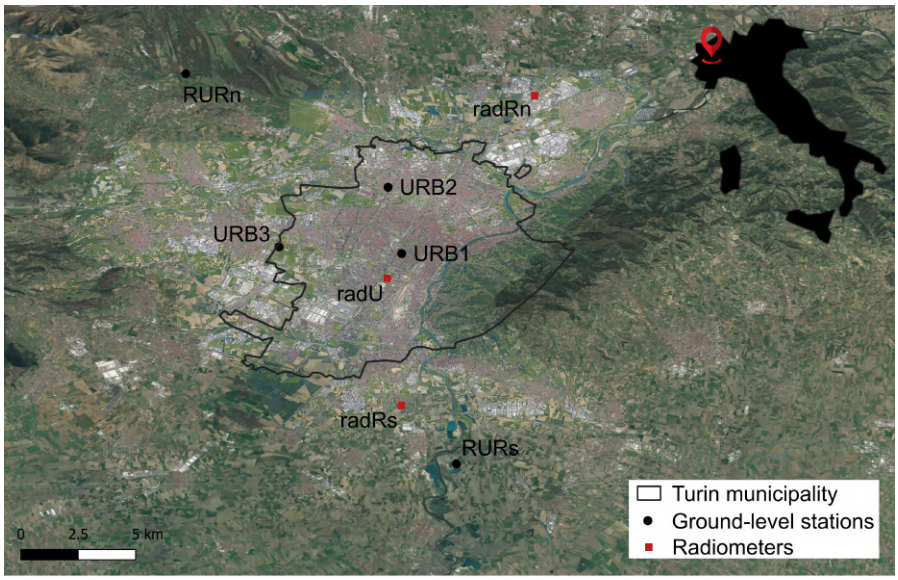

Figure 2.1: Map of the metropolitan area of Turin (North-West of Italy, in the inset), with the Turin municipality highlighted with a black line. The black dots indicate the weather stations used for the ground-level analysis of temperature and humidity (see also Tab. 2.1) and the red squares denote the radiometers providing the temperature vertical profiles.

2.2 Area of study and data

The metropolitan area of Turin is located in the North-West of Italy and encompasses about 600 km^2 with a population of approximately 1.5 million inhabitants. The urban agglomeration develops within a plane topography, where the Po river flows in the South-East and separates the city from the surrounding hills in the East, as shown in Fig. 2.1. The Köppen Climate Classification [68] puts Turin into the Marine West Coast Climate, namely Cfa (C = warm temperature, f = fully humid, a = hot summer). The coldest month averages above 0°C, at least one month's average temperature is above 22°C, and at least four months average above 10°C. Concerning the precipitation, there are no dry periods in summer and the months with the

lowest values are December, January and February, but the amounts are still relevant [111].

For the purposes of this study, several meteorological stations – all pertaining to the network of the Regional Agency for the Protection of the Environment of Piedmont Region (Arpa Piemonte) – are considered (see Fig. 2.1 and Tab. 2.1).

2.2.1 Near-surface instruments

Hourly near-surface temperature (T) and relative humidity (Rh) data are recorded by the first five stations reported in Tab. 2.1. They are chosen on the basis of the longest temporal series available, from January 2007 to December 2020, providing 14 years of data to analyze. Their urban or rural assignment is based on the Mean Temperature Difference (MTD) method proposed in Chapter 1 [43]. In this approach, the monthly-averaged temperature recordings are considered for a heterogeneous group of weather stations, the thermal pattern characterizing each site is detected and, finally, Principal Component Analysis is used to cluster the stations exhibiting common behavior. Since the MTD method has been tested on Turin, we adopt here the findings of Chapter 1. In particular, the stations of Consolata (URB1), Reiss Romoli (URB2) and Alenia (URB3) are identified as urban, while Venaria La Mandria (RURn) and Bauducchi (RURs) as rural (RUR). The letters associated to the two selected rural stations refer to their location, namely North (*n*, Venaria la Mandria) and South of Turin (*s*, Bauducchi). They are characterized by well-defined rural thermal behaviors and their location is characteristic of each geographical area, i.e., the northern and the southern plains. In addition, wind velocity (Wv) measurements are available for the urban station of Alenia (URB3) and for the rural Bauducchi station (RURs). The considered stations were not relocated during the studied period and the local surroundings at the sites did not change. The original data quality check (QC) is made internally by the owner institution (Arpa Piemonte), and we used the validated data available on the Arpa database. We can show on Tab. 2.2 the percentage of data missing (because of instrument failure or because they failed the internal QC) over the entire 14 years period, on hourly base. It can be seen that the percentage is quite low, and only RH in URB2 has a larger amount of "NotAvailable" (NA) data.

	Station name	Station short name	Lat (°N)	Lon (°E)	Type	Records
1	Consolata	URB1	45.0758	7.6783	urban	T, Rh
2	Reiss Romoli	URB2	45.1125	7.6708	urban	T, Rh
3	Alenia	URB3	45.0797	7.6108	urban	T, Rh, Wv
4	Venaria La Mandria	RURn	45.1750	7.5592	rural	T, Rh
5	Bauducchi	RURs	44.9610	7.7086	rural	T, Rh, Wv
6	Leiní	radRn	45.1632	7.7507	rural	vT
7	Moncalieri	radRs	44.9925	7.6780	rural	vT
8	Torino	radU	45.0626	7.6701	urban	vT

Table 2.1: Meteorological stations – sorted alphabetically by their short names – used in the ground-level analysis (upper box, stations 1-5) and in the vertical analysis (lower box, 6-8). The last column refers to measurements of: temperature (T), relative humidity (Rh), wind velocity (Wv) and vertical temperature profiles (vT).

	T2m	RH2m	W10m
URB1	0.015	0.012	-
URB2	0.304	5.464	-
URB3	0.067	0.180	0.115
RURn	0.306	0.318	-
RURs	0.051	0.066	1.942

Table 2.2: Percentage (%) of missing hourly values during the whole period (2007-2020) for the considered stations and the different variables. For the name of the stations, see 2.1.

2.2.2 Radiometers for vertical measurements

Three radiometers, model MTP5, are used to analyze the thermal structure of the urban boundary layer (Fig. 2.1 and last three rows of Tab. 2.1). They are passive microwave instruments based on the measure of the thermal radiation coming from the atmosphere at the center of the molecular oxygen absorption band [112]. The radiometer obtains the temperature (at different elevation angles, on a vertical plane) by a self-calibration process, through which measured values are compared with an external ambient temperature sensor, and a noise generator inside the instrumentation. Scans are performed at 10 minute intervals and the output levels (vertical temperature profiles vT, see Tab. 2.1) are given every 50 m. The urban radiometer is located on the roof of a building in the city center (radU, 277 m a.s.l.). The other two radiometers are considered rural since their location is far outside the most urbanized area (see Fig. 2.1), above industrial buildings: Leinì (radRn, 240 m a.s.l.) and Moncalieri (radRs, 230 m a.s.l.). As above, the letters *n* and *s* indicate their location at North (radRn) and South of Turin (radRs). The elevations include

the building heights: 30 m for radU, 20 m for radRn and 5 m for radRs. The Leinì instrument (radRn) measured up to 600 m between 2007 and 2013 and up to 1000 m from 2013 onward. The others (radRs and radU) measured up to 1000 m for the entire considered period. Therefore, in order to avoid inhomogeneities in the dataset, it has been decided to use only data up to 600 m for all the three radiometers in the entire period 2007-2020. This allowed us to have a larger statistics keeping the focus on the lowest part of the boundary layer. Regarding the data provided by the 3 radiometers, no QC is currently implemented in Arpa Piemonte for them. An accurate validation was then performed by comparing the first level temperature provided by each radiometer with the temperature provided by a nearby thermometer and excluding those values differing more than 2°C. In addition, each radiometer was subject to power cuts, instrument failure and shutdown periods for recalibration. Due to the large amount of unavailable data, we decided to compare the radiometers over a common period when all three radiometers were operational, and this resulted in 44% of unavailable data from 2007 to 2020.

2.3 Ground-level analysis

2.3.1 Temperature and Urban Heat Island

The comparison of the mean daily cycle of temperature for the selected stations for different seasons is shown in Fig. 2.2. The hours on the x-axis are always in UTC.

When considering the mean maximum temperatures all the stations show similar values. The most relevant differences in the thermal patterns emerge during night times, when the urban mean minimum temperatures are clearly higher than the rural ones, regardless of the season. Such differences are statistically significant – at the 5% significance level by using the two-sample t-test [113] – as reported in Appendix B. Notice that RURs usually exhibits higher temperatures than RURn, except for winter. Actually, in this season the southern station experiences a delay in the heating with respect to the northern one at sunrise, resulting in lower temperatures during daytime. In addition, the mean temperatures recorded by the two rural stations are statistically different with the exception of few daytime hours in winter, spring and fall (Appendix B). This is coherent with the analysis of [43], that showed weather stations located in the southern area of Turin to be characterized by a different thermal regime than those in the North. In fact, the northern plains are about 100 m higher than the southern plain

and they are close to North-West oriented Alpine valleys, which favours the intrusion of Föhn, the typical katabatic wind able to enhance the turbulent mixing layer [114, 115]. Instead, the southern plains are much less affected by strong winds and are characterized by more frequent inversion in the vertical temperature gradient, especially during the coldest months.

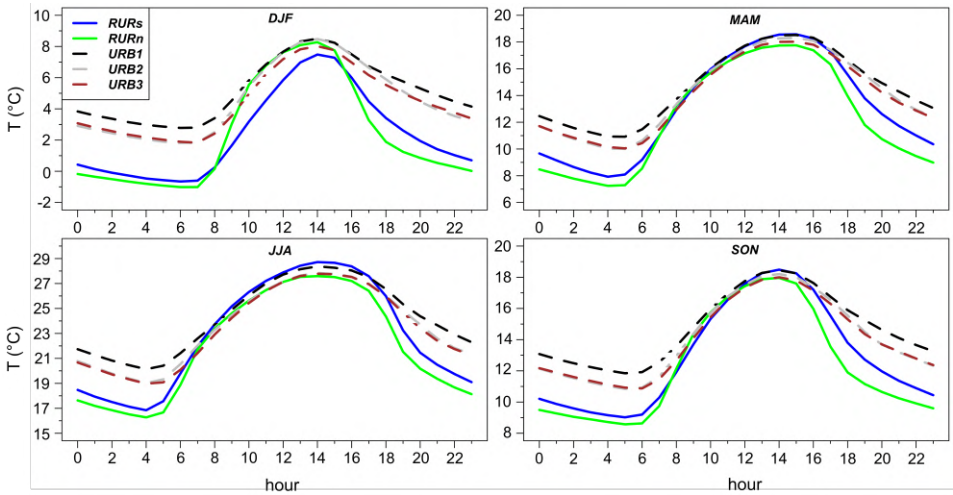

Figure 2.2: Mean daily cycles of the ground-level temperatures registered in the metropolitan area of Turin for winter (DJF), spring (MAM), summer (JJA) and autumn (SON).

In terms of intra-city variations, we observe a very similar, almost overlapped, behavior between the two urban stations URB2 and URB3, while URB1 always shows the highest temperatures at night times. Actually, the mean nocturnal temperatures measured in URB2 and URB3 are on average 0.5-1°C lower than URB1. This is due to the proximity of URB2 and URB3 to the city suburbs, which induces a slightly larger cooling with respect to URB1, that is located in the city center and experiences the most pronounced Urban Heat Island Effect. Indeed, the mean daily cycles of URB2 and URB3 do not show significant differences, while URB1 is statistically different from the other two urban stations, especially during night times, which are relevant for the Urban Heat Island effect (details for every hour are provided in Appendix B).

The different steepness of the night-day-night transition can be clarified through the rate of temperature change (ROC, [116]), which is defined for every hour h as $(T_{h+1} - T_h)/\Delta t$ and which is reported in Fig. 2.3. In particular, the seasonally-constant behavior of the urban stations is quite evident. In the morning they show smaller warming rates after sunrise

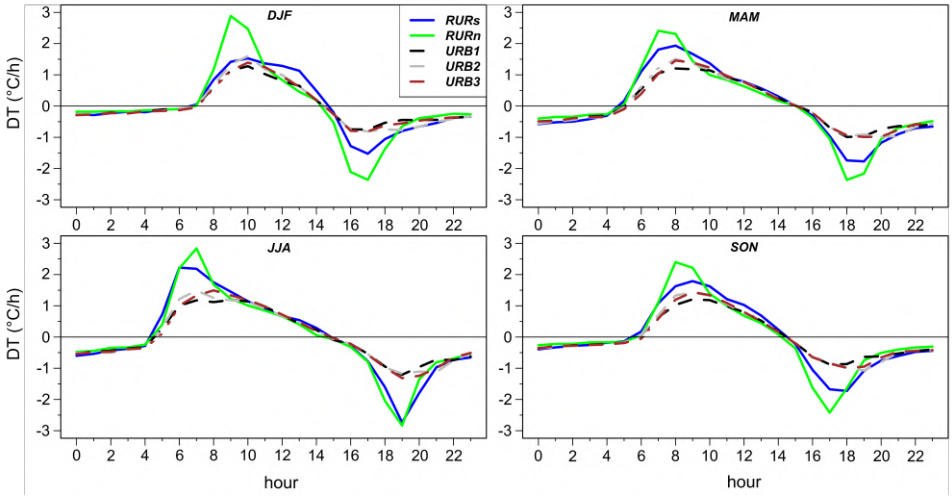

Figure 2.3: Mean daily cycles of temperature rate of change (ROC). The different panels refer to the four seasons: winter (DJF), spring (MAM), summer (JJA) and autumn (SON).

with respect to rural sites (not more than 1.5°C/h compared to 2-3°C/h measured in the rural stations), because the available energy from the sun is mostly stored in the building walls and roofs rather than in heating the UBL air. This is due to the different properties characterizing the urban fabric, with a greater thermal inertia than the natural lands [27]. Such stored heat is then released in the evening as sensible heat flux in the urban boundary layer [117], producing significantly smaller cooling rates after sunset with respect to rural areas (1°C/h instead of 1.5-2.5°C/h). It is interesting to point out that after sunrise in winter, the ROC of RURs is closer to the urban behavior rather than to RURn. This agrees well with the different UHI observed between the North and the South. The colder air layer trapped near the ground by the frequent inversions, induces a delay in the morning warming up of the southern area, and it is associated with frequent foggy conditions in this zone [76]. In particular, the southern station registered a mean (over the 14 years of the analysis) of 88 foggy days/year, while the northern one 17 days/year only [77], because it is closer to the reliefs and more subject to ventilation. For the same reason the cooling rate after dusk is less steep. This is actually true also in spring and fall, because the southern station is ≈600 m distant from the Po river whose latent heat release mitigates the transition.

As the station of Consolata (URB1) is the "most urban" among the three sites in the city, we chose it to represent the urban term in the UHI

quantification. We evaluated the hourly mean UHI – time-averaged over the total period of data availability (14 years) – as: $(T_{URB1} - T_{RURs})$ and $(T_{URB1} - T_{RURn})$, in order to feature the spatial differences between the South and the North of Turin, respectively (see Fig. 2.4). The statistically significant higher temperatures perceived by the urban station during night hours, with respect to the southern and northern rural sites, yield to the typical thermal behavior characterized by positive UHI when the solar radiation decreases.

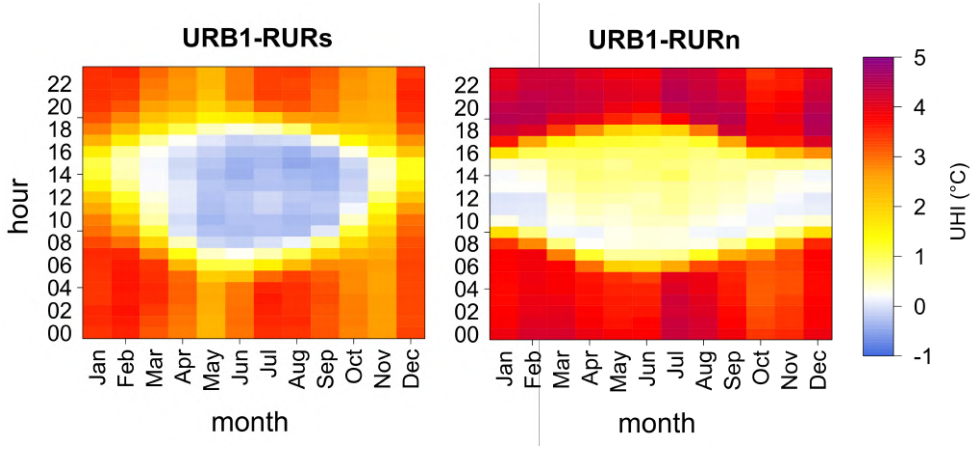

Figure 2.4: Mean annual UHI (averaged over the 14 years of data availability) computed as URB1-RURs (left panel), and URB1-RURn (right panel).

Regarding the southern station (RURs), the maximum UHI values reach $\approx 4°C$ at night (see the left-hand side panel of Fig. 2.4). During the central hours of the day from April to October, the pair URB1-RURs exhibits a slight negative UHI: this phenomenon is known as Urban Cool Island (UCI) effect [97] and was found in other cities (e.g., see [118]). It refers to the morning different mixed-layer depth, deeper over the city and shallower over the countryside and to the different warming rate after sunrise, higher over the countryside and lower over the city. Both the processes induce a temperature overtaking which can last till early afternoon [71]. On the contrary, from November to March daytime UHI is always positive ($\simeq 1°C$), most likely due to the frequent inversion phenomena occurring in the southern area [77], which inhibit air heating and result in colder temperatures.

The difference between T_{URB1} and T_{RURn} exhibits higher mean nocturnal values than the UHI computed with RURs, reaching $\simeq 5°C$ at night. Moreover, while for the southern UHI we observe the UCI effect, the northern

RURn is always characterized by positive or neutral UHI.

2.3.2 Absolute Humidity and Urban Dry Island

The effects of an urban environment on the atmosphere moisture are less investigated than the thermal ones, e.g. see the studies by [92, 119–121]. Different parameters can be used: relative humidity (the most common), absolute humidity, specific humidity or vapour pressure. Since relative humidity is dependent on air temperature and pressure, it is not advisable to measure horizontal or vertical differences of moisture in different places, because they might involve different temperature and/or pressure as well [27]. Thus, we adopted absolute humidity (AH) as the indicator of possible changes of moisture between the city and the surroundings.

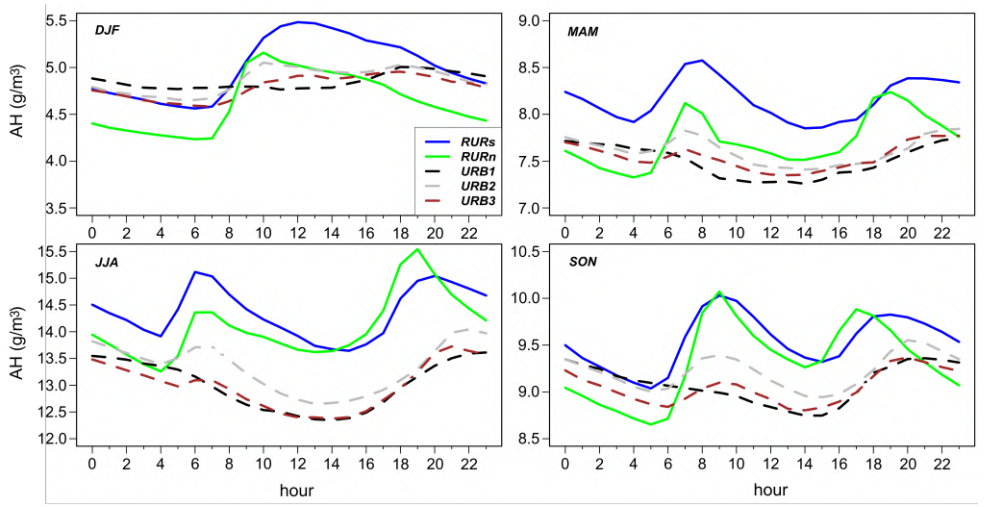

Figure 2.5: Mean daily cycles of absolute humidity data registered in the metropolitan area of Turin for winter (DJF), spring (MAM), summer (JJA) and autumn (SON).

In Fig. 2.5 we show the seasonal mean daily cycle of AH for the same reference stations used for UHI. The first feature is the double peak of the rural sites, one a few hours after sunrise and another one around sunset, which occurs in spring, summer and autumn. In the morning the mixing layer is still shallow and the evaporation increases at sunrise, favouring the increase of AH (first peak). This first peak is significantly higher for the two rural sites than the urban ones: it is, on average, about 0.5 and 1 g/m^3 larger for RURs and RURn, respectively, during MAM and JJA; in SON the two rural recordings are characterized by non-significant differences in

the first peak, which reaches 10 g/m^3 (details of the t-test are reported in Appendix A). Then, with the increase of solar radiation, turbulence increases the mixing layer height and AH decreases, still remaining statistically higher in the rural sites than in the urban ones, with differences reaching the maximum deviation of 1 g/m^3 in summer day times. When approaching the sunset, the surface starts cooling reducing the convective turbulent activity and increasing the stability; the mixing layer height starts decreasing and the AH increases (second peak) also because the evaporation is still on. After sunset, AH decreases again because evaporation stops and, especially during the coldest months, the possible formation of dew removes water vapor from the air.

In winter only one peak is visible at midday. In this case the time distance between sunrise and sunset is smaller and the mixing layer remains shallow throughout the day [27]. Albeit both rural sites show the single peak in AH, the values reached by the southern rural RURs are always higher than those of the northern station (such differences are statistically significant, as discussed in Appendix A). In particular, the maximum absolute humidity is registered at noon in the southern station. AH is usually higher in RURs than in RURn because (i) the proximity of RURs to the Po river favors advection of moister air and (ii) RURn is colder than the southern station (see Fig. 2.2), favouring the formation of dew in the nights and the removal of AH from the atmosphere. In the urban environment, the trend is similar to the countryside but moisture values are generally lower. AH in the city during daytime is lower than in the countryside, since the latent heat flux (and so the evaporation) is weaker due to the prevalence of impervious surfaces and the higher turbulent mixing layer. During the winter, spring and autumn night hours, AH values are slightly higher in the city than in the northern rural station (RURn). This is most likely due to the presence of highly-grown vegetation in RURn and the occurrence of colder temperatures, which favor dew formation. Such discrepancies are found to be statistically significant (see Appendix A), especially when comparing the urban URB1 with RURn, except for few hours where the curves intersect. Instead, being the rural RURs less vegetated than RURn, we observe that only winter nights are slightly moister in the city, with statistically significant differences of about 0.5 g/m^3.

Note that the diurnal cycle of solar radiation, i.e., its increase (or decrease) – associated to the higher (or lower) mixing layer height – and the season are not the only causes impacting substantial changes in the absolute humidity (see Fig. 2.6). On short-time scales AH is strongly

affected by the meteorological conditions in the area of interest, e.g. the intensity of the wind or the amount of precipitation. Another important factor, which is again strictly related to the location of the studied area, lays in the occurrence and amount of water bodies. As discussed above, the presence of the Po river nearby the southern rural station fosters incursions of air with relatively high humidity and, therefore, it plays a decisive role in differentiating significantly the southern and northern rural responses to AH variability. Among the causes, a remarkable influence in the absolute humidity is given by the land use, which in turn directly affects the different surface energy balances and the sensible and latent heat fluxes. For instance, focusing on urban and natural landscapes, the most evident difference between the two landscapes is the prevailing impervious surface cover and the relative lack of vegetation in cities. As a consequence, the relation between urbanization and humidity is straightforward [122].

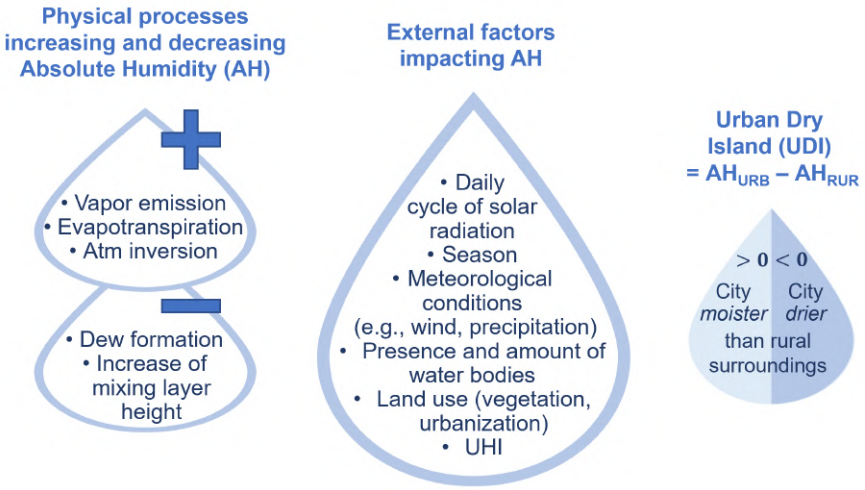

Figure 2.6: Graphical scheme of the Urban Dry Island effect: physical processes increasing (+) and decreasing (-) the absolute humidity (left drops), external factors impacting AH (center drop) and UDI effect (right drop).

Generally, the atmosphere of an urban settlement is found to be drier than its surroundings [93], particularly during daytime. Therefore, in analogy with the UHI effect, the phenomenon is named Urban Dry Island (UDI) effect [123]. Since not statistically significant differences emerge in the behavior of the three urban stations (see Appendix B), we considered the "most urban" station URB1 to compute the UDI intensity (coherently with Section 2.3.1). $(AH_{URB1} - AH_{RURs})$ for the southern UDI and $(AH_{URB1} -$

AH_{RURn}) for the northern UDI. Since the physical processes behind the urban effect on humidity depend on a range of factors (Fig. 2.6), it is quite challenging to disentangle the UDI occurrence in different cities. Actually, the mechanisms involved in the enhancement of AH in the urban boundary layer depend on moisture advection, on the direct vapor addition (e.g., emissions from chimneys or stacks), on evaporation processes and on the eventual atmospheric inversion, which favors a shallow mixing layer resulting in higher humidity [27]. On the contrary, the dew formation at the ground's surface acts like a sink factor for AH, that is removed from the atmosphere to condense as water droplets. In addition, the increase of the mixing layer height may decrease the content of humidity from the surface due to the enhanced turbulent transport. Keeping in mind all these competing factors, in the following we discuss the UDI characteristics observed in Turin on the basis of the data at our disposal. Fig. 2.7 shows the mean hourly UDI for each month of the average year. Positive UDI values indicate that the city – represented by the urban station URB1 – is moister than the rural surroundings, while it is drier when the UDI is negative.

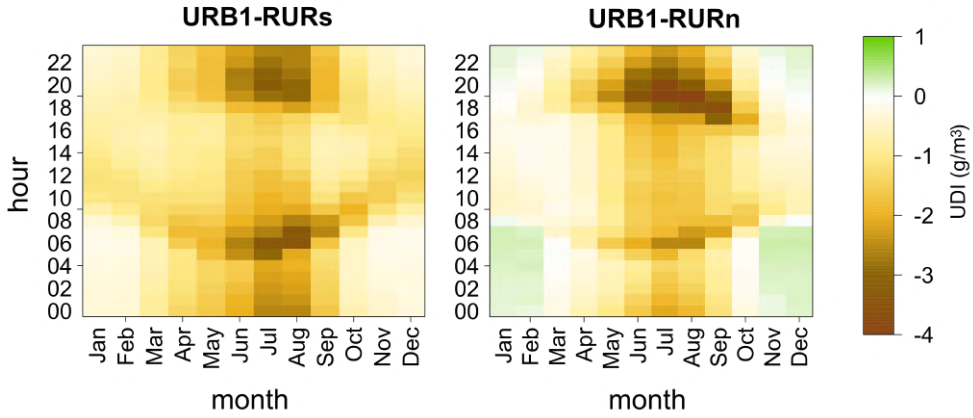

Figure 2.7: Mean annual UDI (averaged over the 14 years of data availability) computed between URB1-RURs (left), and URB1-RURn (right).

The left panel of Fig. 2.7 shows that the city is always drier than the southern rural surroundings, resulting in UDI values up to -3 g/m^3 in summer. Regarding RURn (Fig. 2.7 right panel), the city results drier than this rural station during day times (like URB1-RURs) and reaches the highest values (close to -4 g/m^3) during summer evenings. This is related to the particular orography and climatology of the region. Actually, the northern areas receive a larger amount of precipitation during the year

than the southern plains and, in particular, summer convective activity is higher in the North, being at the foot of the Alps [77]. Differently from the pair URB1-RURs, the northern UDI is characterized by positive values during winter nights (around 0.5 g/m^3), meaning that the city is moister than the northern rural station RURn. In fact, being the northern area colder than the city, the formation of dew and ice in the northern plain is boosted, removing moisture from the lower atmosphere and resulting in less AH content than Turin. Other cities (e.g., London [124]) usually experience a constant moisture excess in the night all over the year. This behavior is not always found for Turin, where the AH contents is different between the South and the North.

In a nutshell, during the day Turin is (on average) always drier than both the southern and northern rural surroundings. This is due to the higher evaporation from the surface occurring in the natural landscapes than in the city, caused by the different surface characteristics. Instead, during the night the humidity content depends on the balance of different factors and it is difficult to draw a unique conclusion. On the one hand, according to [27], the city could be moister than the countryside at night for three reasons. Firstly, albeit after sunset the evaporation can be considered almost null, the city still releases the heat stored during the day (Urban Heat Island), resulting in the occurrence of a weak evaporation. Secondly, dewfall in the city may be much lower than the countryside; thirdly, some industrial activities and human emissions never stop, fuelling the urban moisture. Nevertheless, during the night the urban AH content may be reduced because of the increasing of the mixing layer height due to the presence of buildings (urban geometry). On the other hand, the countrysides may be affected by dew formation which subtracts AH from the air. Therefore, when comparing the urban and the rural areas, the prevailing of one factor over another depends on the typical characteristics of each specific zone, e.g., the presence of the Po river in the South and the colder climate of the North.

2.3.3 Influence of wind

It is known that the UHI intensity is stronger during windless meteorological conditions (e.g., [125]), while high wind speed prevents the formation of UHI effect [119]. According to Oke (1973, 1976) [34, 47], there is a threshold wind speed after which the intensity of the UHI decreases until becoming negligible. To investigate this aspect, a comparison between the southern nocturnal (23-05UTC) UHI and the corresponding wind speed registered in the rural station RURs is shown in Fig. 2.8 (in red). The wind

speed is not available in RURn (see Tab. 2.1). The plot shows two different regimes, a sharp decrease towards zero and a quasi-horizontal plateau. The wind speed value for which the UHI reaches the plateau is around 3-3.5 m/s, value quite similar to the threshold of 4 m/s found by [126] in Thessaloniki, Greece. In Melbourne [127] it was found a linear decrease of UHI with a wind speed larger than 2 m/s, but in that case the UHI averaged over 20 years of measurements was significantly lower than in Turin.

It has to be underlined that the peculiar topography characterizing the city with the Alps all around, from North to West, and the hills at East, makes Turin not a windy city. The highest wind values usually happen in case of sigle Föhn events (North-West wind).

The same Fig. 2.8 (in blue) shows the relation between diurnal (06-20UTC) UDI intensity and wind speed. Here, a rapid linear increase of UDI is followed by a flat trend and the wind speed at which we observe the change of regime is 4-4.5 m/s.

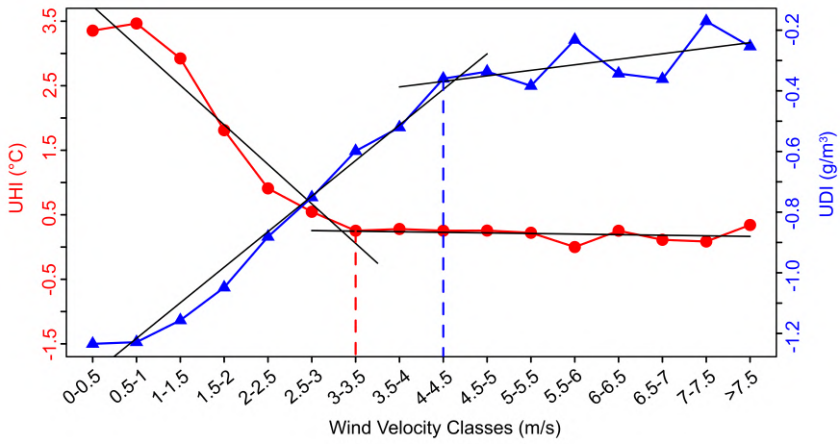

Figure 2.8: Mean UHI (in red, left y-axis) and UDI (in blue, right y-axis) intensities (URB1-RURs) for each wind speed class registered in RURs. E.g., the class 0-0.5 in the x-axis refers to the wind speeds between 0 and 0.5 m/s for which the UHI (or UDI) is averaged. Linear trends are highlighted by black lines.

2.4 Vertical analysis and boundary layer Heat Island

In the present section, the observations provided by the three radiometers are shown to highlight the features of the urban boundary layer with respect

to the rural neighborhood: in fact, a radiometer is located in the city center (radU), while the others (radRn and radRs) are located respectively in the northern and southern rural area surrounding the city (see Fig. 2.1).

Since the UHI is a nocturnal phenomenon, we focus on the vertical structure of temperatures during night hours. The nocturnal vertical profiles are shown in Fig. 2.9. They are obtained by averaging the temperatures recorded between 23UTC and 05UTC among the 14 years of data availability, and they are plotted with respect to the elevation above the ground level (m a.g.l.), which corresponds to the height of the buildings (5 m for radRs, 20 m for radRn and 30 m for radU).

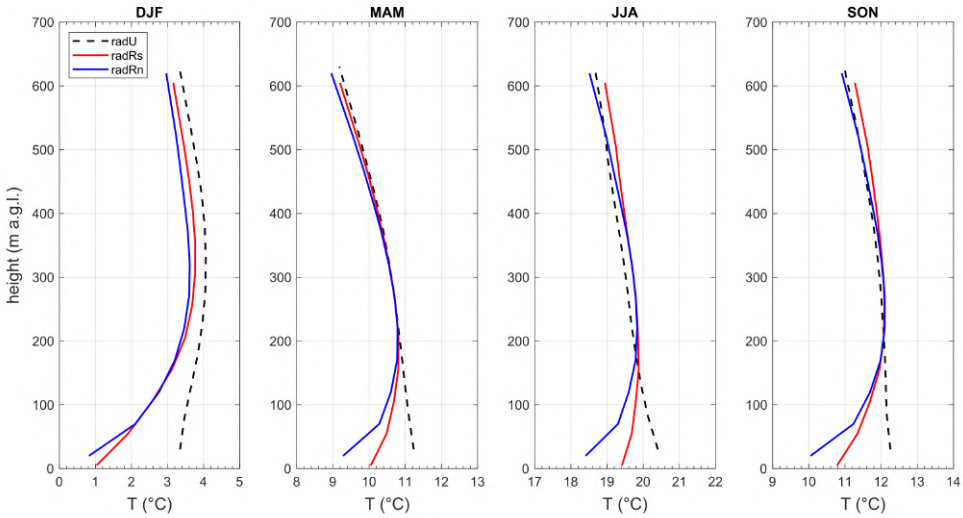

Figure 2.9: Averaged nocturnal vertical profiles, from 23UTC to 05UTC, for winter (DJF), spring (MAM), summer (JJA) and autumn (SON). The urban radiometer (radU) is marked by a dashed black line, while the southern (radRs) and northern (radRn) rural radiometers by continuous red and blue lines, respectively.

Initially, we focus on the lowest level common to the three radiometers, namely 30 m a.g.l. During all seasons, the urban radiometer radU (see the dashed black line in Fig. 2.9) exhibits significantly higher temperatures than radRn and radRs, in analogy with what observed with near-surface temperatures (in Section 2.3.1 and in Appendix B). The greatest mean temperature excess of radU with respect to the rural radiometers occurs during winter, where it reaches about 2°C. During the other seasons the urban radiometer is about 1°C warmer than the southern radRs and almost 2°C warmer than the northern radRn, on average. Notice that the coldest

temperatures always occur for the northern rural radiometer (radRn). This is in line with what observed at the ground-level analysis, where the northern rural ground-level station experienced the lowest nocturnal temperatures.

Focusing on few levels above the first one, an important remark concerning the urban effect on vertical temperature screenings is the thermal inversion in the vertical profile. Two main features clearly emerge. The first is that winter (DJF) is the season characterized by the strongest inversion experienced by the rural radiometers. Secondly, winter is also the only season for which a slight inversion in the vertical profile occurs for the urban radiometer (radU). This is mainly due to the cooling of the urban surface which releases the heat stored during the day, enhanced by the anthropogenic heat emissions, resulting in an upward sensible heat flux towards the upper layers [128]. For radRn and radRs the greatest intensity of the inversion, computed as the difference between the maximum and the lowest level temperatures along the profiles, occurs during winter months and it reaches a mean amplitude of about $2.5 - 3$°C. In other seasons, the inversion experienced by the rural stations decreases in intensity: during spring and summer it is about 1.5°C for radRn and $\simeq$ 0.5°C for radRs; then, it starts increasing again in fall ($\simeq$ 2°C for radRn and $\simeq$ 1.5°C for radRs). All the differences between the urban radiometer and radRs and radRn, respectively, are found to be statistically significant (according to the t-test reported in Appendix B) up to 350 m a.g.l. in winter and up to 100 m a.g.l. during the remaining seasons. Notice also that in summer, the urban radiometer show slightly colder temperatures than the rural recordings between 200 and 500 m a.g.l. While such differences are statistically significant over the whole vertical layer for the southern radRs, the t-test showed that it is true only between 250 and 350 m a.g.l. for the northern radiometers (see Appendix B).

The vertical temperature (vT) distribution over the studied area is further investigated by computing the Urban Heat Island intensity as the difference of temperatures, screened by the radiometers, between the urban radU and the rural radRs and radRn. In order to refine resolution, the 50 m-sampled values were linearly interpolated and re-sampled with a 5 m step. The mean nocturnal profiles of the UHI_{UBL} for each season, averaged in the hourly range 23-05UTC, are shown in Fig. 2.10. The southern UHI vertical profile is given by $vT_{radU} - vT_{radRs}$ (left panel in Fig. 2.10), while the northern one is computed as $vT_{radU} - vT_{radRn}$ (right panel in Fig. 2.10). Like the UHI_{UCL}, positive values refer to urban temperatures warmer than the rural surroundings.

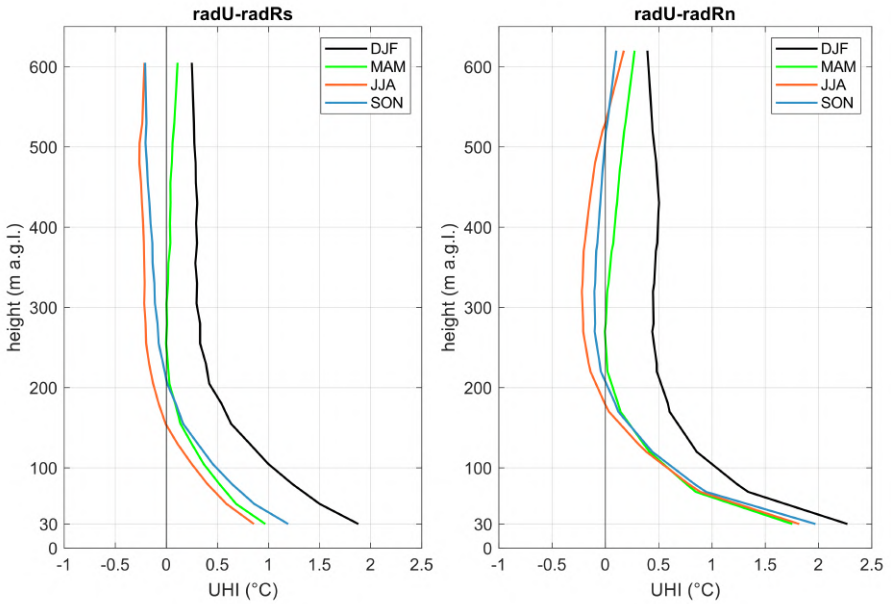

Figure 2.10: Nocturnal mean seasonal profiles of UHI, averaged from 23UTC to 05UTC and computed with respect to the southern radiometer (radU-radRs, left panel) and to the northern one (radU-radRn, right panel).

The lowest layer at 30 m above the ground shows that the nocturnal UHI computed for the southern radiometer is around 1°C during spring, summer and autumn and it reaches its maximum in winter (≈2°C). A similar picture is found for the northern pair radU-radRn, being winter the season with the highest UHI, but for all seasons the UHI values are higher than the ones registered South of Turin. Moving up towards the higher levels, both the southern and the northern UHI vertical profiles (regardless of the season) decrease from the first scan up to the urban boundary layer height, above which they get balanced. This layer ranges from 30 m to about 150 m a.g.l. both for the southern and the northern UHI, with the exception of winter season. In this case, both for the southern and the northern pairs, we observe that the UHI profiles remain weakly positive along the whole vertical air column (less than 0.5°C). This is due to the very shallow mixing layer height, which prevents the turbulent mixing of the atmosphere and maintains temperature differences over the city.

For the southern UHI profiles (Fig. 2.10, left panel), we observe that the UHI becomes negative above ≈150 m a.g.l. in summer and above ≈200 m a.g.l. during autumn, and this slightly colder air layer of the city extends

vertically to the limit of the measured region. A similar behavior occurs also for the northern profiles (Fig. 2.10, right panel), where the UHI becomes negative above ≈180-200 m a.g.l.; the fact that the profiles become positive again above ≈500 m a.g.l. during summer and autumn is not statistically significant (see Appendix B).

The negative values of UHI above certain heights, meaning that urban vertical temperatures are lower than ones in the rural surroundings, is a phenomenon known as cross-over or cold lens effect [74, 129, 130] and was firstly observed by [131]. It indicates the existence of a portion of air which is slightly cooler over the city (urban boundary layer) than at the same elevation over the countryside [74]. A possible explanation is related to the nocturnal inversion from which heat has been removed by entrainment. Another reason concerns the divergence of the long-wave radiative flux occurring at the top of the urban boundary layer: the uplift due to heat island convergence causes radiative cooling of aerosol and adiabatic cooling of the advecting rural inversion [128]. In the case of Turin, this effect looks very weak, about 0.25°C at the most and it is statistically significant above 250 m a.g.l. for summer and just between 250-350 m a.g.l. during autumn (see Appendix B).

Differently from Turin, the summer cross-over effect observed in New York [132] is between 300 m and 500 m a.g.l. only. This is most likely due not only to the much bigger size of New York than Turin, but also to its proximity to the ocean, which promotes a larger exchange of air masses and tends to equalize the temperature profiles. Over Moscow, where 8 years of data are available [133], the nocturnal summer measurements indicate a UHI of 100-150 m a.g.l. and a positive ΔT of almost 2°C in the lowest level. In that case there was no evidence of a significant cross-over effect. On the contrary, Varentsov et al. (2018) [134] confirm the UHI elevation up to 200 m a.g.l. and the existence of a negative ΔT zone between 200-700 m a.g.l. over Moscow. Moreover, a recent study over Akademgorodok (Russia) showed a yearly mean UHI of 200-300 m a.g.l. and the presence of a cold lens [130]. A numerical study of vertical UHI over London [135] showed that the height of the nocturnal summer cross-over layer, from 22UTC to 07UTC, ranges from about 0.2 to 1 km a.g.l.: considering that London is appreciably larger than Turin, our observations are coherent with these data.

2.5 Conclusions

Turin is a city characterized by a quite complex orography, due to its proximity to the Po river, its enclosure among hills (East) and Alps (West), the exposure to the Föhn wind, and its location in the Po valley, which is critical for fog formation. In this work, the main objective was the description of the Urban Heat Island effect over the city with respect to its natural surroundings, by focusing on the mean seasonal variations of temperatures recorded in 14 years-long period. Five weather stations at the ground-level, three urban and two rural (one in the North and the other in the South of Turin), allowed us to study the Urban Canopy Layer UHI. We found that the UHI (i) is predominant during night hours, (ii) its mean values do not differ dramatically and significantly among the seasons, and (iii) its maximum intensity (with respect to both the North and South of the city) is recorded in the station of Consolata (URB1), which is on average 1°C warmer than the other two urban sites. This is due to its location in a highly urbanized and impervious area, which results in more heat trapped by the nearby buildings to be released at night. URB1 is also the weather station characterized by the most intense urban thermal pattern detected by Bassani et al. (2022) [43]. Another important feature is that the UHI effect is on average stronger along the city center-North direction than along the city center-South line, reaching a maximum of about 4.5-5°C during winter and summer nights.

The analysis of absolute humidity for the same ground-level weather stations featured the presence of an Urban Dry Island effect over Turin, which is always drier than the rural surroundings at daytime. The highest negative UDI values occur during summer nights, ranging from -3 g/m^3 in the South to -4 g/m^3 in the North of Turin. The city results slightly moister than the northern rural station only, reaching a peak of about 0.5 g/m^3 in winter nights.

The wind speed for which the UHI and UDI effects over Turin are swept out is about 3-4 m/s. This threshold value is lower than other cities placed in very different geographical contexts.

The availability of 14 years of data provided by three radiometers – one urban and two in rural northern and southern areas, respectively – allowed us to characterize also the vertical structure of the UHI effect and to highlight features of the Urban Boundary Layer not detectable by the ground stations only. Temperature measurements at the lowest atmospheric levels confirm that the highest UHI intensity occurs with respect to the rural area located North of the city. The upper levels showed that the urban

radiometer exhibits warmer temperatures than the rural ones up to about 150-200 m a.g.l.: this is the height up to which the influence of the city is perceived in the atmosphere, in line with other cities (e.g., New York and Montreal [27]). Above this height threshold the urban and rural vertical profiles get balanced on average, but still we observe a slight cold lens effect during summer above 250 m a.g.l. and in fall between 250 and 350 m a.g.l., which is a quite common phenomenon in presence of significant urban heat islands.

This study shows the non-trivial structure of the UHI effect on a city located in an orographically complex area and demonstrates the importance of combining the ground-level analysis of UHI-induced thermal singularities with the description (provided by radiometers) of the atmosphere above the city.

3

Evaluating the urban canopy scheme TERRA_URB in the COSMO model for selected European cities

The work presented in this chapter has been partially derived from Garbero et al. (2021) [73].
This paper is part of the collaboration between ARPA Piemonte and the Consortium for Small-scale Modeling (COSMO) [42]. It summarizes the results obtained within the COSMO Priority Tasks ÆVUS [136] and ÆVUS2: Analysis and Evaluation of TERRA_URB Scheme, which main aim were the implementation and the testing of the TERRA_URB parameterization into the COSMO model and involved researchers from five institutions: the Italian Aerospace Research Center (CIRA, Italy), ARPA Piemonte (Italy), Russian Hydrometeorological Center (RHM, Russia), German Weather Service (DWD, Germany) and the University of Ghent (Belgium).

3.1 Introduction

Urban areas have a significant impact on atmospheric flow and meteorological processes and this field of study is growing within the scientific community. One of the most investigated phenomena is the Urban Heat Island (UHI from now on), which occurs when a city experiences much warmer temperatures than its nearby rural area. The topic is of great public and scientific interest because urbanized surfaces are expanding throughout the world [137] and the number of urban residents will increase in the following years, according to the 2018 Revision of World Urbanization Prospects produced by the Population Division of the UN Department of Economic and Social Affairs [26]. Because of this, the impact of the UHI phenomenon is becoming more relevant and, according to IPCC's climate projections [138], this situation will aggravate in the next 80 years since a continued

increase in number, intensity and duration of heat waves during the 21st century is expected [139]. Indeed, many studies have already documented that UHIs tend to intensify during the heat waves (e.g., [140, 141]) leading to additional deterioration of the human thermal comfort [142, 143], amplification of heat-stress hazards, and even increase of heat-related mortality in the cities [88, 144]. Higher rates of climate warming and heat stress increase in the 21st century are expected for urban areas in comparison to rural background, according to regional [145, 146] or global [147] urban climate projections. The correct representation of UHI in numerical models is then a crucial aspect for Numerical Weather Prediction (NWP) applications and regional climate simulations. An adequate representation of urban areas in NWP models is essential to correctly forecast not only air temperature, UHI and human heat stress, but also dangerous weather events such as heavy rain and thunderstorms, which may be triggered or modified by urban-induced effects. There are studies [148, 149] suggesting that urban heat island-induced circulation is able to modify the boundary layer over a city, affecting the precipitation pattern. The urban heat island effect could give rise to a more unstable atmosphere, producing an increase of extreme precipitation larger than in nearby rural areas [150]. This effect is more evident over the tropics. For instance, in Singapore, the urban area leads to the formation of a rainfall "hot spot" which is responsible for 20–30% of the afternoon/evening total precipitation [151]. On the other hand, the humidity could be lowered, creating an urban dry island over a city, during the day particularly, and the local circulation could be modified [152, 153]. The standard classification separates the canopy layer UHI, measured by in-situ meteorological stations (using 2m temperature), and the surface UHI (SUHI), measured by means of remote sensors (using land surface temperature—LST). The UHI is more essential than SUHI when dealing with health impacts, since air temperature has a closer relationship with the urban environment and is essential for any assessment of urban heat reduction efficiency [154]. Nevertheless, given the progress in remote sensing and spatial science, more and more studies [155] consider SUHI which is able to provide a more detailed spatial pattern. In this work we deal with UHI only, but SUHI will be the subject of further studies. The reproduction of urban climate features in NWP and regional climate studies is possible with the use of so-called urban canopy models (UCMs), which are needed to parameterize the interaction between the urbanized surface and the overlying atmosphere when individual buildings remain unresolved. A wide variety of UCMs have been developed over the last decades [156],

and their use is getting more and more common in high-resolution climate simulations as well as in NWP. Nowadays, several widely used atmospheric models already include the selection of UCMs of different complexity in their basic versions. For example, Weather Research and Forecasting (WRF) model is coupled separately with three different UCMs, a slab (SB), which considers buildings as increased roughness, a single-layer representation of the canopy (SL), and an advanced multi-level Building Environment Parameterization (BEP) [157, 158]. The three different types of UCMs are also available in the HIRLAM model [159, 160]. Numerous studies have already demonstrated the advances of urban climate modelling with UCMs. Simulations of London's meteorology using the Met Office Unified Model with a new surface energy-balance scheme to represent the urban surfaces, called MORUSES, show encouraging agreement with observations and identify the urban land-use fraction as the dominant factor [161]. Several studies with WRF model have been performed as well, using different UCMs. In Bucharest, the comparison of simulations with no urban parameterization scheme, a SL UCM (SLUCM) or a BEP demonstrated that the last better represents the UHI [162]. The same results were also found for Berlin in a recent work [163]. The further introduction of a Building Energy Model (BEM) coupled with BEP minimizes the RMSE for 2-m temperature and 2-m relative humidity in Barcelona [164]. In the basic version of the COSMO model [165], cities are represented as natural surfaces with an increased surface roughness length and a reduced vegetation cover. This representation is not very effective, since urban areas are still treated as water-permeable soil with aerodynamic, radiative and thermal parameters similar to the surrounding natural land. Different UCMs have been coupled to COSMO: the single layer urban canopy model TEB (Town Energy Balance), the most advanced multi-layer schemes Double-Canyon effect parameterization (DCEP) and BEP-Trees and the TERRA_URB (TU) bulk parameterization. TU offers an intrinsic representation of urban physics with modifications of the input data, soil module and land-atmosphere interactions. The effect of buildings on the surface-atmosphere interaction is described without resolving the energy budgets of the buildings themselves but parameterizing the impervious surface water balance, translating the 3D urban-canopy parameters into bulk parameters by Semi-empirical Urban canopy parameterization (SURY) [166] and using the externally calculated anthropogenic heat flux, which has been proved to be beneficial for the simulation of screen-level temperature [167]. TU scheme is the simplest one in comparison to other UCMs, however its simplicity and effectiveness

make it suitable to urban climate application. Despite the TU scheme is rather new, it has been already tested for different cities. Recent studies over Moscow megacity demonstrated the ability of the TU parameterization to capture the UHI and other urban-induced meso-climatic effects and confirmed that it is a useful tool for urban climate research, especially if the city-descriptive parameters are improved [168, 169]. Moreover, TU scheme has been already implemented in the high-resolution numerical weather forecasts for Moscow megacity with grid spacing of 1 km and 500 m within the framework of the COSMO-Ru system [170, 171]. The TU scheme has been previously evaluated offline (forced with observations) for Basel, Toulouse and Singapore [172, 173] and online (coupled to COSMO-CLM v5) for Berlin, Belgium and Kampala [146, 174–176]. The other UCMs in COSMO were tested less extensively, e.g., TEB was tested only over Berlin [177], DCEP over Zürich [178] and Berlin [179], BEP-Trees over Basel [180] and BEP with a Building Energy Model (BEP-BEM) over Berlin [181]. Currently, all listed UCMs are not available within the official (operational) COSMO version, but exist as parallel branches of the model code development, which are not synchronized with recent updates in the operational version. Due to the computational efficiency of the TU scheme and its encouraging evaluation results, the COSMO and CLM consortia decided to select it as the default urban parameterization. It is planned to include TU into the official COSMO code in the forthcoming unified model version 6.0, and latter to implement it into ICON (Icosahedral Nonhydrostatic Weather and Climate), the future operational model of the COSMO Consortium. This work focuses on the improvement that TU could provide to urban climate modelling. The aim of this paper is then an in-depth evaluation and verification of the performances of the recent COSMO version 5.05 with TU scheme [136] and new implemented physical parameterizations, such the ICON-like surface-layer turbulence scheme and the new formulation of the surface temperature. Since the goal of the urban scheme is to catch small-scale features, only high-resolution runs have been considered in order to verify its capabilities in reproducing the urban dynamics and specific phenomena, e.g., UHI. The validation was performed for 1- or 2-week selected periods over 3 European cities characterized by different environment and climate, namely the Moscow megacity in Russia and Turin and Naples in Italy. This Chapter is organized as follows: Section 3.2 contains a description of the model, with emphasis on the surface-layer turbulent schemes, the skin temperature scheme and the urban parameterization TU. Section 3.3 contains a description of the performed experiments, while results are

presented in Section 3.4 and conclusions in Section 3.5.

3.2 Model Description

The COSMO model [165, 182] is a nonhydrostatic limited-area atmospheric prediction model, which is developed and maintained by the COSMO consortium [42]. It is designed for both operational NWP and various scientific applications on the meso-β and meso-γ scale. The COSMO model is based on the primitive equations describing compressible flow in a moist atmosphere. A variety of physical processes, such as radiation, convection, turbulence, and land surface processes, are taken into account by parameterization schemes. The governing equations are integrated using the mode-splitting approach to split up the equations into a longer model time step for the processes on larger time scales such as advection and the tendencies from the physical parameterizations, and into a short time step for the fast sound wave processes. Several options for a two time-level second and third order Runge–Kutta split-explicit scheme are available [183].

3.2.1 Surface-Layer Turbulence Scheme

Current Formulation

The COSMO model implements the next-generation TKE-based surface-layer transfer scheme [165, 184]. The surface layer, which refers to the layer of air between the earth's surface and the lowest model level, is divided into a laminar-turbulent sublayer, a roughness layer and a constant-flux (or Prandtl) layer. The surface layer scheme is also intimately related to the TKE-based closures of the COSMO model (see Sections 3.3 and 3.4 in [165]). As a result, the surface layer does not need the empirical Monin–Obukhov stability functions (as in [185, 186]) for which the Obukhov stability parameter needs to be determined from an iterative procedure or a non-iterative approximation [187, 188]. It rather generates these functions using the dimensionless coefficients of the turbulence closure [189] (see Section 4.2 in [165]).

New Formulation

Since COSMO version 5.05, a new ICON-based physics has been implemented involving a different turbulence scheme [190]. One main extension of the vertical diffusion scheme is the formal separation of turbulence from

a potential non-turbulent component of the sub-grid scale energy spectrum. This separation is related to additional scale interaction terms in the prognostic TKE equation which describe additional shear production of TKE by the action of other, non-turbulent, sub-grid scale flow patterns, such as wakes generated by sub-grid scale orography [191], convective currents or separated horizontal circulations. Through this formalism, the scheme describes separated turbulence interacting with non-turbulent circulations which allows for a consistent application of turbulence closure assumptions, even though other sub-grid scale processes may be dominant within the grid cell. One of the significant shortcomings of the older turbulence scheme is related with constant values of minimum vertical diffusion coefficients for momentum and scalars (tkmmin and tkhmin parameters), which are introduced in the model to prevent the turbulence from decaying in stable conditions [192]. Such limitation results in artificial mixing in the model leading to warm nocturnal temperature biases [171, 192, 193]. The new turbulence scheme attempts to fix this problem by introducing a correction function for minimum values diffusion coefficients in dependence on Ri-number and height above the surface, together with a retuned value of tkmmin and tkhmin. Additionally, the new scheme is supplemented by fixed pattern-length scale pat_len (which is used in our additional TKE-source-term due to near surface heterogeneity) by an upper limit dependent on the standard deviation of sub-grid-orography height, together with a retuned value for pat_len. With these modifications there is less artificial mixing at stable stratification and hence a stronger drop of near-surface temperature during night, as well as a stronger and shallower nocturnal surface inversion (Matthias Raschendorfer, personal communication).

3.2.2 Land Surface Scheme TERRA

The physical parameterization schemes include the multi-layer land surface model TERRA [182, 194]. It simulates the energy and water balance at the land surface and in the ground, providing the land surface temperature and humidity as lower boundary conditions for computing the energy and water fluxes between surface and atmosphere. In TERRA, all processes are modelled one-dimensionally in the vertical, no lateral interactions between adjacent soil columns are considered. The soil temperature is calculated by the heat conduction equation, while the soil water content is predicted by the Richards equation. Both equations are discretized by a multi-layer scheme. At the interface between surface and atmosphere, the surface energy balance equation is solved, yielding the new surface temperature.

The current representation of the surface temperature as well as the new skin temperature in TERRA are described in the following Subsections.

Current Formulation of Surface Temperature

In the current model version of TERRA, the surface temperature Ts is represented by the temperature of the uppermost soil layer [195]. The surface energy balance equation has the following form:

$$C_s \, \partial T_s / \partial t = RSW + RLW + LE + SE + G \tag{3.1}$$

where C_s is the heat capacity per unit area, and t is the time. RSW and RLW are the net shortwave and longwave radiation flux, respectively, while LE and SE denote the latent and sensible heat flux and G the ground heat flux.

New Formulation of Surface Temperature

The new description of the surface temperature in TERRA [195] is based on the skin temperature formulation by Viterbo and Beljaars [196]. They introduced an additional temperature of the canopy leaves, the skin temperature Tsk, as a representation of the vegetation in the surface energy balance:

$$\Lambda_{sk}(T_{sk} - T_s) = RSW + RLW + LE + SE \tag{3.2}$$

The behavior of this equation is mainly determined by the new parameter Λ_{sk}, the skin layer conductivity. Large values represent a strong coupling between the skin temperature T_{sk} and the surface temperature T_s, so that their diurnal cycles stay similar. In contrast, small values of Λ_{sk} describe a weak coupling and the diurnal cycle of T_{sk} can become considerably larger than the one of T_s. The leaves can become warmer during day and cooler during night. This can improve the surface temperature simulated by the soil-vegetation system.

TERRA_URB

Urban-atmosphere interactions are taken into account with the urban canopy model TU [166, 172]. The urban scheme considers the urban physics in terms of surface energy and moisture exchanges including the influence of street-canyon geometry. TU scheme provides the corrections of the surface parameters (roughness length, albedo, emissivity, heat capacity, etc.) within the framework of the TERRA module using the semi-empirical urban

canopy dependencies. TU integrates road, roof and wall surfaces into a 2D horizontal surface for which radiative and thermodynamic properties are adapted according to the 3D structure of the urban canopy. This is done through the Semi-empirical Urban canopy parametrization (SURY), which translates 3D urban canopy into bulk surface parameters [166]. In order to describe the 3D urban canopy for urban tiles, TU requires the definition of several urban canopy parameters for each grid cell of the model, including impervious surface area fraction (ISA), building area fraction (BF), mean building height (H) and height-to-width ratio (H/W). The anthropogenic heat flux (AHF) is also taken into account according to Flanner [197], assuming annual-mean values together with the typical diurnal and annual variations and the dependence of its annual amplitude on the latitude. TU also represents the water puddles on impervious surfaces in the urban environment at which storage, run-off and evaporation of precipitated water occurs [172]. To describe the heterogeneity of the urban surface, TU implements the so-called tile approach, for which urbanized and natural parts can coexist in each grid cell of the model. The fraction of urban area in a tile is defined by the ISA parameter. Hence, near-surface temperature values, heat fluxes and other soil or surface variables are simulated separately for natural and urban tiles in each grid cell of the model. The average values for each grid cell are calculated according to the area fraction of urban and natural tiles, and to annual-mean anthropogenic heat flux (AHF).

External Parameters

The external input parameters for TERRA are provided by the external parameter pre-processor EXTPAR and are aggregated from various raw datasets describing land use, orography, soil, etc. [198]. For the urban surfaces, EXTPAR, by default, uses AHF data from Flanner [197], ISA from Elvidge et al. [199] for global cities and the "degree of soil sealing product" from EEA [200] for European cities. However, the use of these datasets in combination with Globcover 2009 land use classes [201] leads to inconsistencies for the urban surfaces, which affect a number of time-invariant natural land cover parameters (root depth, stomatal resistance, roughness length, minimum and maximum land cover, skin conductivity, emissivity, and leaf area index). This so-called 'urban double-counting effect' requires an additional pre-processing step, explained in detail in Appendix C, Section C.1. Since the reported simulations in the current study use different data sources to describe the urban canopy parameters, this information is provided in more detail in Section 3.3 for each case study.

3.3 Experiments

The COSMO model has been used at high resolution to perform simulations in 3 different cities in Europe, namely Turin and Naples in Italy and Moscow in Russia, on selected periods characterized by heat waves or intense heat islands (see Tab. 3.1). Even if the study weeks differ among the domains, due to different background and meteorological conditions, the model has been configured as consistently as possible across the various cities. Firstly, each area experienced high-pressure conditions and absence of rainfall and wind, favorable for UHI appearance. In addition, the final grid spacing adopted was 1 km for all the three domains and the lowest model level was equal to 10 m in each case. The model set up and the corresponding namelist switches were derived from the COSMO User's Guide [190], which recommends values for both the conservative (old COSMO physics) and the advanced (new ICON physics) approach. The model set up for Moscow was close to other partners' configurations with minor differences, determined by previous experience in COSMO simulations for this region. An additional scaling coefficient of 2.5 was introduced for the rooting depth to avoid dry and hot bias temperature bias, which is typical for hot summers in the European part of Russia [202]. In TERRA look-up tables the rooting depth does not exceed 1 m even for the forests, which is a significant underestimation in comparison to observations [203–205]. Previously, a positive effect from such engineering was found for tropical Africa [206] as well as for the Moscow region [168]. Additionally, the scale of subgrid thermal inhomogeneity (pat_len parameter) in the simulations adopting the ICON-like turbulence was set to 100 m instead of 750 m (as in the Italian domains), in order to better represent the nocturnal temperatures. It was verified that the adoption of pat_len = 100 m for Turin and Naples has no effect at all on the results (not shown here).

The information about the simulation workflow and resolution are summarized in Table. 3.1 for the three domains. As regards the city-descriptive external parameters for TU, they are provided by EXTPAR for the Piedmont and Campania domains. Even if a better characterization of the urban parameters could be done, and it will be the subject of further studies, they were the only available data when the present simulations were started. In any case we believe that they are acceptable approximations of reality for these areas. Morphological urban canopy parameters, thermal and radiative parameters of urban environment were set by the defaults from [166]. For Moscow, default EXTPAR output on ISA and AHF was found to be too coarse and unrealistic [207], which was a motivation for incorporating a

Table 3.1: Setup of the simulations.

	Turin, Piedmont domain, Italy	**Naples, Campania domain, Italy**	**Moscow Megacity Russia**
Model setup	2 nested domains: 3500 × 2750 km over Europe (5 km grid spacing); 350 × 350 km (1 km grid spacing) centered around Turin	1 single domain centered around Naples: 260 × 138 km (1 km grid spacing)	2 nested domains centered around Moscow: 720 × 720 km (3 km grid spacing); 200 × 200 km (1 km grid spacing)
Initial and boundary conditions	Taken from the Integrated Forecast System (IFS) analysis (9 km grid spacing)	Same as Turin	Taken from the ICON analysis (13 km grid spacing)
Study period	22-29 October 2017	8-14 August 2017	1-16 June 2019
Number of vertical levels	65	60	50
Lowest model level	10 m	10 m	10 m

more advanced GIS-based approach to derive the city-descriptive parameters. ISA and morphological urban canopy parameters for Moscow were obtained based on GIS-processed vector OpenStreetMap data on buildings and roads, vegetation mask derived from Sentinel-2 satellite imagery with 10-m resolution and the recent Copernicus Global Land Cover raster dataset with 100-m resolution. Anthropogenic heat flux was defined based on a literature estimate of its city-mean value from [208] and re-distributed over the area based on building area fraction and height. More details about this approach are given in [209], while its advantages over default EXTPAR output was already demonstrated for Moscow in model simulations for different seasons [207]. Specifically, in this study we used REF1 data set from [207]. Thermal and radiative parameters of urban environment were taken from [166], in line with the other two regions. Different model configurations have been tested in order to assess the one that better reproduces the observed values. Specifically, the capabilities of TU scheme in reproducing the UHI effect was evaluated by comparing reference simulations without the urban parameterization (lterra_urb = FALSE) with simulations in which TU was activated (lterra_urb = TRUE). Additional sensitivity tests were then performed to evaluate the current and icon-like formulation of the turbulence scheme (loldtur = TRUE/FALSE) and the new skin temperature scheme

compared to the current formulation of surface temperature (itype_canopy = 2/1). Summarizing, six configuration model settings have been tested over the three domains, which are described in Tab. 3.2.

Table 3.2: Model configuration settings.

Namelist switch	**Configuration explanation**	REFold	REFnew	TUold1	TUold2	TUnew1	TUnew2
loldtur	Old (TRUE) or ICON-based (FALSE) turbulence scheme	TRUE	FALSE	TRUE	TRUE	FALSE	FALSE
lterra_urb	TU scheme switched on (TRUE) or off (FALSE)	FALSE	FALSE	TRUE	TRUE	TRUE	TRUE
itype_canopy	Current formulation (1) or skin temperature scheme (2)	1	1	1	2	1	2

The model validation for Turin was carried out by using the hourly data provided by the ARPA Piemonte network (Fig. 3.1a). The analysis focused on six stations, three urban and three rural, located at similar elevation above the sea level, as described in Chapter 1. The urban ones comprehend both the historical city center and suburbs, with an impervious surface area above 0.60 (for details see Tab. C.1 in Appendix C). The rural stations are chosen in the southern surroundings of the urban area, since Turin is enclosed by mountains in the north-western sector and by hills in the eastern part. The modelled values used for validation purposes have been calculated for each station using a bilinear method and refer to the values interpolated from the values of the four nearest raster cells.

The model validation for Naples has been carried out by using the hourly observational data provided by the Civil Protection network of Campania. In this domain, five stations were considered, two urban and three rural (Fig. 3.1b). The urban ones are located in Naples and S. Marco Evangelista. The second one has been chosen in order to reduce the effects of the proximity to the sea with respect to Naples. They are both characterized by an impervious surface area above 0.60 (Tab. C.2, Appendix C). The rural stations are chosen respectively in Grazzanise, Rocca D'Evandro and Alife. The simulated values used for validation purposes have been obtained for each station with a bilinear method.

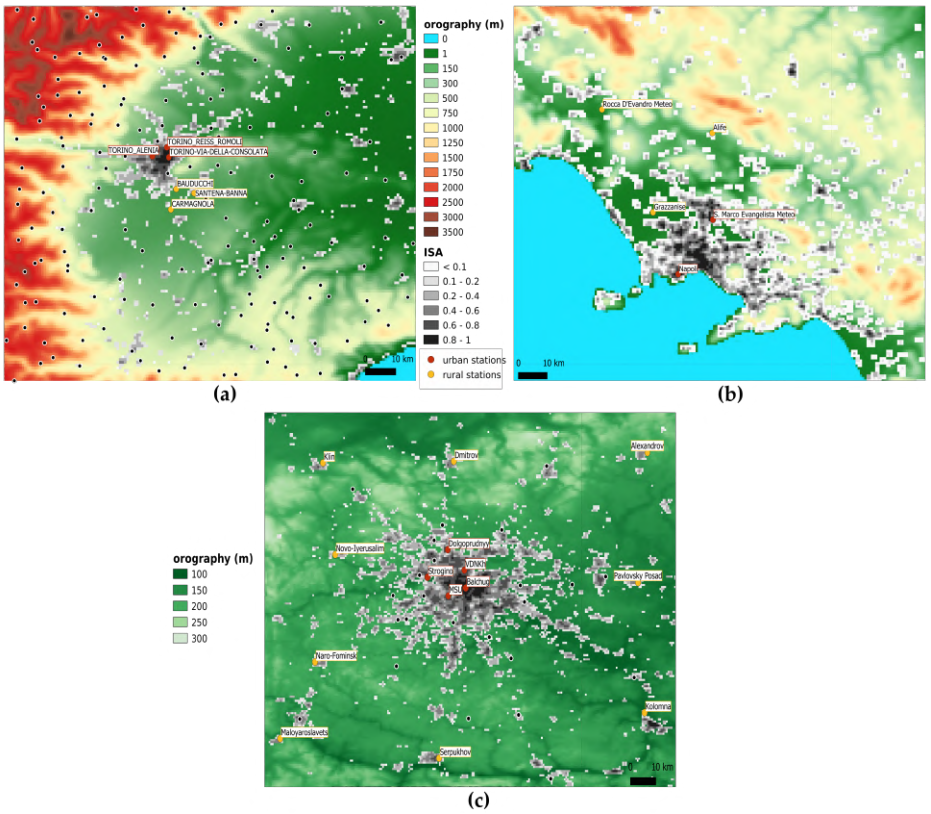

Figure 3.1: **(a)** Piedmont domain, Italy: the black marks indicate all the stations of the Arpa Piemonte network; **(b)** Campania domain, Italy. Observations are provided by the Civil Protection of Campania; **(c)** Moscow domain, Russia: the black marks indicate the Roshydromet network (WMO) that include 43 weather stations. For all three domains, the urban stations considered in the analysis are shown with red markers, while the stations selected to calculate the mean rural temperature are shown with yellow markers.

The model validation for Moscow was performed using observational data on 1-hourly intervals from the Roshydromet network that include 42 weather stations (Fig. 3.1c). Stations from uncertified networks, used in previous studies for Moscow, are not used in this study. Most of the stations are in the countryside, in relatively small towns or in airports, so we further consider them as rural. Five stations are considered as urban, i.e., representing the urbanized area within Moscow megacity. These stations are located in different urban environments, e.g., Balchug station in a densely built area in the historical city center, Strogino and Dolgoprudny in residential areas with newer development at the periphery of the megacity, MSU and VDNKh in

urban parks. According to the previous studies, all these stations experience higher temperatures than rural surroundings, with the most intense UHI observed for Balchug weather station in the city center [169, 210]. Since many stations in Moscow are located in inhomogeneous environment (e.g., at the border between urban park and build areas, which is a case for MSU and VDNKh stations), the procedure of grid cell assignment for Moscow was a bit more complicated than for other study areas. For each station, one model grid cell was selected among 4 nearest ones taking into account real and modelled settings of the station's environment (e.g., if the station is located in a park area, the grid cell with lower ISA is selected). If more than one among four nearest cells corresponds to the actual local settings of the station, the one with smallest temperature RMSE is selected.

More specific information about the stations used for validation purposes are provided in Appendix C for each of the three domains.

3.4 Results

In order to evaluate the configuration that better suits the observations and therefore which of the six parameterizations is able to better capture and reproduce the UHI phenomenon, the same statistical evaluations were performed over the different domains. The air temperature and how it evolves is the most effective parameter to detect the UHI effect. During the day, a city stores heat, which is then released at night, resulting in warmer urban temperatures than its rural surroundings. Then, the dynamics of observed and modelled 2-m temperature (T2m) was analyzed for urban and rural stations both over the entire study period and in their mean daily cycle. In a similar manner the dynamics of the UHI intensity, defined as the difference between urban and rural temperature, was investigated. A unified set of statistical indices was calculated for all domains in order to evaluate the performance of the different model configurations. The mean daily evolution of Mean Bias (MB) and Root Mean Square Error (RMSE) of T2m, evaluated both over rural and urban stations, and of UHI intensity are plotted and allow to identify the configuration that better reproduces the urban features. Taylor diagrams are shown for T2m, referred to both rural and urban stations, and for UHI intensity and provide a concise statistical summary of how well patterns match each other in terms of their correlation, their root-mean-square difference and the ratio of their variances.

3.4.1 Turin

The UHI intensity is calculated as the difference between the mean urban temperature, obtained averaging temperature of the three selected stations in the city, and the mean rural temperature, i.e., the average of the three selected stations surrounding Turin (Fig. 3.1a).

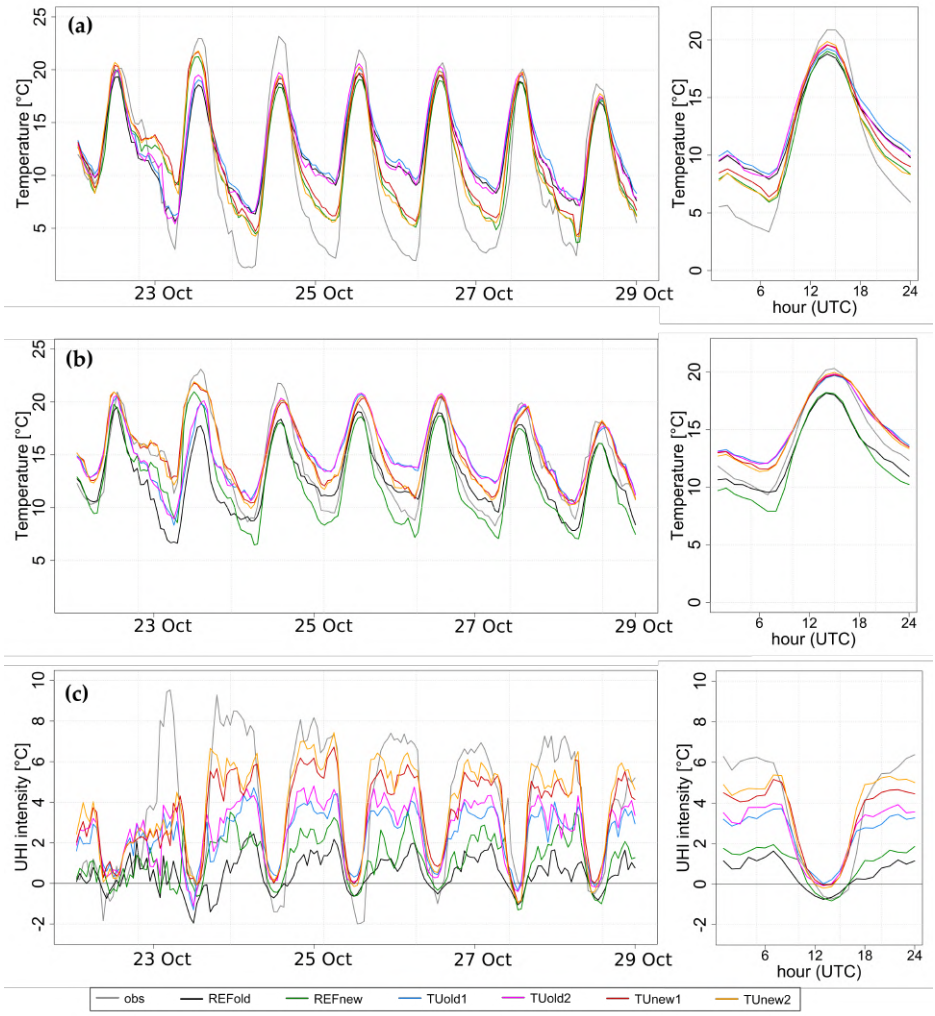

Figure 3.2: **(a)** Mean rural T2m, **(b)** mean urban T2m and **(c)** Urban Heat Island (UHI) intensity during the week 22-29 October 2017. Subplots on the right show the mean daily cycle of the rural temperature and UHI intensity.

The hourly values of T2m, both for rural and urban areas, have been

analyzed for the considered period in October 2017 and evaluated in their mean daily cycle. Although minimum temperatures are rather overestimated and maximum temperatures are slightly underestimated, the characteristic oscillating pattern is well reproduced by all configurations (Fig. 3.2a,b). Simulations with the current turbulence scheme experience the highest nocturnal bias, with values more than 4°C, and worst diurnal and nocturnal RMSE (Fig. 3.3a,d). The adoption of the ICON-like physics and skin-layer temperature scheme decreases nocturnal temperatures and partially reduces positive nocturnal bias up to 2°C, improving also the RMSE (Fig. 3.3d). The new formulation of turbulence scheme has also a minor impact on the maximum daily temperature, as highlighted by better scores. The activation of the TU scheme has no significant impact on rural temperatures, as expected, and the small differences could be attributed to the proximity of urban settlements. A major impact can be noted on urban temperatures, as the TU scheme induces warmer temperatures than reference simulations (black and green lines). It is worth noting that there is an evident overestimation of the model of the nocturnal temperature, which is partially compensated in the urban stations due to the UHI effect: the reference simulations (without TU) get better scores during night, since the positive model bias fictitiously reproduces the effect of the heat island at night. For this reason, we analyzed the UHI intensity, which eliminates any possible bias or systematic error by being the difference between two temperatures. Figure 3.2c demonstrates the ability of the TU scheme in capturing the dynamics of the UHI intensity, since the results that come closest to the observations concern TU configurations. The fact that the TU scheme improves the representation of the UHI is also confirmed by the better scores obtained by the configurations using the urban scheme (Fig. 3.3c,f). Among the runs with TU, significant improvements are provided by adopting the new turbulence and the skin temperature schemes, as confirmed by the best scores for urban temperature and UHI intensity. Nevertheless, a significant overestimation of nocturnal temperatures remains also in the best configuration (TUnew2, yellow line), due to the positive model bias we discussed above. A possible explanation of this systematic error could be related to the double nesting domains or to the external urban parameters and it will be furtherly investigated.

The correlation between modelled and observed data is shown in the Taylor diagrams (Fig. 3.4). They show the strong improvement provided by the new turbulence scheme in forecasting rural and urban temperatures. If we focus on the UHI intensity, the correlation between model and observa-

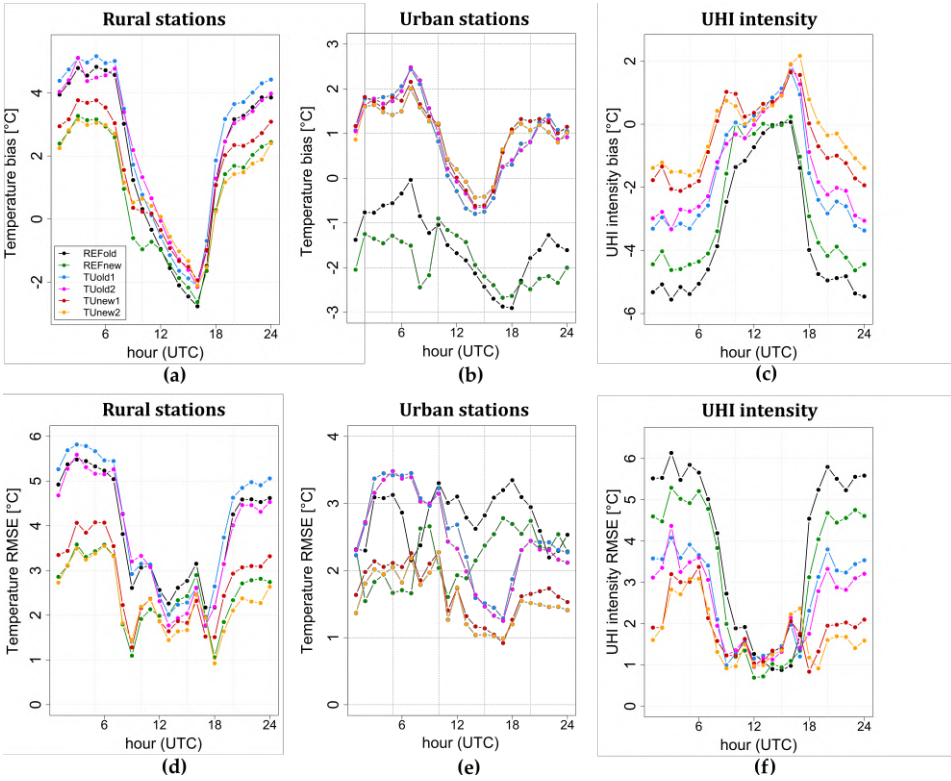

Figure 3.3: Mean biases and root-mean square errors of T2m, evaluated over rural **(a,d)** and urban **(b,e)** stations in the Piedmont study area; mean biases and root-mean square errors of UHI intensity for urban stations **(c,f)**.

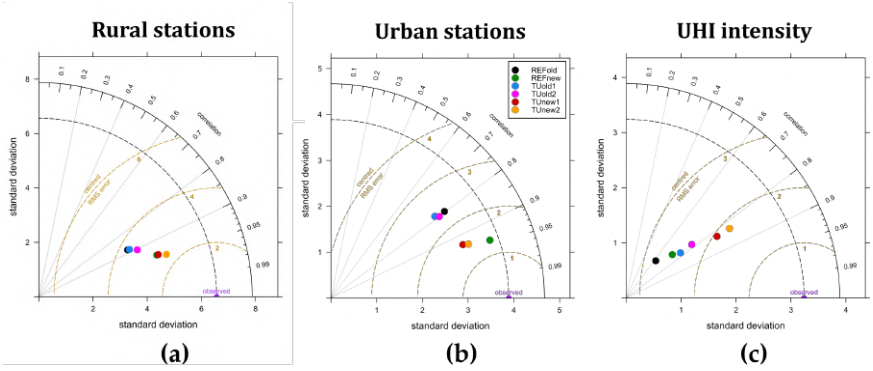

Figure 3.4: Taylor diagrams for rural stations **(a)**, urban stations **(b)** and UHI intensity **(c)**.

tions increases from 0.6 to 0.83 and the RMS error gradually decreases by

activating TU scheme, adopting the ICON-like physics and skin temperature scheme. This result confirms that the TUnew2 is the configuration that better captures and reproduces the UHI effect.

3.4.2 Naples and Moscow

The hourly values of the two-meter temperatures have been analyzed over the week 8–14 August 2017 for the Naples domain and evaluated in their mean daily cycle. The behavior of the rural stations (average values among the three stations) is displayed in Fig. C.1a (see Appendix C, Section C.3). The characteristic oscillating pattern reveals that, during daytime, peaks up to 38°C are reached, while during the night the temperature decreases up to 18°C. In general, this pattern is well captured by all the configurations, even if in the first three days of simulation the maximum values are largely underestimated. The new turbulence scheme provides a sensible reduction of the minimum nocturnal values with significant performance improvement, as confirmed by MB and RMSE values for rural stations (Fig. C.2a,d in Appendix C). In rural sites, as expected, the activation of TU does not produce remarkable effects. On the other side, TU improves the representation of nocturnal values in urban stations, especially when the skin temperature scheme is activated. The hourly UHI intensity, computed as the difference between the mean temperature urban value and the mean temperature rural value, is well reproduced when TU is activated (Fig. C.1c, Appendix C), as confirmed by MB values less than 1.2°C.

Taylor diagrams (Fig. C.3, Appendix C) show a good correlation value – about 0.95 – between the modelled and the observed data, both in urban and rural sites with all the configurations. Moreover, in urban stations all the simulations are characterized by a standard deviation generally lower than the observed one, with a better agreement achieved with the new turbulent scheme. The RMSE value is close to 1 for all the configurations. In rural stations the usage of TU causes an unexpected increase of the standard deviation and of RMSE values. The Taylor diagram related to UHI intensity provides interesting findings. In fact, the standard deviation gradually increases from the minimum value with the reference configuration to a value close to the observational one when TU is employed (TUnew1 and TUnew2). These configurations also provide the best values of correlation and RMSE.

Model evaluation for Moscow domain was performed separately for 30 stations located outside urban environment at the distance of more than

25 km from the Moscow city center (further referred as rural neither they may be also affected by local anthropogenic effects due to their location near smaller cities or within sparsely built rural/suburban settlements), and for five urban stations, located within the megacity in the different types of urban environment. Among them, special attention is given to Balchug weather station in the city center, since it is the only one located within a relatively homogeneous dense urban environment and experiences higher temperatures than other urban stations. UHI intensity for Moscow is defined for each individual weather station as a temperature difference between this station and mean rural temperature, calculated for 9 selected stations surrounding Moscow. Same approach was used in previous studies for Moscow [168, 169, 171]. For the considered study period in June 2019, all model runs capture the basic patterns of the rural temperature dynamics, and a typical summer daily temperature cycle (Fig. C.4, Appendix C). As for other regions, the model overestimates nocturnal temperatures (at 0 and 21 UTC) in the runs with old physics, with worst MB more than 1.5°C in TUold1 simulation (Fig. C.5, Appendix C). Simulations with old physics also demonstrate the highest daytime bias. The use of the new turbulence scheme and skin-layer temperature scheme decreases nocturnal temperatures and partially, but not fully eliminates positive nocturnal bias and improves RMSE (Fig. C.5a,c, Appendix C). It should be noted that model sensitivity to the change of physical schemes is smaller than for Turin and Naples, which may be associated with weather conditions or with flat terrain in the Moscow region, as well as with a larger number of rural weather stations used in analysis. Switching on TU scheme makes a small, but noticeable impact on rural temperatures since some rural stations are still affected by nearby settlements.

As in previous modelling studies for Moscow [168, 169, 171], the model runs with TU nicely captures the dynamics of the air temperature in the city center, UHI intensity and its daily turn (Fig. C.4b,c, Appendix C). On the contrary, simulations without TU do not reproduce even a part of urban-induced temperature anomaly. The differences between UHI intensity in the runs with TU and different physical schemes are consistent with other regions, although the model sensitivity is less than for other study regions: the strongest UHI is experienced in TUnew2 run and the weakest in TUold1/2 runs. Not surprisingly, runs without TU provide the worst evaluation scores for temperature and UHI intensity for urban stations (Fig. C.5, Appendix C). Among the runs with TU, simulations with new turbulence provide the best scores during the most part of the day. TUnew2

simulation provides the best scores for UHI intensity at night and morning, since it is the only one which fully captures nocturnal maximum of UHI intensity (Fig. C.4c, Appendix C). However, this run performs worse in the evening (at 15–20 UTC) due to the phase shift between modelled and observed UHI daily cycle (Fig. C.4b, Appendix C). Such phase shift is also observed for Turin and may be associated with specific microclimatic features within the urban canopy layer, which remain unresolved in TU, as well with shortcomings the ABL scheme in the model.

Taylor diagrams on Fig. C.6 (see Appendix C) confirm that there is only a minor difference between the model runs for rural temperature, with slightly better correlation for TUnew1/2 runs with new turbulence. The difference between the runs becomes more noticeable if considering urban stations or specifically Balchug station in the city center (Fig. C.6b,c, Appendix C) where TUnew1/2 runs are again the best in terms of the air temperature. The difference between the model runs becomes even more noticeable when considering the UHI intensity for all urban weather stations and for the city center. In both cases, the TUnew2 run becomes the best one in terms of correlation coefficient and standard deviation.

3.5 Conclusions

This Chapter presents evaluation results of the TERRA_URB scheme in high-resolution simulations with a recent COSMO model version for selected European cities, namely Turin, Naples and Moscow. Additional sensitivity tests have been performed in order to evaluate the ICON-like turbulence scheme developed in COSMO and the use of a new skin-layer temperature scheme. The novelty of the work in comparison with previous TU evaluation studies lies in the use of the recent model version, and in the uniform approach for setting up numerical experiments and their evaluation applied for all different cities. Even if the three domains are morphologically different and the stations for data validation do not share the same properties in Turin, Naples and Moscow, the outcomes follow a common behavior. This similarity in such different morphological conditions points out that the finding is not due to specific model calibration but has a universal meaning. The effect of TU combined with the ICON-like turbulence and skin temperature schemes provides a substantial improvement in capturing the UHI intensity and improving air temperature forecasts for urban areas. It should be noted that model sensitivity to the change of physical schemes is smaller for Moscow than for Turin and Naples, which may be associated

with weather conditions or with flat terrain in the Moscow domain, as well as with a larger number of rural weather stations used for the validation. In comparison with other urban canopy schemes, TU is much simpler, but provides reasonable results for three cities considered in our study and for more cities in previous studies (e.g., [146, 171–174, 176]). Additionally, it realistically represents urban effects in the lower atmosphere by capturing the urban-induced modification of precipitation patters. The scheme simplicity together with encouraging verification results for these three cities strongly supports the use of TU scheme in operational weather forecast, as it is already done for Moscow [171]. This study is limited to the canopy-layer UHI effect, while it would be better to have a more comprehensive view of other urban-induced climatic and atmospheric effects, including SUHI and urban effects on air humidity and wind. Further verification studies should involve satellite-retrieved land surface temperatures and urban/rural observations on other meteorological parameters. Moreover, a better evaluation of the PBL structure by means of temperature and wind stratification is needed. Among the case study cities, Moscow and Turin provides opportunities for further in-depth model verification due to the presence of temperature profiler networks. Moreover, sodar wind profilers are available in Moscow, Turin and Naples. The presence of necessary observations together with experience of effective collaborative work will allow to consider these three cities as a cross-border test bed for further deeper model evaluation studies. The TU scheme has been implemented in the main branch of COSMO development under the latest version 6.0, which simplifies its use in NWP and climate modelling tasks. Since in the COSMO Consortium it is planned the migration to ICON model, which will be the future operational model, a special attention will be devoted to the porting of the scheme into ICON.

Part II

The Rayleigh-Bénard problem

4

Rayleigh-Bénard convection with thermal boundary inhomogeneities

The work presented in this chapter has been partially derived from Bassani et al. (2022) [211].

4.1 Introduction

Rayleigh-Bénard (RB) convection [37, 38] is one of the simplest, most studied and paradigmatic examples of thermal convection [212–220]. RB experiments and numerical simulations have traditionally focused on a configuration with thermally homogeneous top and bottom plates. However, boundary inhomogeneities play a crucial role in a number of real cases, e.g. in mantle convection, involving the continental and the oceanic lithosphere [221, 222], in sea convection under floating ice [223, 224], and in air convection over cities surrounded by rural lands [225]. Some works have investigated heterogeneous temperature boundary conditions (b.c.) on one wall only. Ripesi et al. [226] studied alternating thermal insulating and conducting patches on the upper plate in two-dimensions (2D), with a later extension in 3D by Bakhuis et al. [227]. Ostilla-Mónico and Amritkar [228] found a relationship between heat transport intensity and the wavelength of adiabatic-conducting stripe pairs. A recent numerical experiment, with inhomogeneities on the lower boundary, simulated a three dimensional cavity [229], demonstrating that non-uniform heating strongly affects the dynamics and structure of large-scale circulation. The effects of non-uniform b.c. on both plates were investigated by Kelly and Pal [230] and Yoo and Moon [231], but for relatively low Rayleigh numbers. All the previous works show that inhomogeneities in thermal boundaries can induce structural changes in RB convection. However, a systematic analysis of non-uniform temperature conditions on both top and bottom boundaries, in the fully turbulent regime,

is missing. Are the boundary inhomogeneities able to impose their own scales on the convection? How do these interact with the self-organized large-scale structures emerging from turbulent convection [40, 41, 232–235]? In order to shed light on this topic, we study top and bottom sinusoidal temperature perturbations in 3D and 2D numerical simulations, exploring a broad range of wavelengths.

4.2 Numerical model

We consider the classical Rayleigh-Bénard configuration, with an incompressible fluid confined between two horizontal, rigid plates, kept at fixed temperatures, with the bottom surface warmer than the top one. Considering the position vector $\mathbf{x} = (x, y, z)$, with z the vertical coordinate, the fields are: velocity $\mathbf{u}(\mathbf{x}, t) = (u, v, w)$, temperature $T(\mathbf{x}, t)$ and pressure $p(\mathbf{x}, t)$. The variables are non dimensionalized through the temperature difference between the plates $\Delta\tilde{T}$, the layer thickness $\tilde{d}$ and the time $\tilde{\tau}_{conv}$ (the tilde indicates dimensional quantities). The latter represents the convective timescale, given by $\tilde{\tau}_{conv} = \sqrt{\tilde{d}/(g\alpha\Delta\tilde{T})}$, where g is the gravity acceleration and α the thermal expansion coefficient. Under the Boussinesq approximation [37, 218] the equations read

$$\frac{\partial \mathbf{u}}{\partial t} + \mathbf{u}\cdot\nabla\mathbf{u} = -\nabla p + T\hat{\mathbf{z}} + \left(\frac{\sigma}{R}\right)^{1/2}\nabla^2\mathbf{u} \tag{4.1}$$

$$\nabla\cdot\mathbf{u} = 0 \tag{4.2}$$

$$\frac{\partial T}{\partial t} + \mathbf{u}\cdot\nabla T = \frac{1}{(\sigma\, R)^2}\nabla^2 T \tag{4.3}$$

where $\hat{\mathbf{z}}$ is the vertical versor, $\sigma = \nu/\kappa$ is the Prandtl number (kinematic viscosity to thermal diffusivity ratio), and the Rayleigh number $R = g\alpha\Delta\tilde{T}\tilde{d}^3/(\nu\kappa)$. In all simulations, we set $\sigma = 0.71$ (air) and $R = 10^7$.

The numerical code employed for integrating Eqs. (4.1–4.3) is spectral with 4/5 dealiasing in the planar directions and with second-order finite differencing in the vertical, with a non-uniform grid and a third-order fractional step method in time [41, 236, 237], available on GitHub [238]. We use 193 grid points along z, while the horizontal resolution is $4\pi/512$ in all experiments. Part of the computational resources were provided by HPC@POLITO [239].

4.2.1 Tested configurations

Periodic b.c. are set in the horizontal directions and z ranges between 0 and 1. The aspect ratio L (the ratio of the planar size of the domain and its thickness $\tilde{d}$) is set to 4π and 8π in 3D and to 32π in 2D. We perform simulations for both no-slip ($\mathbf{u}|_{z=0,1}= 0$) and free-slip ($\partial u/\partial z|_{z=0,1}= \partial v/\partial z|_{z=0,1}= w|_{z=0,1}= 0$) velocity conditions at the top and bottom boundaries.

Thermal b.c. imposed at both plates are $T_b = A\ \sin(\mathbf{k}\cdot\mathbf{x})+\overline{T}$ (hereinafter subscript b indicates variables at boundaries), with amplitude $A = 0.25$ and mean $\overline{T} = 0.5$ and $\overline{T} = -0.5$ at the lower and upper boundaries respectively. $\mathbf{k} = (k_x, k_y)$ is the wave number vector of the temperature perturbation, where $k_x = k_y \equiv k_b$. Top and bottom sinusoidal patterns are in phase, so that $\Delta T = 1$ everywhere (in this way, also the local effective R is not altered). Figure 4.1 shows a schematic representation of the RB system studied here, with respect to the classical one. In order to explore different heterogeneity scales, the wavelength $\lambda_b = 2\pi/k_b$ is changed as reported in Tab. 4.1 (the homogeneous case $k_b = 0$ is also investigated).

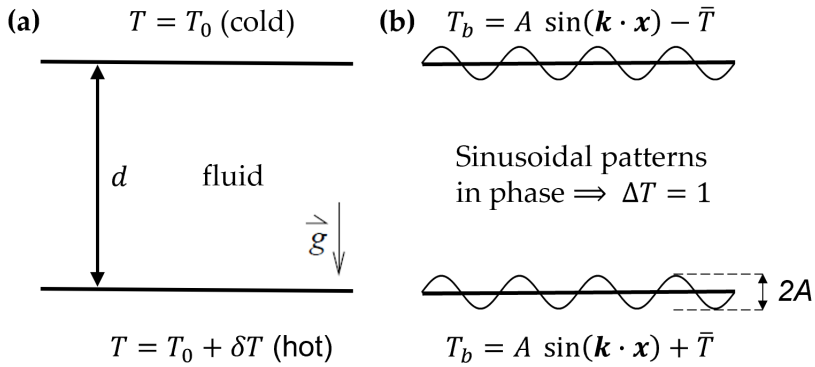

Figure 4.1: Schematic representation of the Rayleigh-Bénard configuration, with (**a**) uniform boundary conditions and (**b**) thermal b.c. (sinusoidal patterns in phase).

4.3 Results

4.3.1 3D

In a homogeneous three-dimensional RB configuration, plumes are known to organize themselves into clusters [41]. After an initial transient, the aggregation among horizontal large-scale structures reaches a statistically

Table 4.1: Wave numbers k_b and wavelengths λ_b of the sinusoidal temperature boundary conditions, for the 2D ($L = 32\pi$) and 3D ($L = 4\pi$ and $L = 8\pi$) domains.

L = 32π (2D)		**L = 4π (3D)**		**L = 8π (3D)**	
k_b	λ_b	k_b	λ_b	k_b	λ_b
0.00625	32π	0.5	4π	0.25	8π
0.125	16π	1	2π		
0.25	8π	1.5	$4\pi/3$		
0.5	4π	2	π		
1	2π	2.5	$4\pi/5$		
1.5	$4\pi/3$	3	$2\pi/3$		
2	π	3.5	$4\pi/7$		
2.5	$4\pi/5$	4	$2\pi/4$		
3	$2\pi/3$				
3.5	$4\pi/7$				
4	$2\pi/4$				
5	$2\pi/5$				
6	$2\pi/6$				

stationary state and the clustering is evident, as shown in Fig. 4.2a$_{1-3}$ for the no-slip cases (see also Fig. D.1a$_{1-3}$ in Appendix D, for free-slip conditions). Panel a$_1$, showing the temperature at midplane, clearly reveals the clustering of thermals of the same sign [233]. The snapshots of the vertical velocities w and the vertical heat fluxes in Fig. 4.2a$_{2-3}$ – calculated as the product between w and the temperature anomalies T' – show that intense w are associated with high positive values of wT' where warm (cold) structures are ascending (descending).

The clustering phenomenon is further highlighted by the horizontal power spectrum $E(k)$ of the kinetic energy $(u^2 + v^2 + w^2)/2$ (see the asterisks in Fig. 4.3a–c). The spectrum associated with the homogeneous case $k_b = 0$ peaks at the horizontal wave number $k_{so} \simeq 1$ (see the red asterisk), corresponding to wavelength $\lambda_{so} \simeq 2\pi$: this is the typical size of the large-scale patterns [233] emerging in Fig. 4.2a$_1$. Hereinafter, we refer to E_{so} for the energy spectrum peak value at the self-organized scale k_{so}. In the following, we show that the clustering-induced structures occur not only when the thermal b.c. are uniform, but also with inhomogeneities. In particular we explore (i) if non-homogeneous thermal boundary conditions are able to force novel convective structures and (ii) their interaction with the self-organized clusters already observed in the homogeneous case.

We begin with the two 3D cases where the wavelengths of the boundary inhomogeneities are comparable to the domain size: $\lambda_b = 8\pi$ ($k_b = 0.25$) in $L = 8\pi$ and $\lambda_b = 4\pi$ ($k_b = 0.5$) in $L = 4\pi$. The temperature fields

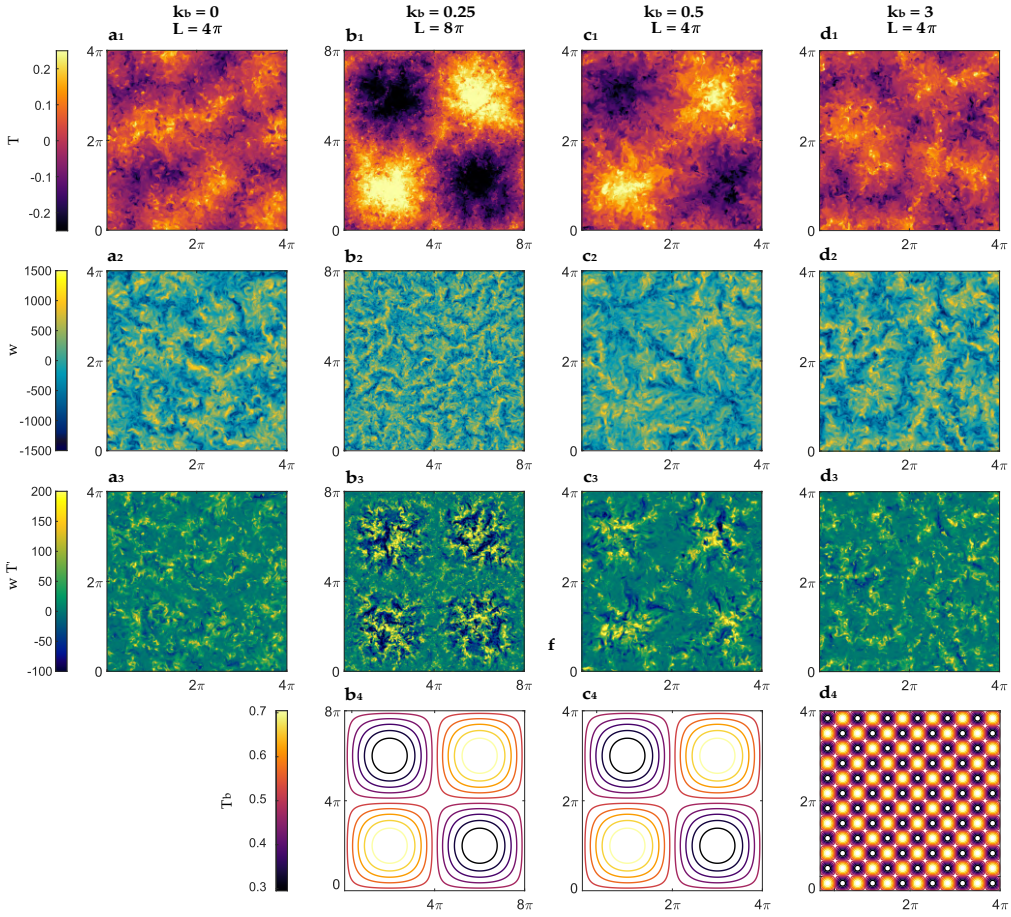

Figure 4.2: 3D simulations: snapshots at $z = 1/2$ and $\tau_{conv} = 180$ of the temperature perturbations T (first row, subscript 1), vertical velocity field w (subscript 2) and vertical flux wT' (subscript 3), under no-slip conditions. The panels $\mathbf{b_{1-3}}$ refer to the domain $L = 8\pi$, while $\mathbf{a_{1-3}}$, $\mathbf{c_{1-3}}$ and $\mathbf{d_{1-3}}$ correspond to $L = 4\pi$. Panels $\mathbf{b_4}$, $\mathbf{c_4}$, $\mathbf{d_4}$ provide a visualization (with isotherms) of the boundary conditions T_b at the bottom plate.

reported in Fig. 4.2b$_1$-c$_1$, would seem to show that in both cases the imposed boundary anomalies affect the convection pattern, by localizing the structures in preferred spots of the domain, in phase with the boundary inhomogeneities. However, temperature snapshots alone could be misleading, since the presence of hotter or colder zones does not necessarily indicate vertical motion of the fluid. Instead, looking at the vertical velocity panels, when $k_b = 0.5$ the boundary perturbations do effectively have an impact on w (Fig. 4.2c$_2$): the convective vertical motions exhibit the same (in

phase) large-scale pattern of boundary heterogeneities. On the contrary, forcing at a significantly larger scale with $\lambda_b = 8\pi$ ($k_b = 0.25$) does not have a significant impact on the scale of horizontal structures, which exhibit a clustering scale close to $\lambda_{so} = 2\pi$. In fact, in this case, w (Fig. 4.2b$_2$) is clearly distributed over the 8π domain similarly to the uniform case: notice how panel b$_2$ resembles the tessellation of four panels like a$_2$, where $k_b = 0$. This is confirmed also by the power spectrum $W(k)$ of the vertical velocity component, which exhibits a lower peak at $k = 0.25$ than at the self-organized scale $k = 1$ (see Fig. D.1e-f in Appendix D). This result is also supported by the heat fluxes (Fig. 4.2b$_3$-c$_3$) and by the mean Pearson cross-correlation coefficient between the temperature and the vertical velocity, which is $r(T, w) \simeq 0.04$ for $k_b = 0.25$, while it is $\simeq 0.35$ for $k_b = 0.5$. It emerges that when $k_b \ll k_{so}$, the boundary forcing is unable to impose its own scale and the system is organized according to the self-organized scale $k_{so} \simeq 1$ as in the homogeneous case.

The scenario does not change when considering a forcing wave number k_b greater than the self-organized wave number k_{so}. Also in this case, the scale of the b.c. is no longer perceived and the convection is not significantly affected by the boundary inhomogeneities. The structures aggregate randomly over the domain and exhibit only the typical self-organized scale $\lambda_{so} \simeq 2\pi$. Figure 4.2d$_{1-3}$ illustrates an example corresponding to the case $k_b = 3$, but the same behavior is found for any $k_b \geq 2$.

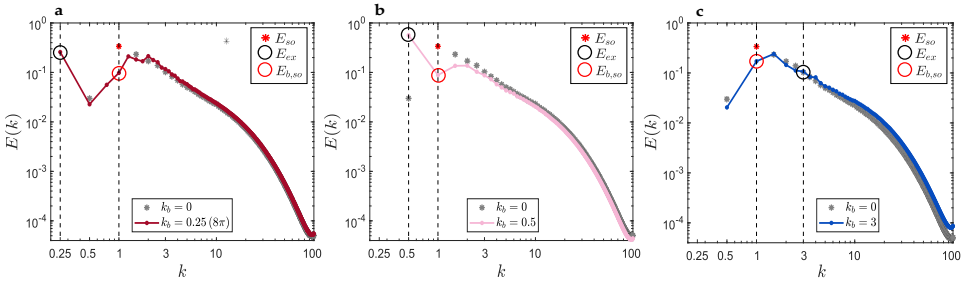

Figure 4.3: 3D simulations: horizontal power spectra (normalized to unit variance and averaged over the vertical fluid column and times $\tau_{conv} = 180 \div 220$) of the no-slip kinetic energy $E(k)$, plotted as functions of the horizontal wave number k for the cases $k_b = 0.25$ (**a**), $k_b = 0.5$ (**b**) and $k_b = 3$ (**c**). The spectrum for the homogeneous case ($k_b = 0$) is shown with gray asterisks for reference. The spectral peak E_{so} in the homogeneous case is marked with a red asterisk, while the spectral values (in the heterogeneous cases) corresponding to the exogenous scale (E_{ex}) and self-organized scale ($E_{b,so}$) are highlighted with a black and red circle, respectively.

All the previous snapshots provide a qualitative overview of the problem. In order to quantitatively identify when the boundary conditions are able

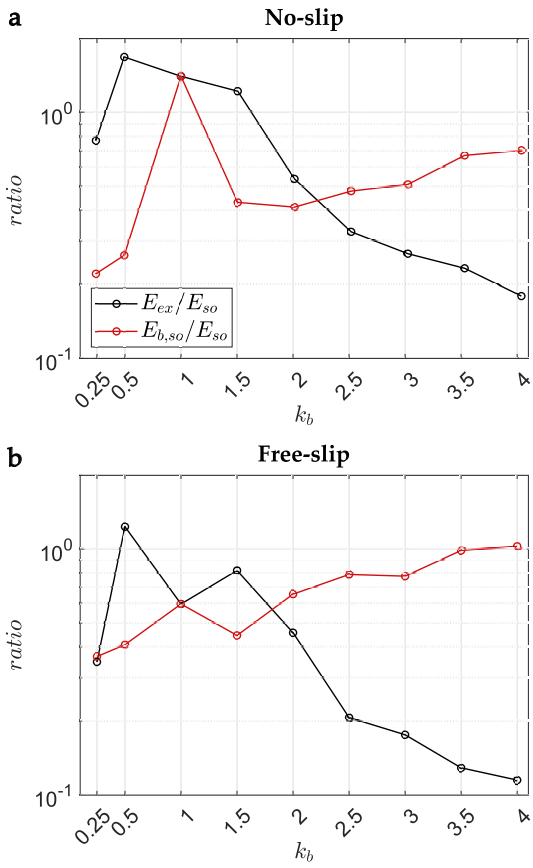

Figure 4.4: 3D simulations: E_{ex}/E_{so} (black line) and $E_{b,so}/E_{so}$ (red line), as functions of the b.c. wave numbers k_b, for the no-slip (**a**) and free-slip (**b**) cases.

to influence the convective process, the horizontal power spectrum $E_0(k)$ of the homogeneous case is compared with the spectra $E_b(k)$ for the cases $k_b = 0.25$, $k_b = 0.5$ and $k_b = 3$ in Fig. 4.3a–c; all the other cases are reported in Figs. D.2 and D.3 of Appendix D. In particular, we focus on (i) the maximum spectral density $E_{so} = E_0(k_{so})$ occurring in the homogeneous case at the scale of clustering $k_{so} = 1$, and (ii) the spectral density $E_{ex} = E_b(k_b)$, associated with the externally imposed scale k_b (the subscript ex recalls that this scale is exogenous). In Fig. 4.3a–c, the former is marked with a red asterisk and the latter with a black circle. An additional red circle indicates the value $E_{b,so} = E_b(k_{so})$ of the spectrum corresponding to the non-uniform cases at the self-organized wave number.

The interplay between the self-organized and the exogenous scales given

by the ratio E_{ex}/E_{so} is shown in Fig. 4.4 (black line). A ratio greater than 1 indicates that the thermal b.c. strongly influence the convection patterning, leading to a spectral peak at the forcing scale which is higher that the self-organized one in the homogeneous case. In this case, the external inhomogeneities reinforce the self-organized arrangement of the structures in the domain and the ascending (descending) plumes tend to organize themselves and to develop where the b.c. have positive (negative) values of temperature. Figure 4.4 shows that this occurs for $k_b = 0.5, 1, 1.5$ under no-slip conditions and for $k_b = 0.5$ in free-slip, all values that are close to the scale $k_{so} = 1$.

The extent by which the external forcing is capable of imposing its own scale on the flow can be seen considering the ratio between the spectral values at the self-organized scale for the non-homogeneous and homogeneous cases $E_{b,so}/E_{so}$ (compare the red and black lines in Fig. 4.4). When this ratio is below or equal to E_{ex}/E_{so} the boundary anomalies are imposing their scale on the flow, while when $E_{b,so}/E_{so}$ prevails, the exogenous scale becomes negligible with respect to the self-organized one, suggesting clustering as in the homogeneous case.

Figure 4.4 therefore shows that the non-uniform boundaries are able to induce convective structures of size comparable to the perturbation wavelength, and to localize them, only when the scale of the forcing is sufficiently close to the self-organized one. Otherwise, the clustering of structures occurs at the self-organized scale.

These findings are confirmed also by the integral length scale of the convection $\lambda_I = \int [E(k)/k]\,\mathrm{d}k / \int E(k)\,\mathrm{d}k$, which is a quantitative measure of the clustering scale based on the depth-averaged kinetic energy spectra [41, 233]. The mean $\overline{\lambda_I}$, averaged from $\tau_{conv} = 40$ (so that the initial transient phase is neglected) to $\tau_{conv} = 220$ (end of the simulations) for each thermal heterogeneity, is shown in Fig. 4.5. Both under no-slip and free-slip boundary conditions, we observe substantially higher $\overline{\lambda_I}$ for wave numbers k_b close to k_{so}, because of their capability to impose a new, larger, exogenous scale on the convection, overcoming the self-organized one; instead, the remaining cases exhibit a scale similar to that of the homogeneous case.

4.3.2 2D

In order to verify further the capability of non-uniform boundaries with k_b close to k_{so} to induce their own scale on the convection, we consider a two-dimensional systems characterized by an aspect ratio equal to 32π (Tab. 4.1). This choice allows us the exploration of k_b down to 0.0625, overcoming

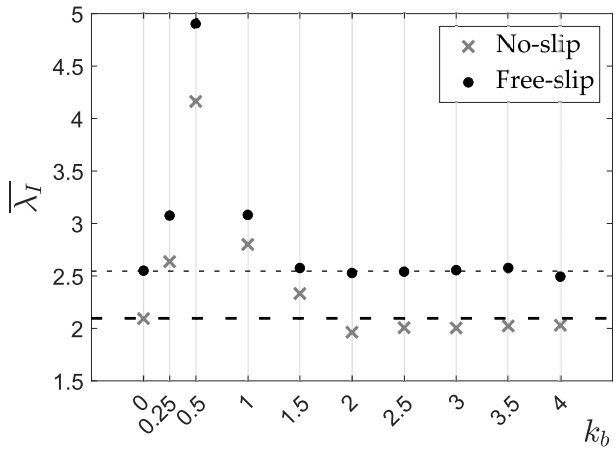

Figure 4.5: Time-averaged ($\tau_{conv} = 40 \div 220$) integral scale $\overline{\lambda_I}$ of the 3D simulations. The horizontal dashed lines refer to $\overline{\lambda_I}$ when $k_b = 0$, for the no-slip (thick line) and the free-slip (thin line) cases.

the limit of small 3D domain dimensions. Moreover, we extend the analysis to wave numbers $k_b = 5$ and 6, in order to confirm that high-frequency b.c. have no evident effect on the convection.

In terms of 2D patterning, we find a behavior similar to that observed in the 3D case. In fact, three elements emerge. Firstly, the self-organized scale occurs both under uniform and non-uniform boundaries. Secondly, non-homogeneous boundary temperatures, having intermediate values of k_b, are able to force the formation of structures around such heterogeneities, exhibiting scales at the b.c. wavelength. Finally, the impact of external thermal perturbations weakens with growing boundary wave number, resulting in a behavior of the system dominated by the self-organized scales, also observed in the homogeneous case $k_b = 0$. Representative vertical sections of the temperature, velocity and flux fields proving these findings are reported in Fig. D.5, Appendix D.

Figures 4.6a–b show two of the most representative spectra $E(k)$ obtained for the two-dimensional simulations, where the exogenous peak E_{ex} largely overcomes the self-organized one. All the other spectra are shown in Fig. D.6 and D.7 of Appendix D. Having confirmed the existence of the self-organized structures also in 2D, the interaction between the self-organized and the exogenous scales is highlighted by the metric E_{ex}/E_{so}, shown in Fig. 4.6c–d. A ratio $E_{ex}/E_{so} > 1$ – for which the b.c. affect the convection patterning – here occurs for k_b between 2 and 4 under no-slip conditions

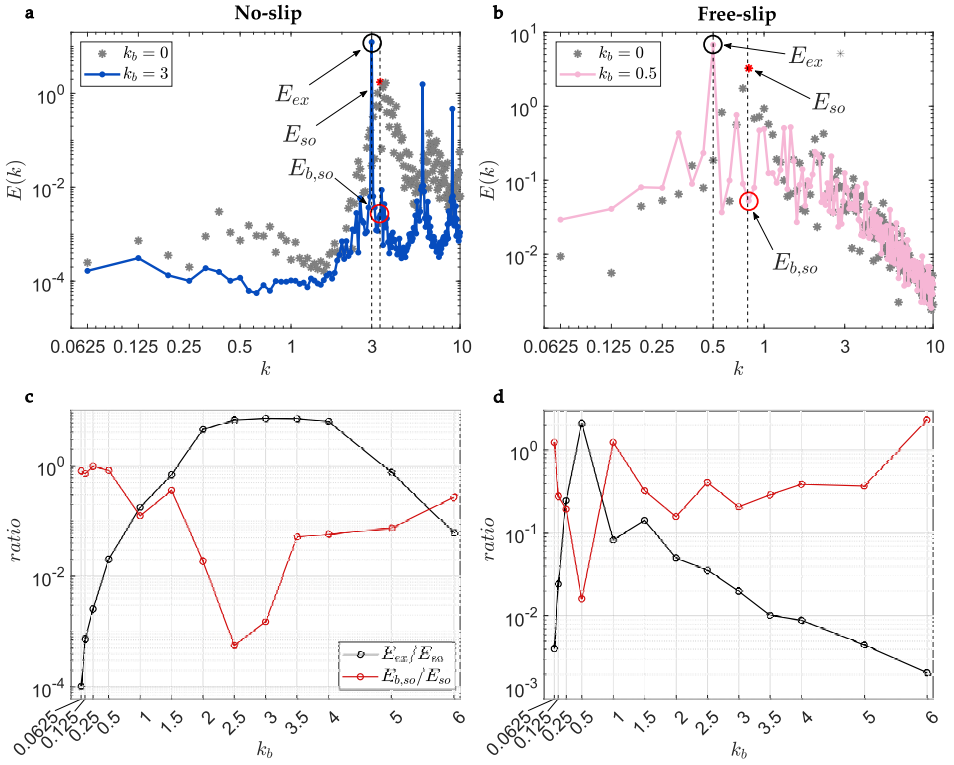

Figure 4.6: Low-k part of the kinetic energy spectra (averaged over the vertical fluid column and times $\tau_{conv} = 180 \div 220$) of the 2D no-slip case $k_b = 3$ (panel **a**) and 2D free-slip $k_b = 0.5$ (panel **b**). The spectrum for the homogeneous case $k_b = 0$ is shown with gray asterisks for reference. The values E_{so}, E_{ex} and $E_{b,so}$ are marked with a red asterisk, a black and a red circle, respectively. Panels **c** and **d** show the two ratios E_{ex}/E_{so} (black line) and $E_{b,so}/E_{so}$ (red line) as a function of the b.c. wave numbers k_b, for all the no-slip (**c**) and free-slip (**d**) cases.

and for $k_b = 0.5$ in free-slip. Such pattern-inducing values of k_b are around the self-organized scales $k_{so} \simeq 3$ (no-slip, red asterisk in Fig. 4.6a) and $\simeq 0.8$ (free-slip, Fig. 4.6b). Otherwise, the clustering occurs at the self-organized scale, as highlighted by a greater ratio $E_{b,so}/E_{so}$ than E_{ex}/E_{so} (Fig. 4.6c–d).

The 2D cases confirm that – as already observed in 3D – values of the imposed wave number k_b significantly greater or smaller than k_{so}, produces no relevant impact on the convection: the only observed scale remains the self-organized one. The exogenous scale prevails over the self-organized one only when the non-homogeneous boundaries are characterized by a wave number k_b close to k_{so}.

The spectra allow us to capture another aspect: under no-slip conditions the peak E_{so} occurs around the horizontal wave number $k = 3$ (red asterisk in Fig. 4.6a), while in free-slip conditions the self-organized peak occurs at $k \simeq 0.8$ (Fig. 4.6b). This is in line with the results discussed in [240] and [241] which analyzed the relationship between roll number, Rayleigh and Prandtl number for stable 2D RB solutions, showing that in large aspect ratio domains multiple stable states are possible. This also suggests that, at least in 2D RB convection, a narrow range of possible stable k_{so} values is possible and we expect that it is in this range that the k_b imposed by the boundary conditions will have a greater impact on the flow. Further future exploration of a broader range of σ and R values could be useful to explore this point.

4.3.3 Effects on the Nusselt number

Another relevant issue concerns the effects produced by the thermal heterogeneities on the Nusselt number Nu. Figure 4.7 shows the time-averaged $\overline{Nu}$ as a function of the imposed k_b: both in 3D and in 2D (Fig. 4.7a and b, respectively) the convection is stronger in free-slip than in no-slip conditions. However, the flow topology seems not consistently affected by the temperature boundary anomalies, since their $\overline{Nu}$ is very close to that found under homogeneous conditions ($k_b = 0$). The only exception emerges for the 2D free-slip forcing at $k_b = 0.25$ and 0.5, for which $\overline{Nu}$ is slightly lower than its mean value. This is consistent with the spectral peak at a lower wave number $k = 0.5$ in the $k_b = 0.5$ case (see Fig. 4.6b and Fig. D.2 in Appendix D for comparison) and the link between larger aspect ratio of large-scale rolls and lower Nusselt number discussed in [240].

4.4 Conclusions

We have found that thermal boundary inhomogeneities applied in-phase on both plates of a Rayleigh-Bénard configuration, can play a crucial role. Our work demonstrates that self-organized structures, or thermal superstructures [234] (up to now observed under uniform conditions only), are not inhibited by the presence of exogenous heterogeneities on the boundaries. Our main result is that the introduction of non-homogeneous boundaries produces another convective scale in the system, which determines the position and the size of thermal structures, only when the scale of the perturbation is close to the scale of the self-organized clustering. If they

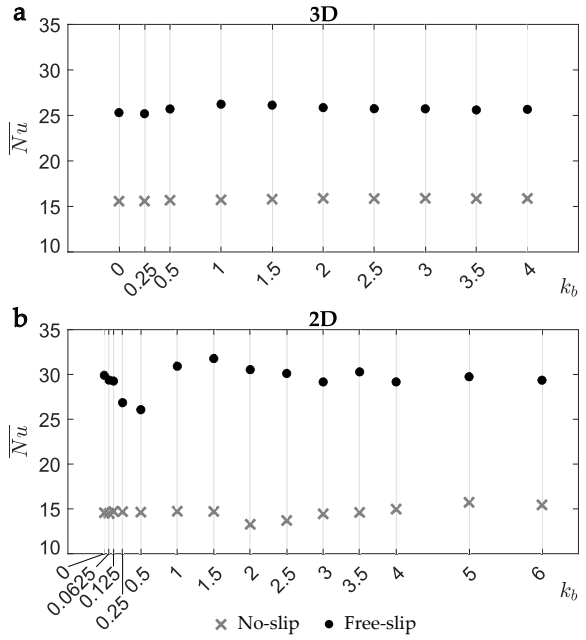

Figure 4.7: Time-averaged ($\tau_{conv} = 40 \div 220$) Nusselt number $\overline{Nu}$ of each analyzed case, for the 3D (**a**) and 2D (**b**) simulations. The no-slip cases are marked by gray crosses, while the free-slip cases by black dots.

are not comparable, the effects produced by the boundaries on the convection are negligible, resulting in a behavior similar to that obtained under homogeneous conditions. The setup considered in this work, introducing a horizontal temperature modulation on the boundaries, is also connected to the so-called problem of horizontal convection [242], where a horizontal temperature gradient drives convection. This may justify the appearance of horizontal winds at the scale of the boundary perturbation, as reported above for the 3D case $k_b = 0.25$, but this topic deserves further future investigation.

5

Alternate convection arising in a 2D Rayleigh-Bénard system

A scientific article about the results presented in this Chapter is in preparation.

5.1 Introduction

Rayleigh-Bénard convection, hereinafter RB, has been the subject of numerous theoretical, experimental and numerical studies [213–217, 241]. Its feasible tractability has allowed many researchers to adopt various RB systems for the investigation of many geophysical phenomena and engineering applications. The classical RB configuration involves two horizontal plates, where the bottom is hotter than the top one and their temperatures are uniform. However, the idealization of constant temperatures at the upper and lower layers is far from the reality: in real physical systems thermal boundary conditions are often inhomogeneous, resulting in temporal and spatial variation in the efficiency of heat transfer [229].

As an example, the analyses carried out in Chapter 4 have shown that thermal heterogeneities at the boundaries yield to the occurrence of another scale in the system, clearly induced by the boundary anomalies themselves. In addition to the self-organized scale emerging under homogeneous conditions, non-uniform boundaries may drive the convection patterning and clustering of plumes of the same sign depending on the wavelength of the imposed perturbation [211].

That work (Chapter 4) introduced a horizontal temperature modulation on the boundaries, a problem closely related to the so-called horizontal convection, after Stern (1975) [243]. Whereas RB convection focuses on the vertical heat flux between two plates at different temperatures, horizontal convection (HC) is the canonical case for heat flow through a single (top or

bottom) boundary [244], in which the convection is driven by differential heating along the same horizontal level and overturning circulation in the volume occurs [242]. Among its relevance in other geophysical systems or planetary atmospheres [245, 246], the topic is commonly associated with the mechanisms of the large-scale ocean circulation and differences in salinity [243, 247].

The preliminary investigation carried out in this Chapter focuses on a particular case of horizontal convection: instead of considering temperature gradients in a single top or bottom boundary as in standard HC, here different horizontal temperatures are imposed on both plates of the system. To this aim, we consider sinusoidal patterns imposed both at the lower and upper plate of a two-dimensional RB configuration; differently from what observed in the previous Chapter 4, the non-homogeneous boundaries are not in phase and the average temperature of the two periodic, rigid plates is set to zero. This novel configuration is composed of two features: (i) the horizontal gradients are out of phase and (ii) a global null temperature difference characterizes the fluid layer in the vertical direction. In doing so, albeit the two plates are on average at null temperatures, the system exhibits zones where the bottom plate is hotter than the top one and vice-versa, due to a phase shift of the sinusoids. As a result, the configuration is nothing but an alternation of a classical RB configuration and a stable zone, namely where the stratification of the fluid is neutral (cold at the bottom and hot at the top). For this reason, we call the phenomenon *alternate convection*, including the vertical motions emerging from the classic RB convection and the circulations prompted by the horizontal gradients typical of HC.

The primary motivation for studying such a particular case is found in the *Part I* of this thesis. In the atmospheric boundary layer we have observed the effects produced by the cities, which are thermal heterogeneities with respect to any natural land nearby. The peculiar thermal properties characterizing the impervious surface of an urbanized area, together with its geometry and physical features, yield a convection which is different from the one developing over a natural, pervious surface. The well-known phenomenon of Urban Heat Island effect (UHI, [27]) – namely, the warmer temperatures experienced by a city than its rural surroundings – has been largely studied in terms of the causes that originate it, the metrics for its quantification, its spatial distribution with respect to the size of the urban agglomeration, its exposition and meteorological conditions and in terms of the ways to mitigate it [36]. However, what are the interactions among contiguous UHIs on the atmosphere? How much is the different heating of

adjacent surfaces reflected in horizontal or vertical motions? These topics are still poorly understood and certainly not trivial to solve, because it is quite difficult to generalize such complicated dynamics.

With this preliminary study we try to take a first step toward in direction, to understand the interaction of contiguous convective and stable zones through a simple two-dimensional model. Despite the impossibility to represent a real case in 2D, this study allows to feature the basic mechanisms that govern the interplay among zones characterized by different thermal conditions. Not only do the horizontal gradients induce a convection in the system, but their mutual proximity or distance lead to different spatial structures and interactions.

5.2 Model configuration

The classical model of Rayleigh-Bénard convection (see Eqs. 4.1–4.3 in Chapter 4) is here studied in a two-dimensional domain of aspect ratio $L = 4\pi$, with periodic boundary conditions (b.c.) in the horizontal direction x and thickness of the fluid layer d equal to the unity (the vertical coordinate z goes from 0 to 1). The two parameters controlling the system, namely the Rayleigh number R and the Prandtl number σ, are set to $R = g\alpha\Delta T d^3/(\nu\kappa) = 10^7$ and $\sigma = \nu/\kappa = 0.71$ (air) respectively, where g is the acceleration of gravity, α the thermal expansion coefficient, ν the kinematic viscosity and κ the thermal diffusivity. The average temperature difference between the two horizontal plates (ΔT) is set to zero: thus, the problem which we analyze is slightly different from a standard RB configuration characterized by a hot bottom layer and a cold top one. We impose sinusoidal thermal boundary conditions, namely $T_b = A\,\sin(k_b \cdot x)$ at the bottom plate and $T_b = A\,\sin(k_b \cdot x + \pi)$ at the top one, with amplitude $A = 0.5$ (peak-to-peak amplitude $2A = 1$) and wave number k_b (the subscript b is referred to boundaries). Note that the top b.c. is shifted of π with respect to the bottom one, so that the two sinusoidal patterns are in counter-phase.

As regards the velocity boundary conditions, we test both the no-slip and free-slip cases. Table 5.1 shows the wave numbers k_b and wavelengths $\lambda_b = 2\pi/k_b$ characterizing each run explored. E.g., for each simulation the same velocity condition and wave number (wavelength) is adopted for the two plates; what triggers the instability is the thermal anomalies since they are in counter-phase, as shown in the schematic representation of Fig. 5.1.

The numerical simulations employ the same numerical code of Chapter

Table 5.1: Wave numbers k_b and wavelengths λ_b of the sinusoidal temperature boundary conditions imposed at the top and bottom boundaries of the 2D domain, $L = 4\pi$.

k_b	0.5	1	1.5	2	4	8	16	20	24	32
λ_b	4π	2π	$4\pi/3$	π	$2\pi/4$	$2\pi/8$	$2\pi/16$	$2\pi/20$	$2\pi/24$	$2\pi/32$

4 [238], with 193 non uniform grid points along the vertical coordinate z and 512 along the horizontal x.

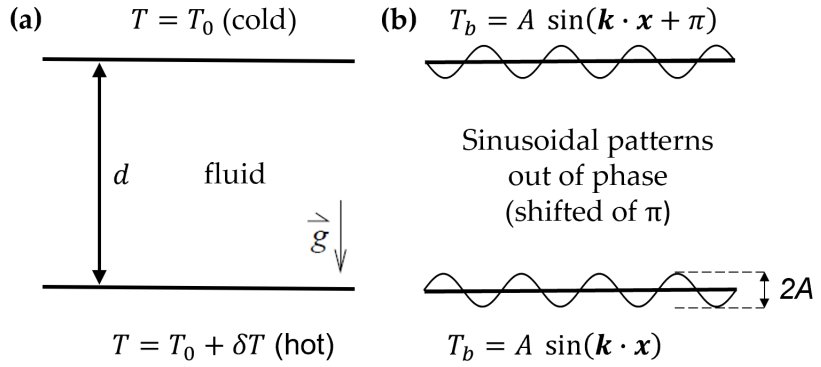

Figure 5.1: Schematic representation of the Rayleigh-Bénard configuration, with (**a**) uniform boundary conditions and (**b**) thermal b.c. (sinusoidal patterns out of phase).

5.3 Results

We start considering the cases characterized by no-slip conditions.

Figure 5.2 shows snapshots of the temperature field at different times during the evolution of the simulation with $k_b = 0.5$, which lasts about τ_{conv}=440 convective times. We refer to $\tau_{conv} = \sqrt{d/g\alpha\Delta T}$ as the time a plume takes to vertically cross the fluid layer d. Notice that along the whole duration of the run the temperature does not change qualitatively, i.e., a stationary state is reached. However, the most remarkable feature is that the imposition of the counter-phase thermal anomalies on both plates yields to two distinct patterns of temperature. On the one hand, considering the left-hand half of the domain (from 0 to 2π), we observe the well-known thermal plumes developing in RB convection, characterized by three rolls (three ascending hot plumes and three descending cold ones). This is noticeable since one may have expected only conductive heat transfer

when a null temperature difference on average between the two plates occurs. Still, it is clear that the imposition of counter-phase sinusoidal perturbations at the boundaries yields a non-null temperature difference ΔT locally, which in turn results in an alteration of the local effective Rayleigh number R. In other words, even if $\Delta T = 0$ globally, the juxtaposition of such perturbations at the boundaries is able to prompt convection in the system.

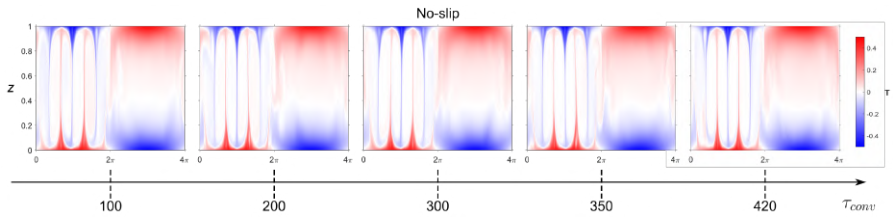

Figure 5.2: Snapshots of the temperature perturbations T for the no-slip case with $k_b = 0.5$, taken at subsequent times $\tau_{conv} = 100$, 200, 300, 350 and 420 (black arrow at the bottom).

On the other hand, the portion of the domain ranging from 2π to 4π reveals a completely different zone without plumes. As time passes, they remain distinct and well separated one from another. We call the phenomenon *alternate convection*, which is composed of the aforementioned two portions, namely a *convective zone* (CZ) and a *stable zone* (SZ), respectively. They correspond exactly to the drastic change in the boundary conditions due to the counter-phase anomalies (see Fig. 5.3).

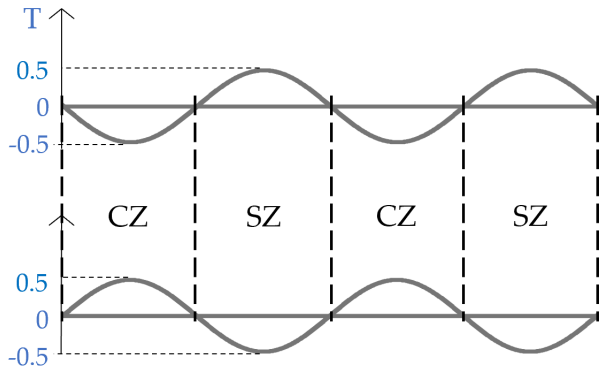

Figure 5.3: Schematic representation of *alternate convection*, where Convective Zones (CZ) alternate with Stable Zones (SZ). The y-axes with labels in light blue indicate the temperature characterizing the top and bottom plates.

As said, the convective zone resembles a classical RB system, where the bottom surface is hotter than the top one and convection is enhanced

because from 0 to 2π (in the current case $k_b = 0.5$) the temperature difference between the plates is not null. Close to the CZ, we find the opposite scenario with a colder bottom plate than the top one: the denser fluid is already at the bottom and, therefore, here the equilibrium is stable (SZ).

This is clear also looking at the snapshots of the horizontal and vertical velocities u and v, taken at the end of the simulation (Fig. 5.4a,b). We observe horizontal motions occurring in the CZ, which reflect the pattern underwent by the temperature field in Fig. 5.2; the highest u is found at the rolls interface (Fig. 5.4(a)). Both u and v are distributed along the CZ, while the stable zone exhibits null velocities.

These findings are confirmed also by the total kinetic energy $E = u^2 + v^2$: it is null in the stable zone and in the middle of the domain ($z = 0.5$), while its maxima occur near the boundaries of the convective zone (Fig. 5.4(c)). Another way of highlighting the spatial distribution of the two zones is given by the integral of E along the vertical, shown in Fig. 5.4(d), where the null kinetic energy is distributed along the SZ, which occupies the portion of the domain from 2π to 4π.

Figure 5.4(e) shows the spatial pattern of vertical heat fluxes, computed as the product between the vertical velocity field and the temperature anomalies $f = vT'$: it is a measure of the heat transport that occurs in the system. Red and black zones indicate high values of f and they are concentrated along the plumes, in particular following the distribution of the rolls. Otherwise, the flux is clearly reduced and tends to zero in the stable zone, where indeed no convective motion occurs.

Let us now focus on what happens at higher wave numbers. Figure 5.5 shows the spatial trend of the kinetic energy E, integrated along the vertical z. Ranging from the lowest wave number $k_b = 0.5$ to $k_b = 2$ the pattern of $\int_z E$ reflects the distribution of temperatures along the domain and the presence of the two zones, namely the convective and the stable one.

This is clear by comparing the temperature snapshots (shown in the insets of Fig. 5.5) with the integral of the kinetic energy associated to each panel (representing each case). From $k_b = 0.5$ to $k_b = 2$, the system exhibits at least one stable zone where nor vertical nor horizontal convective motions occur: here, the integral of the kinetic energy ($\int_z E$) drops drastically to near-null values and no plume occurs in the temperature field. Conversely, values of $\int_z E$ greater than zero are associated with vertical and horizontal velocities which lead to the formation of distinct plumes. The rolls are prompted by the occurrence of the pure horizontal convection: in fact, each plate is subjected to a horizontal difference in temperature given by the

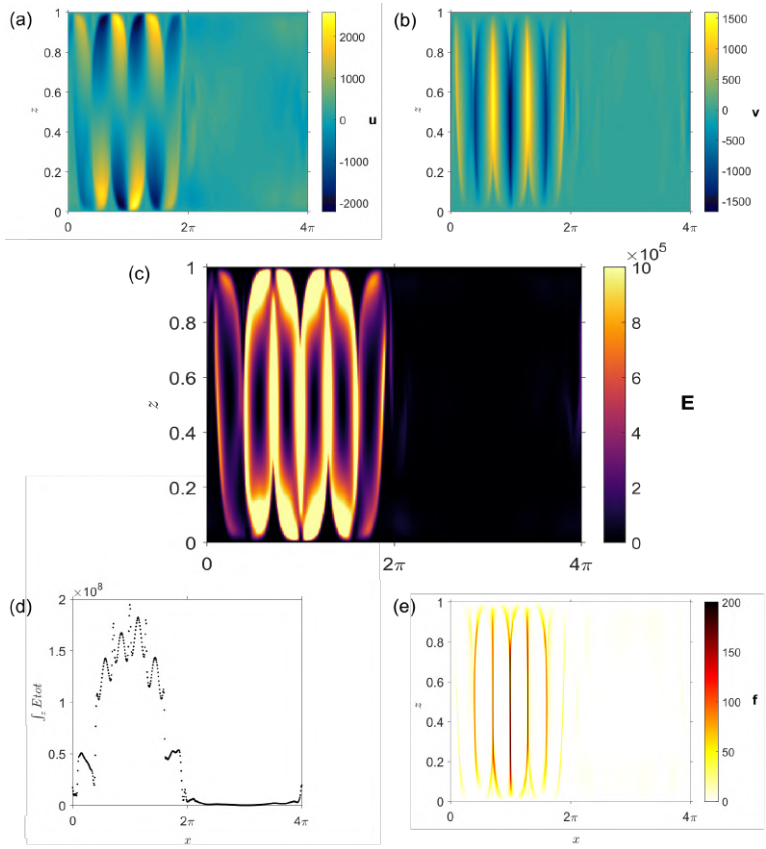

Figure 5.4: Snapshots at the end of the simulation ($\tau_{conv} = 420$) of the horizontal velocity u (a), vertical velocity v (b), kinetic energy $E = u^2 + v^2$ (c), integral of E along the vertical coordinate (d) and the vertical heat flux $f = vT'$ (e), for the no-slip case with $k_b = 0.5$.

thermal perturbations imposed by the sinusoidal patterns at the boundaries. In our analysis, we observe that up to $k_b = 2$ these motions in the convective zone alternate with the stable zone, where instead either the horizontal nor the pure convection develop. Actually, in the no-slip cases $k_b = 0.5$, 1, 1.5 and 2 the kinetic energy drops down to almost null values (stable zones) where the sinusoidal patterns exhibit a cold zone at the bottom and a hot one at the top (stable stratification of the fluid).

By increasing further the wave number, the situation start changing. In the analyses carried out here, we observe a substantial reduction of the kinetic energy going from the case at $k_b = 2$ to $k_b = 4$, subsequently from $k_b = 4$ to $k_b = 8$, and so on. With the preliminary tests shown in this

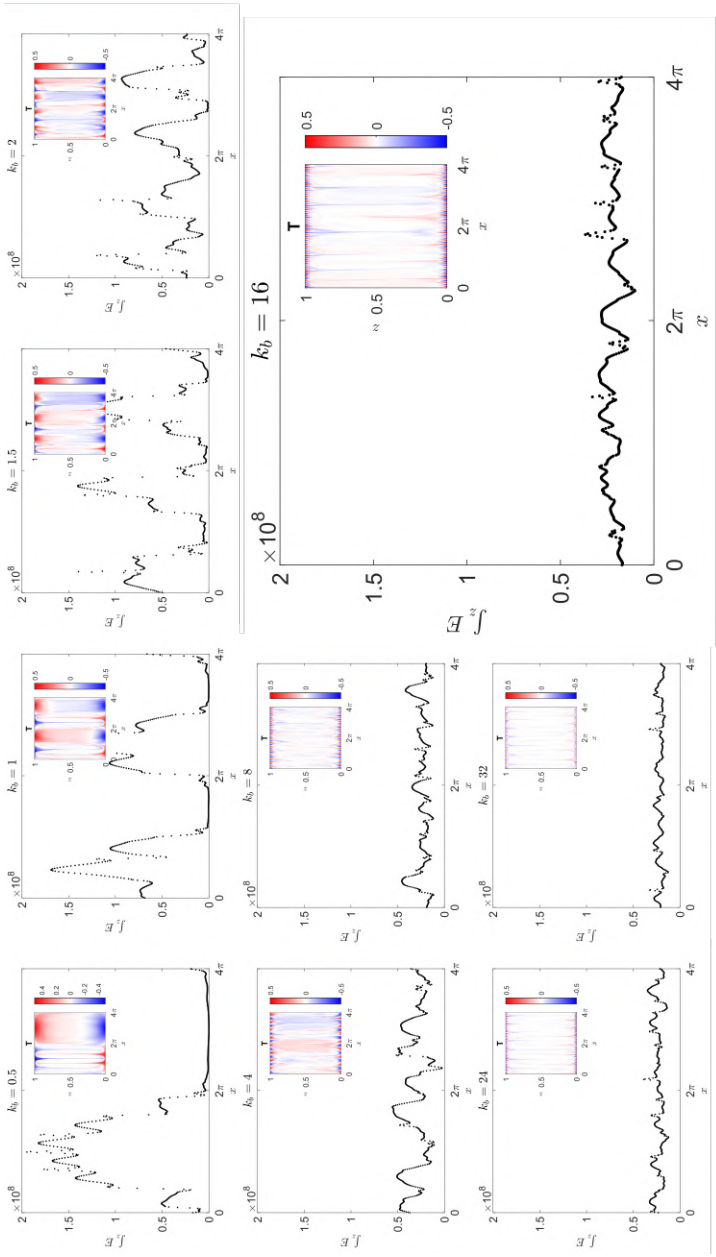

Figure 5.5: No-slip simulations. Integral of the kinetic energy $E = u^2 + v^2$ along the vertical coordinate z taken at $\tau_{conv} = 420$ for the cases: $k_b = 0.5$, 1, 1.5, 2, 4, 8, 16, 24 and 32. The insets show the snapshot of the temperature field at the same instant ($\tau_{conv} = 420$).

Chapter, it is hard to clearly identify the one wave number that turns down the energy of the system, i.e., the motions occurring in the convective zone. Still, the reduction of energy is strictly coupled with growing wave numbers, as featured by the fields of temperature T, vertical velocity v and heat flux $f = vT'$ (where T' are the temperature anomalies) taken at the end of the simulations for the cases $k_b = 16$ and $k_b = 32$, shown in Fig. 5.6. The temperature panels clearly highlight the presence of high frequency temperature anomalies at the boundaries, which are shown with alternating red and blue colors. However, both for the intermediate case $k_b = 16$ and the highest wave number evaluated ($k_b = 32$) we observe that the hot and cold plumes do not develop in phase with the sinusoidal b.c. The sinusoidal peaks are too close to each other to allow the system to follow their patterns and, therefore, the thermals aggregate in few clusters. Thus, the impact of the boundaries in the system is highly reduced. The rising hot plumes and the descending cold ones still give rise to a weak convection, as shown by the vertical velocities in the central panels of Fig. 5.6 and the heat fluxes (right-hand side of Fig. 5.6). If compared with the case $k_b = 0.5$ (see Fig. 5.4), we notice a substantial reduction in the values of v and f; this means that the convective zones are less energetic when the high wave numbers characterizing the boundaries are not able to influence the way the plumes develop. However, this is not the only reason. In fact – as shown by Bassani et al. (2022) [211] – in a standard RB model characterized by a temperature difference between the two plates, boundaries similar to those applied in this study, do affect the scales of the convection but not its intensity. As a consequence, here, the reduction of convection is strongly affected by the fact that the two plates have no temperature difference and the only perturbations are imposed in the horizontal scale. When the frequency of these perturbations increases, the anomalies begin to be perceived as a local small noise, which triggers a reduced instability in the system with respect to what happens at lower wave numbers.

We now focus on the free-slip boundary conditions, starting from the lowest wave number analyzed ($k_b = 0.5$), as above. The evolution of the temperature field at different τ_{conv}, displayed in Fig. 5.7, features the existence of two distinct zones characterized by different patterns: the convective zone (CZ) from 0 to 2π and the stable zone (SZ) from 2π to 4π. Differently from the no-slip case, in which the system exhibited a quite ordinate separation between the two zones and three distinct rolls in the convective zone, here the free-slip boundaries induce one single roll in the CZ and a more chaotic transition from one zone to another.

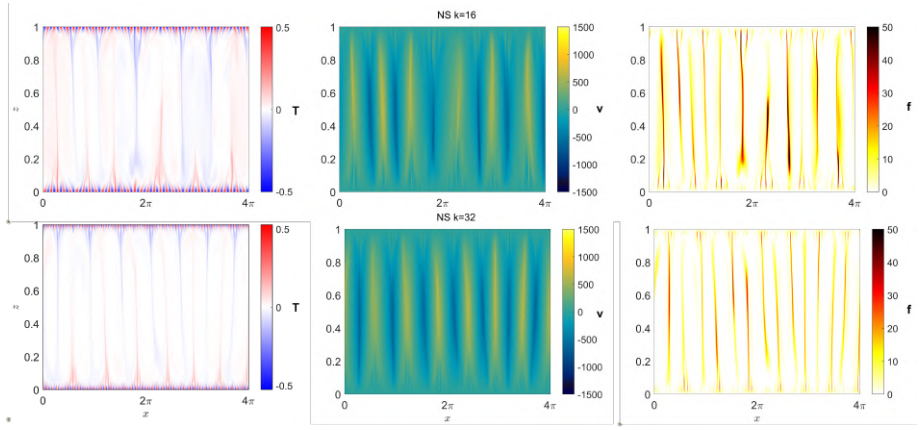

Figure 5.6: Snapshots of temperature T, vertical velocity v and heat flux f at $\tau_{conv} = 420$ for the no-slip cases $k_b = 16$ (top row) and $k_b = 32$ (bottom row).

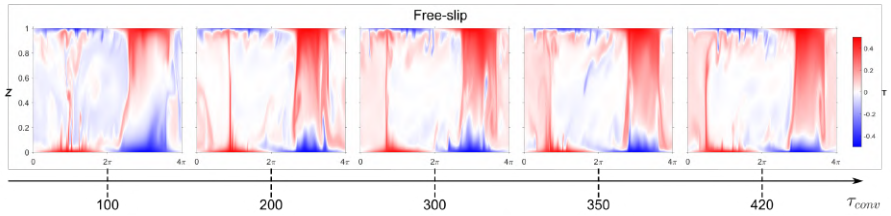

Figure 5.7: Snapshots of the temperature perturbations T for the free-slip case with $k_b = 0.5$, taken at subsequent times $\tau_{conv} = 100$, 200, 300, 350 and 420.

This is because free-slip b.c. are known to favour the formation of high winds [248] – due to the absence of shear stresses at the boundaries – as shown in the snapshot of the velocity fields in Fig. 5.8a,b taken at the end of the simulation (τ_{conv}=440). Notice that the horizontal velocity field (u) is characterized by high values near the boundaries, while it is null in the stable zone (SZ); in addition the SZ occupies a reduced portion of the right-hand side of the domain than under no-slip conditions. The explanation for this occurrence is again found in the higher horizontal winds emerging in free-slip than in no-slip: they induce a drag action on the stable zone nearby. The vertical velocity v and the kinetic energy E complete this picture, confirming the existence of a stable zone in which no motions occur (Fig. 5.8b,c), while a convective zone greater than the half of the domain clearly emerges. The integral of the kinetic energy along the vertical (Fig. 5.8d) highlights both the intensity and the spatial distribution of the convective zone across the domain, while the snapshot of the heat flux f

(Fig. 5.8e) reflects the behavior of the vertical convection. This occurs along the plume (in the convective zone, at the left-hand side of the domain) and at the edges of the stable zone, which is confined by positive fluxes.

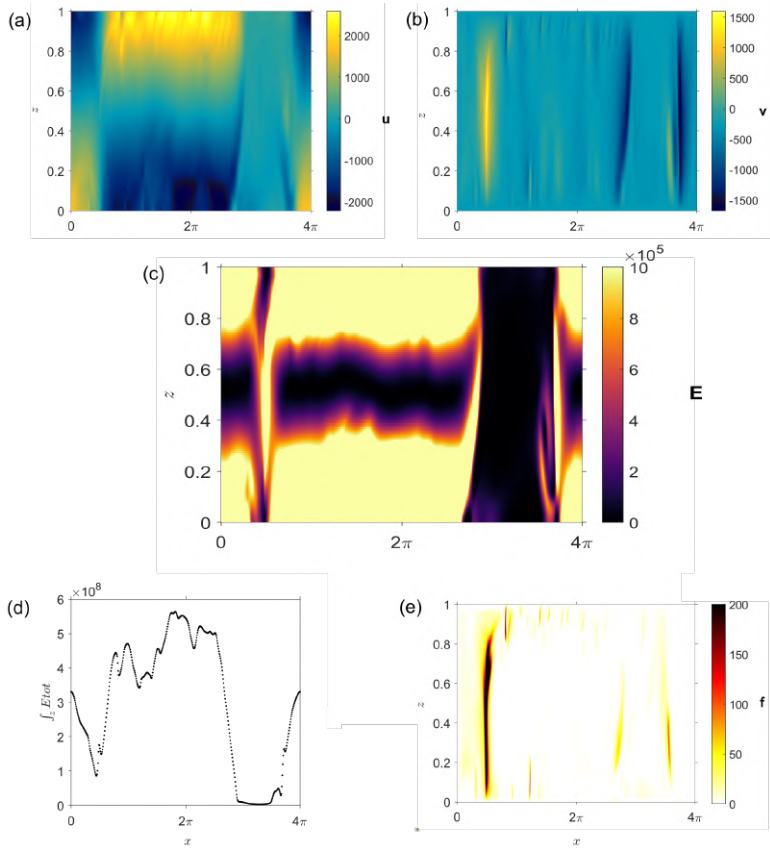

Figure 5.8: Snapshots at the end of the simulation ($\tau_{conv} = 420$) of the horizontal velocity u (a), vertical velocity v (b), kinetic energy $E = u^2 + v^2$ (c), integral of E along the vertical coordinate (d) and the vertical heat flux $f = vT'$ (e), for the free-slip case with $k_b = 0.5$.

With increasing wave number of the perturbation imposed at the boundaries, the system gradually reduces its energy (Fig. 5.9), as observed under no-slip b.c. Two main differences with respect to the no-slip case are found: (i) the integral of the kinetic energy along the vertical ($\int_z E(x,z)\,dz$) is characterized by higher values in free-slip, and (ii) the stable zones do not alternate with the convective ones as regularly as in the no-slip case. Both differences are ascribable to the strong horizontal velocities that influence all the free-slip cases (not shown). In fact, with higher winds, (i) the term u

weights more in the kinetic energy, enhancing its values, and (ii) the stable zone is less able to be maintained and is subjected to the drag action of the CZ nearby. This is why we do not observe regular stable zones alternating with the convective ones under free-slip conditions. Conversely, an almost regular succession of CZ and SZ is observed under no-slip conditions. Beside the strong winds which affect the free-slip cases, the phenomenon of *alternate convection* still occurs. Moving from $k_b = 0.5$ to $k_b = 1.5$, we observe one stable zone that coexists with the convective one; at $k_b = 2$, two CZs are found (see Fig. 5.9). When the wave number at the boundaries is further increased, e.g., considering $k_b = 4$, 8 or 16, the system is no more capable to distinguish separate zones and the convection is drastically reduced due to the high frequency of the boundary perturbations.

As seen, this is true both under no- and free-slip velocity conditions. In fact, by integrating the kinetic energy along the whole fluid column and the horizontal direction ($\int_z \int_x E(x,z)\,dxdz$) it emerges that the more the wave number is increased (wavelength decreased), the less the system is convective (see Fig. 5.10) and less horizontal and vertical convection occur with respect to the cases where the wavelength of the boundary anomalies is higher. The influence of horizontal motions in free-slip is reflected in the higher values reached by the integral of E with respect to the no-slip cases.

Another way to quantify heat transport in RB convection is given by the dimensionless volume-averaged Nusselt number, which is computed – as in the classical RB scheme – as $Nu = 1 + \langle v\,T' \rangle$, where v is the vertical velocity field along z and T' represents the temperature anomaly; Nu is equal to unity when only conduction and no convective transport occurs (in the classical definition with thermal gradient) and grows as fluid motion sets in [219]. In this preliminary analysis, we have maintained the same definition of the standard RB problem. Future work may define a modified Nusselt number in a way that takes into account the occurrence of horizontal motions together with the vertical ones.

Figure 5.11 shows the evolution of Nu as a function of the convective time τ_{conv} for all the explored cases. After an initial transient in which instability is triggered and Nu reaches its maxima values, we observe a sustained convection in all cases, either under free-slip and no-slip b.c. Actually, the Nusselt number hardly overcomes 5 (on average and neglecting the initial transient): such value is clearly reduced with respect to a standard RB configuration ($\Delta T \neq 0$ and homogeneous boundaries), where – depending on the aspect ratios considered [240] – it can reach medium values of 30 under free-slip and 15 under no-slip conditions [211]. The fact that the

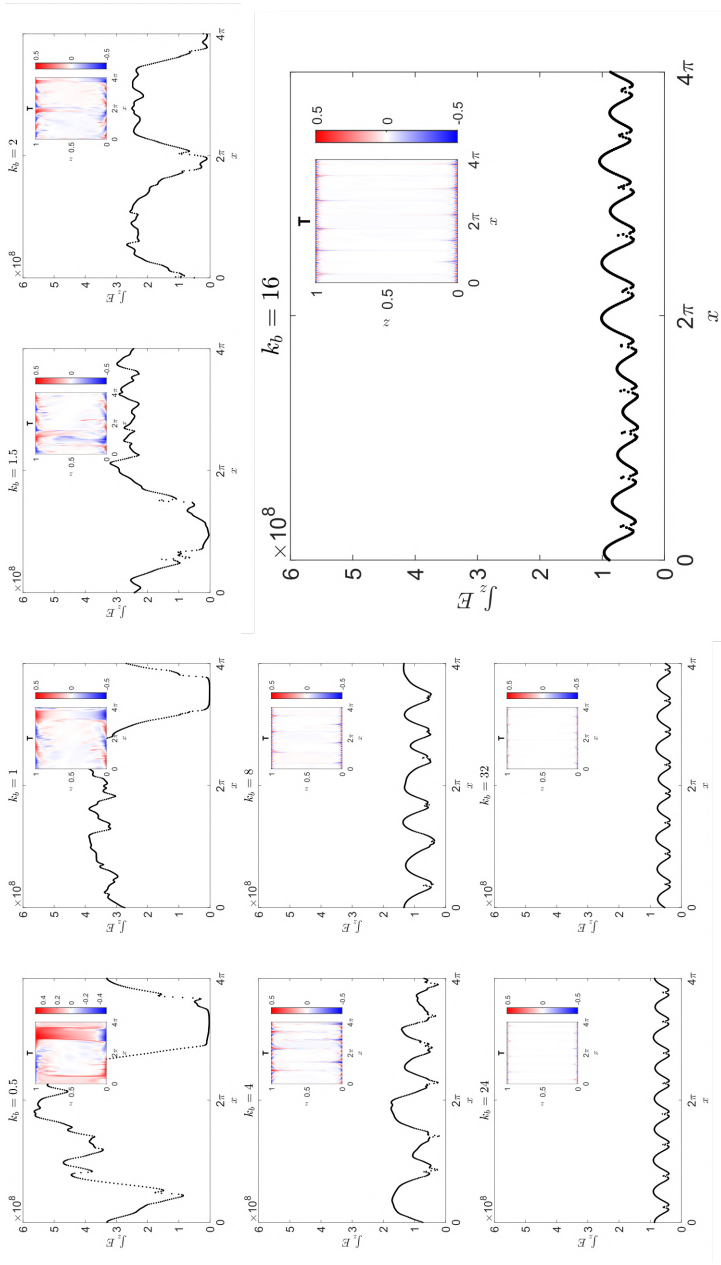

Figure 5.9: Free-slip simulations. Integral of the kinetic energy $E = u^2 + v^2$ along the vertical coordinate z taken at $\tau_{conv} = 420$ for the cases: $k_b = 0.5$, 1, 1.5, 2, 4, 8, 16, 24 and 32. The insets show the snapshot of the temperature field at the same instant ($\tau_{conv} = 420$).

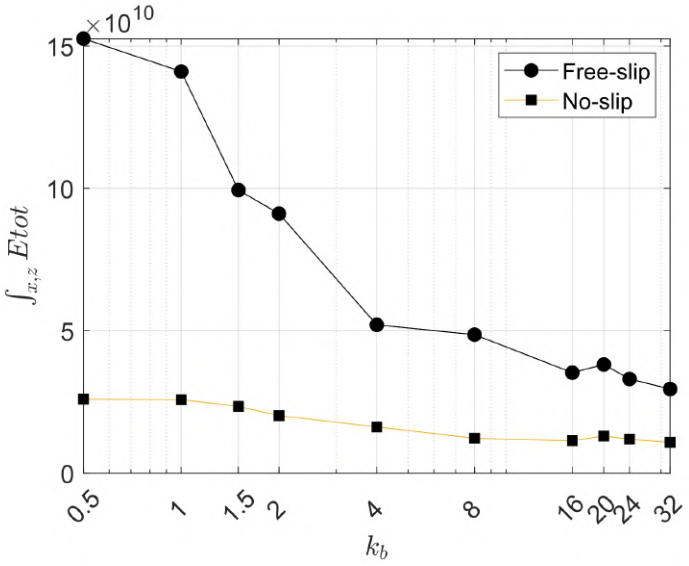

Figure 5.10: Integral along the vertical z and the horizontal x coordinates of the kinetic energy ($\int_{x,z} E$), plotted as function of the imposed wave number k_b.

convection is always sustained proves also that the zonal flows observed in two-dimensional free-slip configurations by Goluskin et al. (2014) – a phenomenon also referred as bursting convection [248] – do not occur under the conditions imposed here.

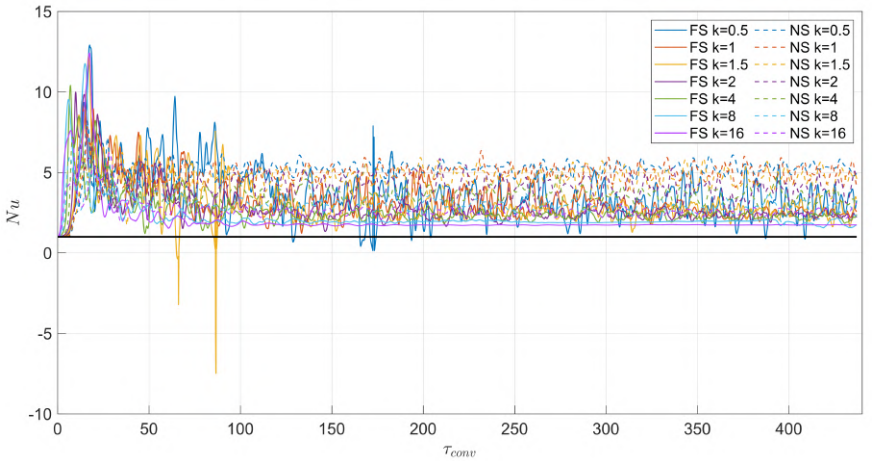

Figure 5.11: Time series of the Nusselt number Nu for all configuration explored. The solid black line indicates the unity.

The time series of Nu (Fig. 5.11) highlight that a statistically stable condition with limited oscillations is reached in all cases, especially after about half time of the total run: i.e., the motion that has been established is maintained along the whole duration of the simulations.

Figure 5.12 shows the behavior of the medium Nusselt number $\overline{Nu}$, averaged between $\tau_{conv} = 300$ and the final time (420), and the corresponding coefficient of variation CV as functions of the wave number k_b imposed at the boundaries. Differently from many studies about free-slip and no-slip b.c., e.g., [122, 211, 249], Fig. 5.12(a) reveals that $\overline{Nu}$ is slightly higher under no-slip rather than free-slip boundaries. Albeit the most energetic system (considering both horizontal and vertical velocities) is found to be the one under free-slip conditions (Fig. 5.10), we should notice that the Nusselt number evaluated here is a measure of the vertical transport only. As a result, the greater number of rolls emerging in the no-slip than in the free-slip cases explains why in this particular condition more vertical convection emerges from the no-slip cases. In addition, even if more vertical motion occurs in no-slip conditions, we also notice a higher variability of the three free-slip simulations characterized by $kb = 0.5$, 1 and 1.5 than their counterparts in no-slip (see panel (b) of Fig. 5.12). We speculate that this is due to the interaction between convective and stable zones, which are strongly affected by the horizontal winds emerging in free-slip; however, this deserves further future analysis.

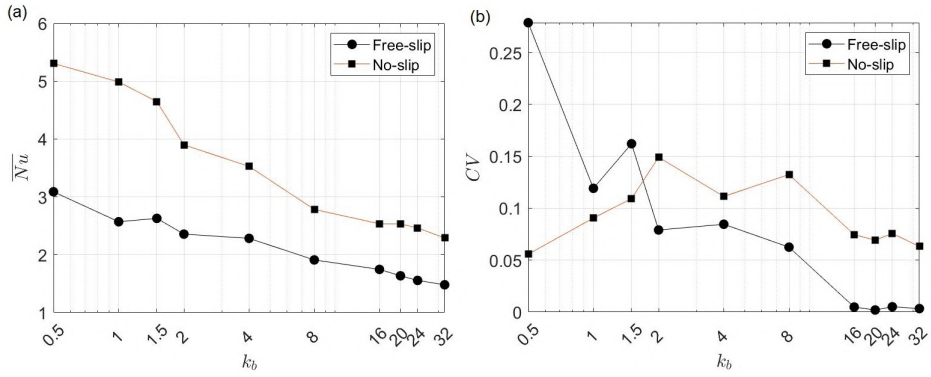

Figure 5.12: (a) Nusselt number $\overline{Nu}$ averaged between $\tau_{conv} = 300 \div 420$ (end of the simulations) as function of the imposed wave number k_b and (b) coefficient of variation CV of $\overline{Nu}$.

5.4 Conclusions

This preliminary study has focused on the juxtaposition of a classical Rayleigh-Bénard configuration, where the the bottom plate is hotter than the top one, and a stable zone where the opposite thermal condition at the boundaries is imposed. This peculiar scheme is obtained through sinusoidal patterns characterized by a global mean temperature equal to zero at both plates and a shifting of the top sine wave with respect to the bottom one (they are in counter-phase). This produces what we called *alternate convection*. The two zones, namely the convective and the stable one (CZ and SZ, respectively), are free to develop with convective motions (CZ) and without them, i.e., no heat transport occurs (SZ). In the case where the wavelength of the perturbation is equal to the aspect-ratio of the domain, i.e, when the lowest possible wave number is imposed, the system exhibits one CZ and one SZ. By increasing the wavelength of the perturbation, more stable and convective zones develop and they start interacting with each other. Unless the frequency of the alternating hot and cold boundaries is not perceived as a small noise in the domain, those zones can coexist even if their mutual interaction begins. Future work is needed to define which wave number(s) can be considered as one or more threshold(s) able to turn down the alternating convection. What clearly emerges is that with increasing frequency of the perturbations, it is hard to distinguish the convective from the stable zones. The more the wave number increases, the more the system looses its energy and tend to come back to an almost stable situation, in which no motions occur due to the overall null temperature difference between the two plates. We identify two main causes for this occurrence. On the one hand, the difference of temperature applied by the sinusoidal thermal b.c. leads to the pure mechanism of horizontal convection, where heating and cooling are applied to different parts of the same horizontal surface of a fluid layer and circulation develops, giving rise to rolls and substantial horizontal velocities (especially with free-slip boundaries). On the other hand, the circulations taking place in each CZ generate instability in the contiguous stable zones, which are eroded by the dragging action of the CZ.

Conclusions

This thesis deals with two crucial aspects of convective heat transfer with thermally inhomogeneous boundary conditions, namely the Urban Heat Islands and the Rayleigh-Bénard problem.

Part I of the work accomplishes the analysis and evaluation of the Urban Heat Island (UHI) effect. It is known that the UHI refers to warmer temperatures experienced by a city with respect to its natural surroundings. This widely investigated phenomenon is usually computed as the difference between urban and rural air temperatures registered by weather stations located in the territory of interest. However, each territory which is subject of UHI studies is certainly characterized by its distinctive orography, climate and peculiarities that make it unique and, for this reason, difficult to be compared with other studies. In addition, the definition of urban-rural pairs of meteorological stations needed for the heat island quantification is a very important and crucial task, since it assesses the UHI intensity itself. Despite the different studies on the UHI, at the current stage a robust metric to select urban and rural sites is still missing. The first Chapter of this work aims to fill this gap by proposing a novel method to identify them in a way that is intended to be as objective and general as possible. The Mean Temperature Difference (MTD) method is based on the assumption to not know *a priori* whether a site falls in the "urban" or "rural" definition. Through a simple equation based on the difference of temperatures among a heterogeneous group of weather stations, the MTD identifies their average thermal pattern. Afterwards, a Principal Component Analysis is adopted to discern groups of common thermal behaviors and to cluster them into the two classes of interest, i.e., "urban" or "rural". The method has been tested for the stations available around Turin (Italy), showing results that very well agree with the authors' knowledge of the territory. It also proved to be very robust and reliable with limited datasets and another city in the Piemonte region, for which data were available.
After having identified the basic metric, the work goes on with the effective evaluation of the Urban Heat Island effect over Turin, by focusing on 14 years of data availability. The main aim of the study is the characterization of the average seasonal variations of temperatures. The analyses focus on five ground-level stations, defined through the MTD method as three urban and two rural. In particular, the most urban station among the three – i.e.,

the one showing higher mean temperature values than the other two – is compared with one rural station located in the North and one in the South of Turin. This allows us to fully characterize the average heat island of Turin from a spatial point of view. The outcomes show that the UHI effect is on average stronger along the city-North axis than along the city-South direction, with a mean value during winter and summer nights that reaches 4.5-5°C. Since the UHI effect is strictly coupled with the so-called Urban Dry Island phenomenon, the analysis of absolute humidity data taken from the same five stations as above, shows that Turin is on average always drier than the natural lands located in the North and in the South of the city. The vertical profiles of the UHI are also explored thanks to the availability of three microwave radiometers, which produce measurements up to 600 m above the ground level. Therefore, we highlight the average features of the Urban Boundary Layer of Turin: the height up to which the influence of the city as a thermal heterogeneity is perceived in the overlying atmosphere reaches an elevation of 150-200 m a.g.l. The final Chapter of *Part I* adopts the same ground-level stations as above to validate a new urban parameterization recently implemented in the numerical weather prediction COSMO model. The new urban scheme, called TERRA_URB, results remarkably capable of capturing the Urban Heat Island effect over Turin, since the model outcomes are strongly in agreement with the observational data. Due to the transition of the Consortium from the COSMO model to the new ICON model, another Priority Project called CITTA' (City Induced Temperature change Through A'dvanced modelling) is ongoing. The aim of CITTA' is to transfer to the ICON model the achievements obtained with the Priority Tasks ÆVUS and ÆVUS2 – which are summarized in the final Chapter of *Part I*.

Part II of this work shifts the attention to another poorly-investigated aspect of thermal convection with non-homogeneous boundaries: the Rayleigh-Bénard (RB) problem. The first Chapter of this Part explores the effects produced by sinusoidal patterns on the so-called clustering phenomenon occurring in RB convection. In this way, we modify the classical problem associated with a fluid confined between two thermally-uniform plates to study how the large-scale patterns – deriving from the clustering between thermals of the same sign – interact with perturbations at the boundaries. The thermal modifications that we impose to the boundary conditions of a RB scheme – through sinusoidal patterns – do not alter the equations governing the problem, since the average temperature characterizing each plate is maintained constant. This allows us to investigate a wide range of

sinusoidal patterns by just varying the wave number of the perturbation imposed at the boundaries. The analysis of such configurations may be of interest both from a theoretical and a practical point of view. Theoretically, few studies have focused on the effects produced by thermal boundary conditions on a RB system so far. From a practical viewpoint, it is not a novel thing that RB systems have been studied to model convection in real world, such as the Earth's mantle, oceans or the atmosphere. Actually, the conceptual clearness of the problem allows one to understand the basic physics behind a phenomena. In this context, the effects produced by sinusoidal thermal anomalies can be seen in light of an idealization of cities, which have different thermal properties than the pervious landscape nearby. Do boundary thermal anomalies interact with the way convection develops? If so, in which ways and at what scales? We try to answer this question and to contribute to the literature of RB convection through a systematic analysis of nonuniform temperature conditions on both top and bottom boundaries, in the fully turbulent regime. In doing so, we compare the classical scheme characterized by uniform plates with two- and three-dimensional domains with non-uniform boundary anomalies. Our results show that two spatial convective scales occur: the one due to the self-organized clustering of plumes (typical of the classical RB scheme with homogeneous conditions) and the scale induced by the boundary heterogeneities. The latter drives the convection patterning, both in 3D and 2D, when the wavelength of the perturbation is comparable with the self-organized one.
The last Chapter of *Part II* concludes the thesis with an insight about another idealization, never explored so far. We develop a new RB configuration in two-dimensions made of the juxtaposition of one (or more) standard Rayleigh-Bénard model(s) and its opposite situation, i.e., stable zone(s) characterized by a cold portion at the bottom and a hot plate at the top surface. This is achieved by adopting sinusoidal thermal patterns at the boundaries set in counter-phase with respect to the vertical direction. Each plate exhibits a global zero mean temperature, but the particular configuration imposed at the boundary conditions allows the occurrence of local thermal gradients. Despite the study being at a preliminary stage, our results show that convection still occurs and affects the vertical and horizontal motions in the system. Since the average temperature between the two plates is equal to zero, this is quite a counter-intuitive outcome. In addition, by increasing the frequency of the boundary anomalies, i.e., the wave number of the sinusoidal patterns, the perturbations seem no more able to be perceived as a local modification of the temperature gradients and, therefore,

convection is gradually dampened. The analytical simplicity provided by this two-dimensional idealized model represents just the starting point for future research work and possible generalizations of our results. In particular, the phenomenon which we call *alternate convection* may be of interest to study the mutual action between convective and stable zones, such as a hot spot at the base (like a city) with respect to a colder one nearby (rural land).

To sum up, this thesis focuses on two aspects of thermal convection with non uniform boundary conditions, namely the Urban Heat Island effect and the Rayleigh-Bénard problem. On the one hand, the thermal heterogeneity is represented by a city with respect to the surrounding natural landscape; on the other hand, sinusoidal patterns yield non-uniform temperatures at the boundaries of a Rayleigh-Bénard scheme. Despite the different perspectives, this work shows the relevance to analyze the problem of convective heat transfer by taking into account the thermal boundary conditions, which play a key role on the way convection develops in environmental fluids. As regards the Urban Heat Island effect, it is crucial to carefully choose the measurement sites for (i) a better quantification of the phenomenon and (ii) a precise analysis of its spatial effects. Regarding the Rayleigh-Bénard problem, thermal heterogeneities have proven to contribute to the formation of novel structures, characterized by a particular scale, which interact with a thermally uniform system.

Appendices

A

Appendix A: Supplementary material for Chapter 1

Results of the applicability of the MTD

With the aim of evaluating to which extent the Mean Temperature Difference (MTD) method is applicable to different datasets (in length or density) or different environments, a sensitivity analysis is performed. Results are reported in this Appendix, which is organized in four sections: Section A.1 is about the minimum duration of the period considered in the analysis, Section A.2 regards the temporal resolution of the selected period, Section A.3 concerns the minimum number of stations that can enter the procedure and Section A.4 reports another case study, geographically different from Turin.

A.1 Duration of the period considered in the analysis

In our application, in order to be as general as possible, the yearly scale in considered. Therefore, this Section addresses the issue about how many years are needed for the method to work. We evaluated the minimum window of 12 months. Figure A.1 illustrates the PCA outcome for the year 2020, but the same results are found for any other year. All the 11 stations available in the metropolitan area of Turin are considered in the spatial mean of Eq. 1.1. The variable $T^S_{(i,M)}$ is computed as the climatological average over the months and hours referring to the year 2020 alone. The method successfully provides the same clustering of stations obtained in Fig. 1.3 of Chapter 1. This means that the method is robust enough even when the dataset at hand is strongly reduced. In fact, even with one year only, Figure A.1 (c) clearly shows the thermal behavior characterizing the Urban

Heat Island and, therefore, it is possible to associate the first principal component to the urban or rural properties of a site. The projections onto the first principal component clearly distinguish the same two groups of stations identified by using the entire dataset.

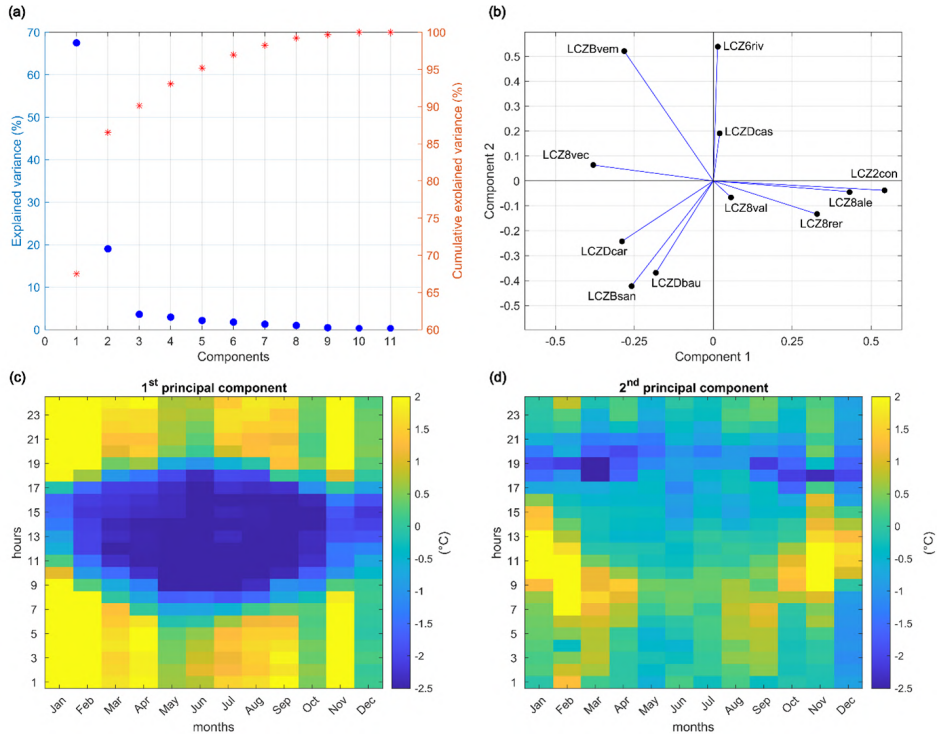

Figure A.1: Principal Component Analysis (PCA) on the dataset including all the 11 stations, but only 1 year of recorded temperatures (2020): **(a)** percentage of explained variance for each of the 11 components (blue dots, left axis) and their cumulative values (red asterisks, right axis); **(b)** space of the first (x-axis) and second (y-axis) principal components; **(c)**, **(d)** representation of the two principal components of the MTD (colour scales in degrees Celsius).

A.2 Temporal resolution of the selected period

Results of the method applied on three-hourly temperature measurements are shown in Fig. A.2. The considered dataset represents a subset of the original one, where the temperature records are at taken at 00, 03, 06, 09, 12, 15, 18 and 21 UTC. The method efficiently provides the same results of Chapter 1: three stations are clustered in the urban thermal pattern (*LCZ2con*, *LCZ8ale* and *LCZ8rer*), five stations pertain to the rural

category (*LCZ8vec*, *LCZBsan*, *LCZBvem*, *LCZDbau* and *LCZDcar*) and the remaining stations of *LCZ6riv*, *LCZ8val* and *LCZDcas* are characterized by an intermediate behavior, since the projection onto the first principal component is almost zero.

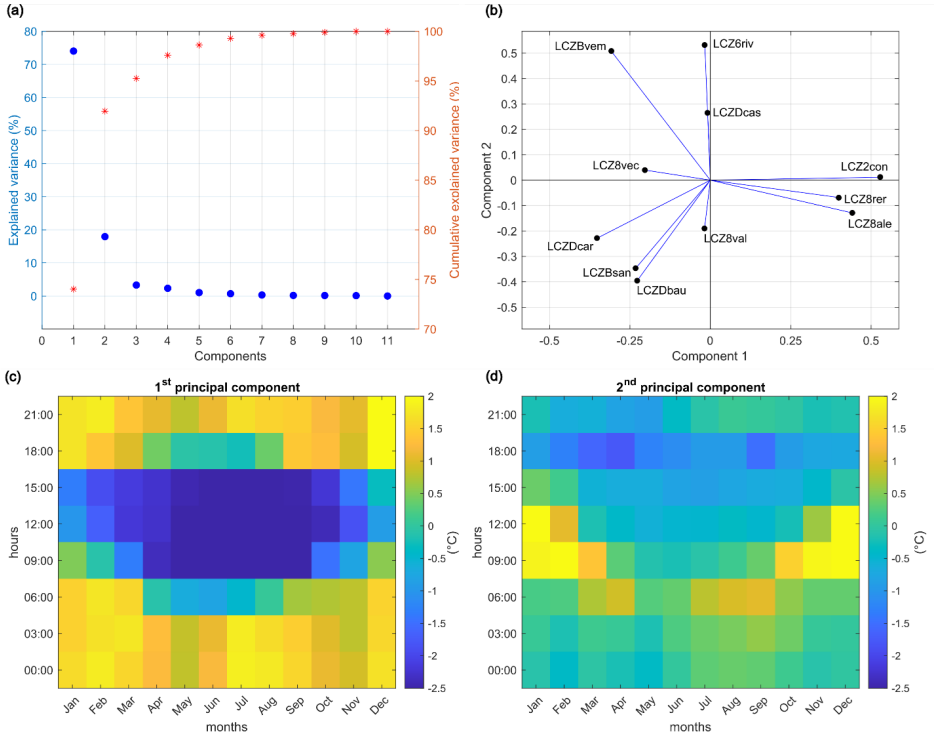

Figure A.2: Principal Component Analysis (PCA) on the dataset including all the 14 years of recorded temperatures available and all the 11 stations, but with 3-hourly temperature measurements. For the description of each panel **(a)-(d)** please refer to Fig. A.1.

A.3 Minimum number of stations

Figures A.3 and A.4 show the results of the method applied on a dataset with less stations than the original dataset. We start describing the first case shown in Fig. A.3, where 5 stations are excluded from the analysis: *LCZBvem*, *LCZ8vec*, *LCZBsan*, *LCZDbau* and *LCZDcar*. These stations correspond to those identified as rural in Chapter 1. The first principal component, which accounts for almost 80% of the total variance (see panel (a) in Figure A.3) describes the thermal differences between daytime and

night hours: therefore, we associate it to the urban or rural properties of a site. Albeit the exclusion of the five rural stations, the method still distinguishes two clear clusters associated with the first principal component, as shown in Fig. A.3 (b). In particular, the stations of *LCZ2con*, *LCZ8ale* and *LCZ8rer* are characterized by substantially negative projections onto the first principal component, while *LCZ6riv*, *LCZ8val* and *LCZDcas* by substantially positive projections. This means that these two clearly separate groups pertain to different thermal behaviors, which are captured by the PCA even when the dataset is reduced.

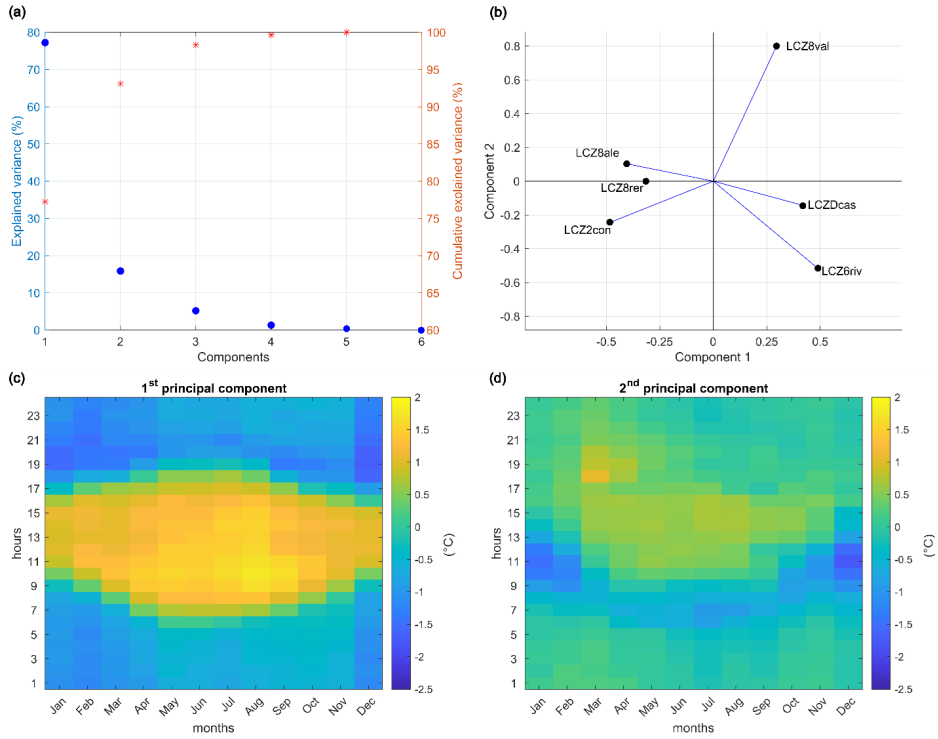

Figure A.3: Principal Component Analysis (PCA) on the dataset including all the 14 years of recorded temperatures available, but considering only 6 stations out of 11. The excluded stations are: *LCZBvem*, *LCZ8vec*, *LCZBsan*, *LCZDbau* and *LCZDcar*. For the description of each panel **(a)-(d)** please refer to Fig. A.1.

In the second case, shown in Fig. A.4, we performed the analysis on the 5 rural stations previously excluded. Figure A.3 shows that the clustering is ambiguous and the main pattern described by the signal cannot be related to urbanity/rurality, but resembles the signal distinguishing the different thermal regime between North and South. Therefore, in this case the

first component of the PCA distinguishes the stations located in the North (*LCZBvem* and *LCZ8vec*, characterized by a positive projection onto the first p.c.) and in the South (*LCZBsan*, *LCZDbau* and *LCZDcar*). However, even in cases like this one, the method shows a warning about its applicability, meaning that the considered stations are not a good choice in selecting urban/rural pairs for UHI.

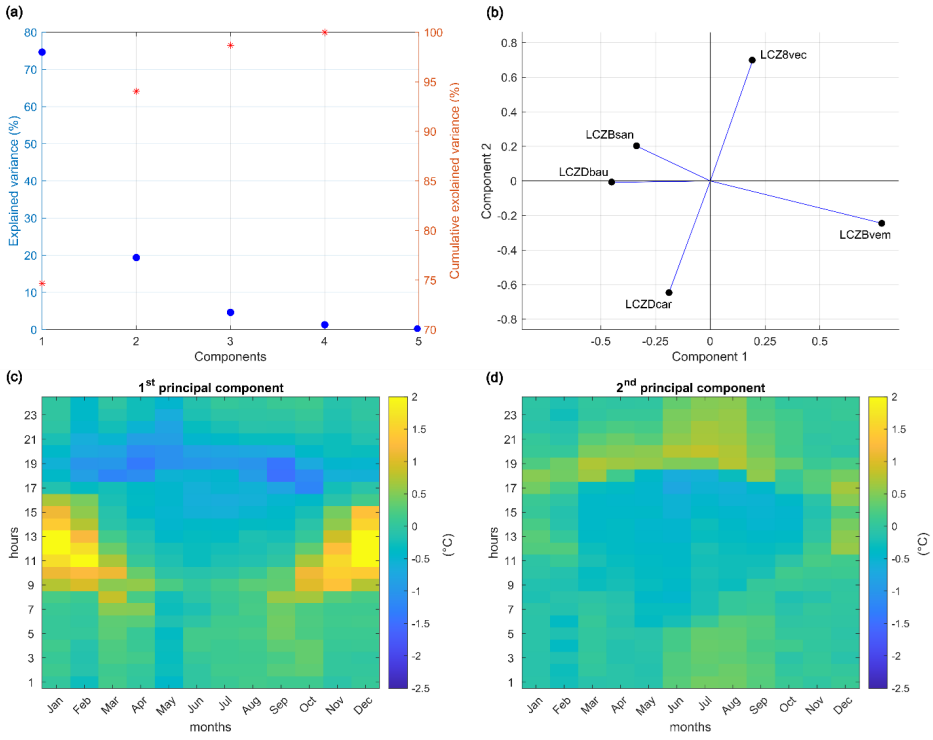

Figure A.4: Principal Component Analysis (PCA) on the dataset including all the 14 years of recorded temperatures available, but considering only 5 stations out of 11. The excluded sites are: *LCZ2con*, *LCZ6riv*, *LCZ6val*, *LCZ8ale*, *LCZ8rer* and *LCZDcas*. For the description of each panel **(a)-(d)** please refer to Fig. A.1.

A.4 Application of MTD to another domain: the city of Cuneo

Finally, this section shows the application of the method on a different dataset and domain: the city of Cuneo, North-West of Italy (see Fig. A.5).

Cuneo is located at a mean elevation of about 550 m a.s.l. and its population is about 60000 inhabitants. Being at the foot of the Alps,

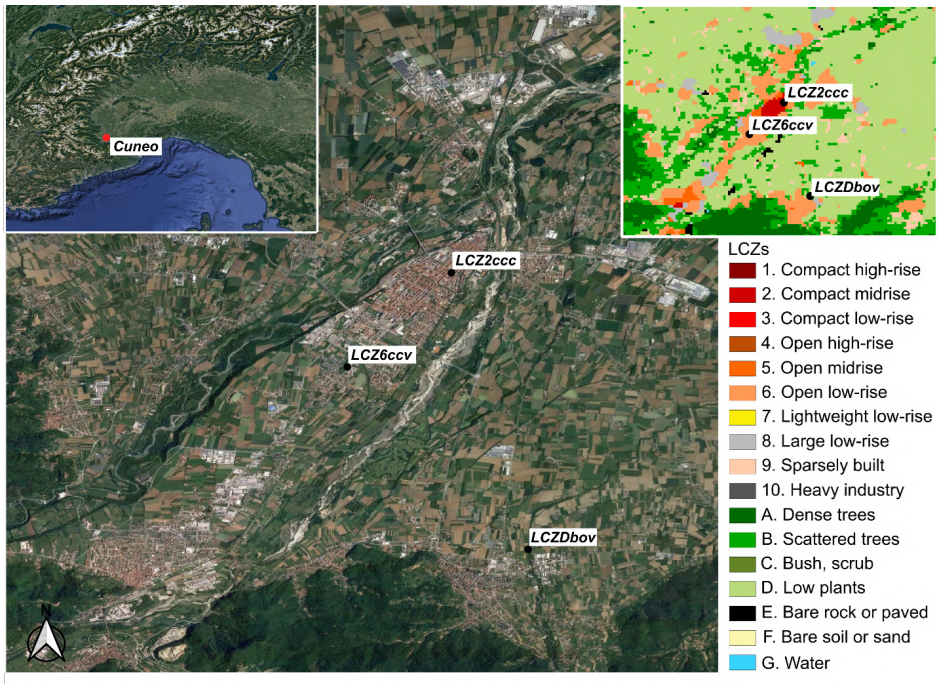

Figure A.5: Map of the city of Cuneo (North-West of Italy, in the northwest inset). The three measurement stations are marked with black dots. North-East inset: LCZ map from [69].

Cuneo receives more snow during winter than Turin [77]. Differently from Turin, Cuneo is provided with two weather stations in the urban area only, namely Cuneo Camera di Commercio (*LCZ2ccc*) and Cuneo Cascina Vecchia (*LCZ6ccv*). In the surroundings, the station of Boves (*LCZDbov*, 575 m a.s.l.) is the only one suitable for a sufficiently strong analysis (Fig. A.5). In addition, the hourly temperatures are available from July 2019 to December 2020, meaning that only 18 months of data can be used in the analysis. Thanks to all these differences with Turin, Cuneo represents an effective example to evaluate whether the MTD works on other case studies. Figure A.6 shows that MTD is efficient in characterizing the thermal patterns of the three stations. Firstly, the variance explained by the first principal component accounts for almost 95% of the total (panel (a) of Fig. A.6), meaning that it represents the greatest part of the signal identified by the PCA. This signal is shown in panel (c) of Fig. A.6: as widely discussed, the higher temperatures at night times than during the day are associated to an urban thermal behavior. As a result, a positive projection onto the first

principal component refers to an urban characterization, while a negative one represents a rural behavior. Looking at these projections (Fig. A.6 (b)), it is clear that *LCZ2ccc* is deemed as urban (positive projection onto the first p.c.) and *LCZDbov* as rural (negative projection onto the first p.c.). Instead, the third station (*LCZ6ccv*) exhibits an intermediate behavior between the other two, since its projection onto the first p.c. is negligible if compared with *LCZ2ccc* and *LCZDbov*.

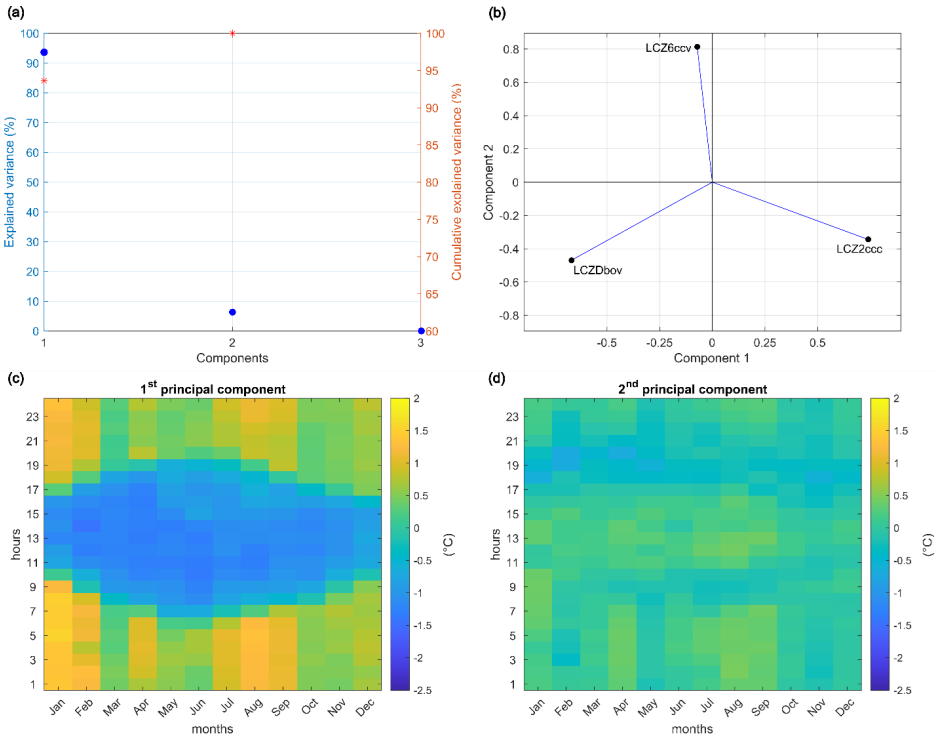

Figure A.6: Principal Component Analysis (PCA) on the city of Cuneo. The dataset includes all the years of recorded temperatures available (18 months), and the three measurement sites. For the description of each panel **(a)-(d)** please refer to Fig. A.1.

B

Appendix B: Supplementary material for Chapter 2

Statistical significance of the observations through the two-sample t-test

With the aim of evaluating the uncertainty of both the ground-level and the vertical data, the two-sample t-test, also known as Welch's t-test [113], was performed. The null hypothesis is that the data come from independent random samples from normal distributions with equal means and unequal variances. As regards the ground-level data, the test was used to verify whether significant differences exist (or not) among (i) the urban recordings and the rural ones (ii) the two different rural stations and (iii) the three urban sites. The first verification fully fits and addresses the main goal of the work, since the difference between urban and rural stations is the core of the Urban Heat Island (UHI) phenomenon. The application of the t-test upon the rural sites allowed us an objective distinction between the southern and northern thermal pattern, which leads to different UHI intensities with respect to the South and the North of Turin. Finally, the third test concerned the differences among URB1, URB2 and URB3 and it provided a further explanation for the selection of the "most urban" station (URB1) as the reference one to compute the UHI, since significantly higher temperatures are observed here than in URB2 or URB3. Regarding the vertical data, the test was applied to detect significant differences among the urban and rural radiometers, since only three radiometers are available to compute the vertical structure of the UHI. The Appendix is organized as follows: the results of the t-test upon the ground-level stations are reported in Section B.1, while those about the vertical measurements are shown in Section B.2.

B.1 Ground-level stations

Figures B.1, B.2 and B.3 show the p-values as function of the hours of the day. The significance level is set to 5% in every case. The outcome of the test is straightforward: whenever two samples are significantly different at the 5% significance level, the null hypothesis is rejected. The first remarkable result regards the two urban stations URB2 and URB3: they are not significantly different for all the seasons and hours (see panel (c) in Figs. B.1, B.2 and B.3). For this reason, the focus of the main text is on the most urban station URB1, which is indeed the one characterized by significantly higher temperatures during the night than URB2 and URB3 (Fig. B.1 (c)). Therefore, the UHI has been computed comparing the couples URB1-RURs and URB1-RURn.

Another relevant outcome regards whether significant differences exist between the two rural stations RURs and RURn. Since in the main text a wider discussion is made on the different thermal behavior between the South and the North of Turin, we have tested also the null hypothesis over the southern and the northern rural sites. Their differences are not statistically significant (at the 5% level) in the following cases:

i for the mean daily cycles of temperature, during few daytimes (i.e., when the solar radiation gets the two rural sites almost equally warm, see Fig. B.1 (b));

ii for the rate of temperature (Fig. B.2, panel (b)), during winter and fall nights, before sunrise and after sunset respectively, and during daytime in summer;

iii for the mean daily cycles of the absolute humidity (Fig. B.3, panel (b)), when the solar radiation is maximum, i.e., during the day in summer and autumn.

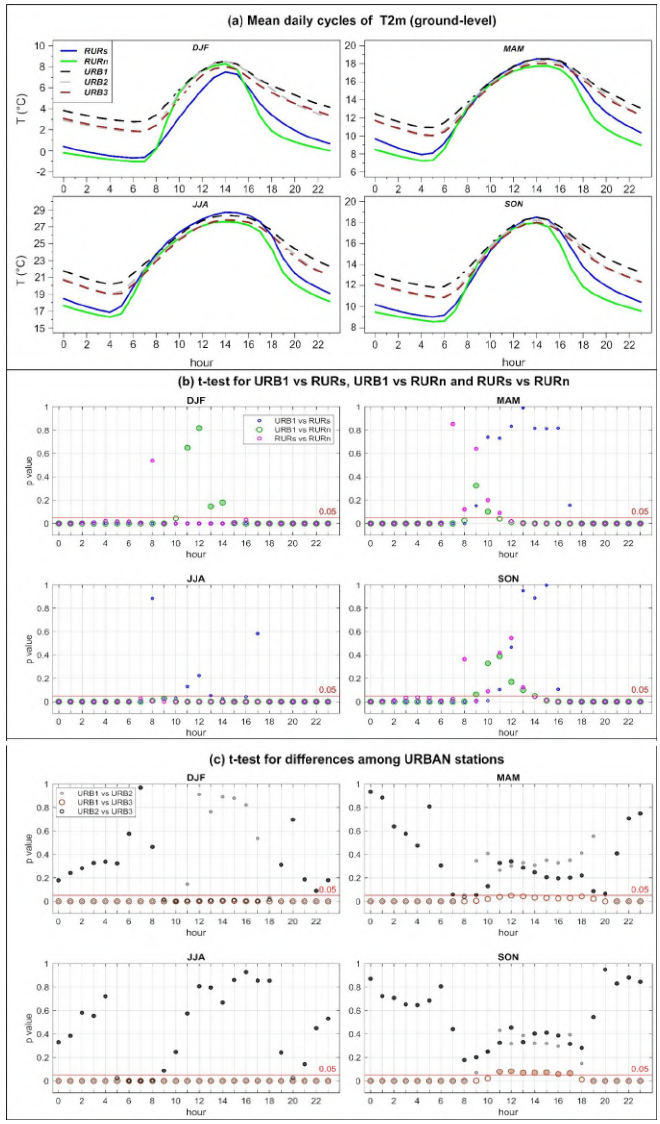

Figure B.1: **(a)** Mean daily cycles of the ground-level temperature, as reported in Fig. 2.2 of Chapter 2. Panels **(b)** and **(c)** report the p-value as a function of the hours. The blank dots refer to the rejection of the null hypothesis (two data are from populations with equal means), while filled dots stand for the failure to reject the null hypothesis. The red line marks the significance level of 5%: dots below the line mark means that are statistically different, while dots above indicate that means are not statistically different.

The results of the 2-m temperatures (Fig. B.1, panel (b)) show that the urban station URB1 is significantly different from the two rural stations

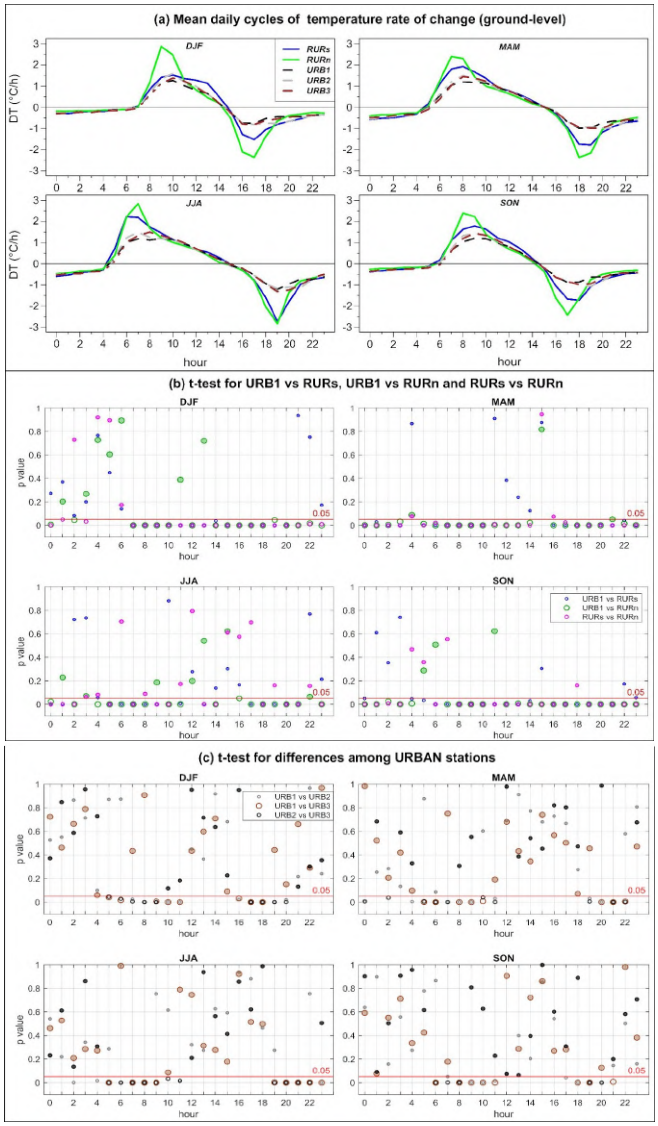

Figure B.2: **(a)** Mean daily cycles of the temperature rate of change, as in Fig. 2.3 of Chapter 2. **(b)** and **(c)**: P-value as a function of the hours. Symbols as in Fig. B.1.

during all nights over all seasons, in fact at night the blank dots are all below the p-value threshold.

The results of the temperature rate of change (Fig. B.2) show that the differences between the urban and the rural stations are statistically significant just after sunrise and after sunset, as it has been explained in the

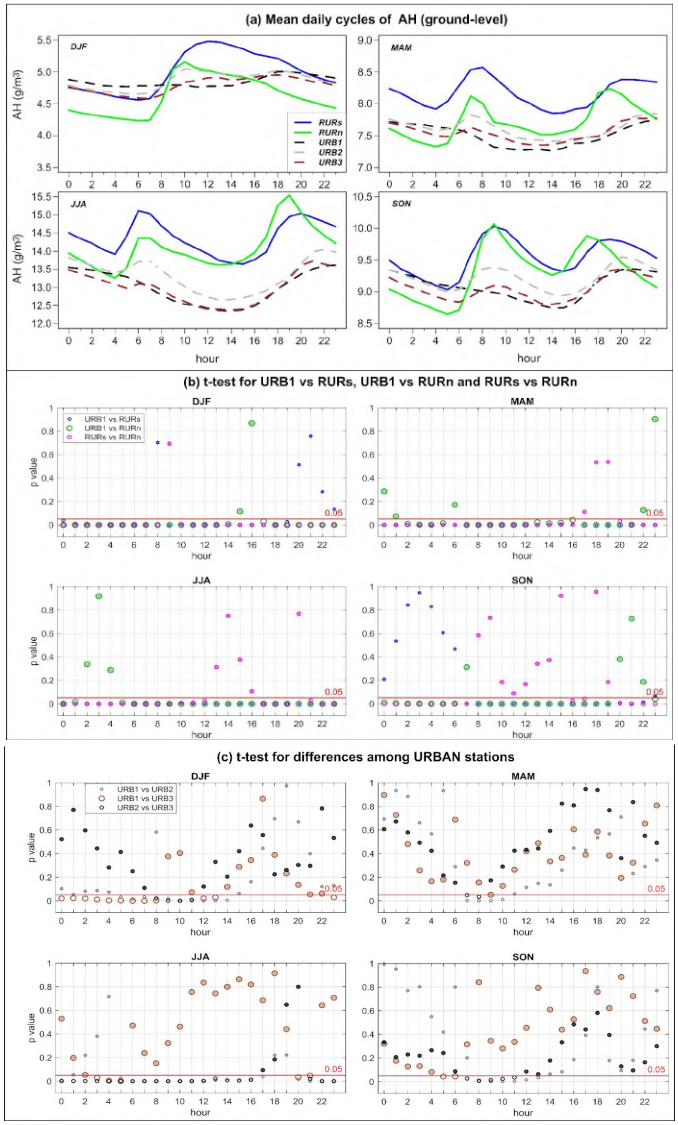

Figure B.3: **(a)** Mean daily cycles of the absolute humidity, as in Fig. 2.5 of Chapter 2. **(b)** and **(c)**: P-value as a function of the hours. Symbols as in Fig. B.1.

main manuscript. Otherwise, there is a failure to reject the null hypothesis and, therefore, there is no significant difference between the ROC of URB1 versus the ROC of RURs and RURn, respectively (filled dots above the p-value threshold).

The differences in terms of absolute humidity (See Fig. B.3, panel (b))

between URB1-RURn and URB1-RURs, respectively, are almost always significant during winter (DJF), spring (MAM) and summer (JJA), except when the curves intersect. Instead, a non-significant difference between URB1 and RURs is detected between 00 UTC and 06 UTC in the morning during autumn (SON) and between URB1 and RURn after sunset in SON.

B.2 Vertical profiles

The results of the vertical temperature profiles are shown in Figure IV and the significance level is set to 5%, like in Section 1. In this case, the p-values are plotted as a function of the vertical levels scanned by the radiometers. As for the ground-level measurements, the null hypothesis is rejected when the urban samples are significantly different than the two rural ones. The outcomes are well in agreement with the mean vertical profiles (top row in Fig. IV): the differences are statistically significant for all the seasons up to the boundary layer height, which has been widely discussed in the main text. Note that during summer (JJA) the cold lens detected around 250 and 350 m a.g.l. is statistically significant both for the northern (radRn) and the southern (radRs) radiometers. The significant difference between radU and radRs continues along the whole vertical column above 350 m a.g.l.

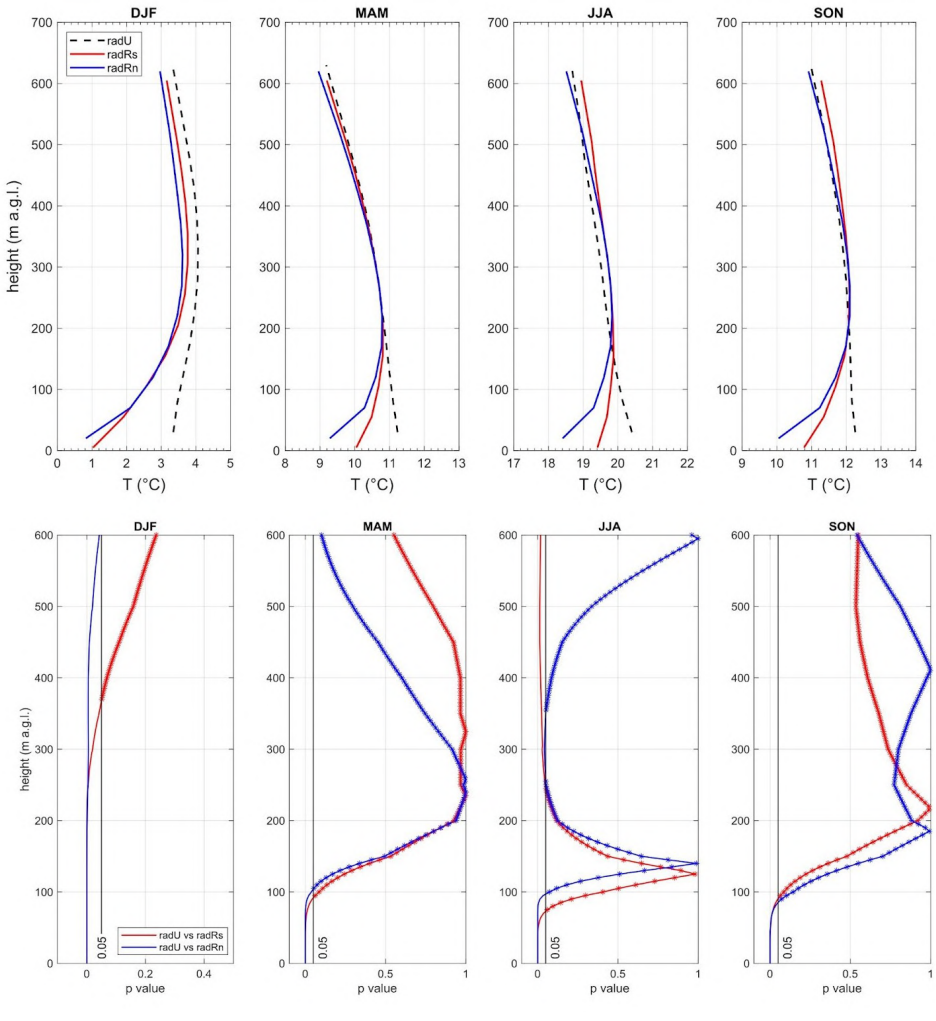

Figure B.4: Top row: mean nocturnal vertical profiles of temperature, as in Fig. 2.9 of Chapter 2. Bottom rom: p-value as a function of the height (meters above the ground level). The continuous (red and blue) lines indicate the rejection of the null hypothesis (two data are from populations with equal means), while the asterisks represent the failure to reject the null hypothesis. The vertical gray line marks the significance level of 5%: asterisks at the right-hand side of this line indicate that temperature profiles are not statistically different, while they are statistically different when red and blue lines fall at the left-hand side.

C

Appendix C: Supplementary material for Chapter 3

C.1 The "urban double-counting effect"

The output external parameters used by COSMO are generated by the EXTPAR software that aggregates various raw datasets to the target grid and performs general consistency checks [198]. Some external parameters are calculated as a function of land use classes and might therefore depend on urban fraction (artificial surfaces, class=19 in GLOBCOVER classification, which corresponds to URBAN parameter). The parameters affected by the presence of artificial surfaces are: roughness length (Z0 [m]), minimum / maximum ground fraction covered by plants in the vegetation period (PLCOV_MN / PLCOV_MX), ground fraction covered by deciduous / evergreen forest (FOR_D / FOR_E), skin conductivity (SKC [Wm-1K-1]), root depth (ROOTDP [m]), minimum / maximum leaf area index in the vegetation period (LAI_MN / LAI_MX), minimum plant resistance (RSMIN [sm-1]) and long wave surface emissivity (EMISS_RAD). If TU is switched off, the effect of urban surfaces is then represented in increased roughness and reduced green vegetation fraction and characteristics, the so-called 'zero-order urban model', which is currently implemented in the operational COSMO model. If TU is activated, a tile approach is implemented in which each cell is divided into two tiles, an urban tile and a natural tile. The fraction of the urban tile is defined by the impervious surface area (ISA) parameter. The SURY parameterization is used to calculate the model variables for the urban tile, whereas the zero-order urban description provides the model variables for the natural tile. However, the current external parameters associated with the natural tile are those provided by EXTPAR and are still calculated by considering the urban contribution: this is what we call the 'urban double-counting effect', as the presence of the city is

counted twice, once by the TU scheme and once by the zero-order urban model that integrates urban characteristics into the natural tile. In order to avoid this double-counting effect, a new dataset for natural tile has been built from the one provided by EXTPAR, where the urban-based external parameters have been calculated according to the functions implemented in EXTPAR but re-weighted excluding GLOBCOVER's URBAN class. A python routine that accounts for this double-counting is contained in the WUDAPT-to-COSMO converter [69] and it is publicly available on GitHub [250].

C.2 Characteristics of the stations used for model validation

The following tables display the specifics of the weather stations, for Turin (Tab. C.1), for Naples (Tab. C.2) and for Moscow (Tab. C.3) respectively. The modelled elevation is extracted from EXTPAR; ISA values are from EXTPAR for Turin and Naples as well, while for Moscow they were obtained with the GIS-based approach described in Chapter 3 [209]. Finally, the Local Climate Zone (LCZ) classes are extracted from the European LCZ map [66, 69]. Both ISA and especially the LCZ class, allowed the classification of each station into urban or rural, thanks to its universality of application. A summary of the LCZ types involved is listed below, taken from Stewart and Oke's study [59]:

- urban, LCZ 2: "compact midrise"; dense mix of midrise buildings (3-9 stories). Few or no trees, land cover mostly paved;
- urban, LCZ 4: "open high-rise"; open arrangement of tall buildings to tens of stories. Abundance of pervious land cover (low plants, scattered trees);
- urban, LCZ 5: "open midrise"; open arrangement of midrise buildings (3-9 stories). Abundance of pervious land cover;
- urban LCZ 6: "open low-rise"; open arrangement of low-rise buildings (1-3 stories). Abundance of pervious land cover;
- urban, LCZ 8: "large low-rise"; open arrangement of large low-rise buildings (1-3 stories). Few or no trees, land cover mostly paved;

- rural, LCZ A: "dense trees"; heavily wooded landscape of deciduous and/or evergreen trees. Land cover mostly pervious (low plants). Zone function: natural forest, tree cultivation, urban park;
- rural, LCZ B: "scattered trees"; same as LCZ A, but lightly wooded;
- rural, LCZ D: "low plants"; featureless landscape of grass or herbaceous plants/crops. Few or no trees. Zone function: natural grassland, agriculture, urban park.

Table C.1: Turin, Piedmont domain, Italy.

Station Name	Lat	Lon	Elevation, Actual (m a.s.l.)	Elevation, Model (m a.s.l.)	ISA (%)	LCZ	Classification
Reiss Romoli	45.113	7.671	270	246	0.67	8	urban
Alenia	45.081	7.612	320	279	0.62	8	urban
Consolata	45.077	7.679	290	248	0.93	2	urban
Bauducchi	44.961	7.710	226	225	0.09	D	rural
Santena-Banna	44.946	7.783	238	234	0.14	D	rural
Carmagnola	44.887	7.688	232	232	0.02	D	rural

Table C.2: Naples, Campania domain, Italy.

Station Name	Lat	Lon	Elevation, Actual (m a.s.l.)	Elevation, Model (m a.s.l.)	ISA (%)	LCZ	Classification
Napoli	40.9375	14.0759	13	61	0.80	8	urban
S. Marco Evangelista	41.0225	14.3358	31	22	0.72	8	urban
Grazzanise	41.0542	14.0913	6	9	0.02	D	rural
Rocca d'Evandro	41.4244	13.8800	62	55	0.09	D	rural
Alife	41.3391	14.3336	117	117	0.01	D	rural

Table C.3: Moscow megacity, Russia.

Station Name	Lat	Lon	Elevation, Actual (m a.s.l.)	Elevation, Model (m a.s.l.)	ISA (%)	LCZ	Classification
Dolgoprudnyy	55.93027	37.51944	193	195	0.64	5	urban
Strogino	55.79694	37.39527	145	155	0.70	4	urban
VDNKh	55.83138	37.62194	148	145	0.00	A/B/5	urban
Balchug	55.74555	37.63	123	129	0.88	2	urban
MSU	55.70694	37.5222	192	183	0.49	5/B	urban
Klin	56.35	36.74972	165	171	0.08	6/8	rural
Novo-Iyerusalim	55.90638	36.825	159	161	0.00	6	rural
Naro-Fominsk	55.38722	36.70111	190	200	0.00	D	rural
Maloyaroslavets	55.01694	36.48583	195	203	0.26	6	rural
Dmitrov	56.3575	37.55722	178	180	0.43	6	rural
Serpukhov	54.9225	37.46556	164	165	0.19	D	rural
Alexandrov	56.4	38.75055	185	184	0.00	6	rural
Pavlovsky Posad	55.7716	38.6925	134	133	0.22	6	rural
Kolomna	55.1422	38.7325	112	111	0.03	6	rural

C.3 Figures of Naples and Moscow domains

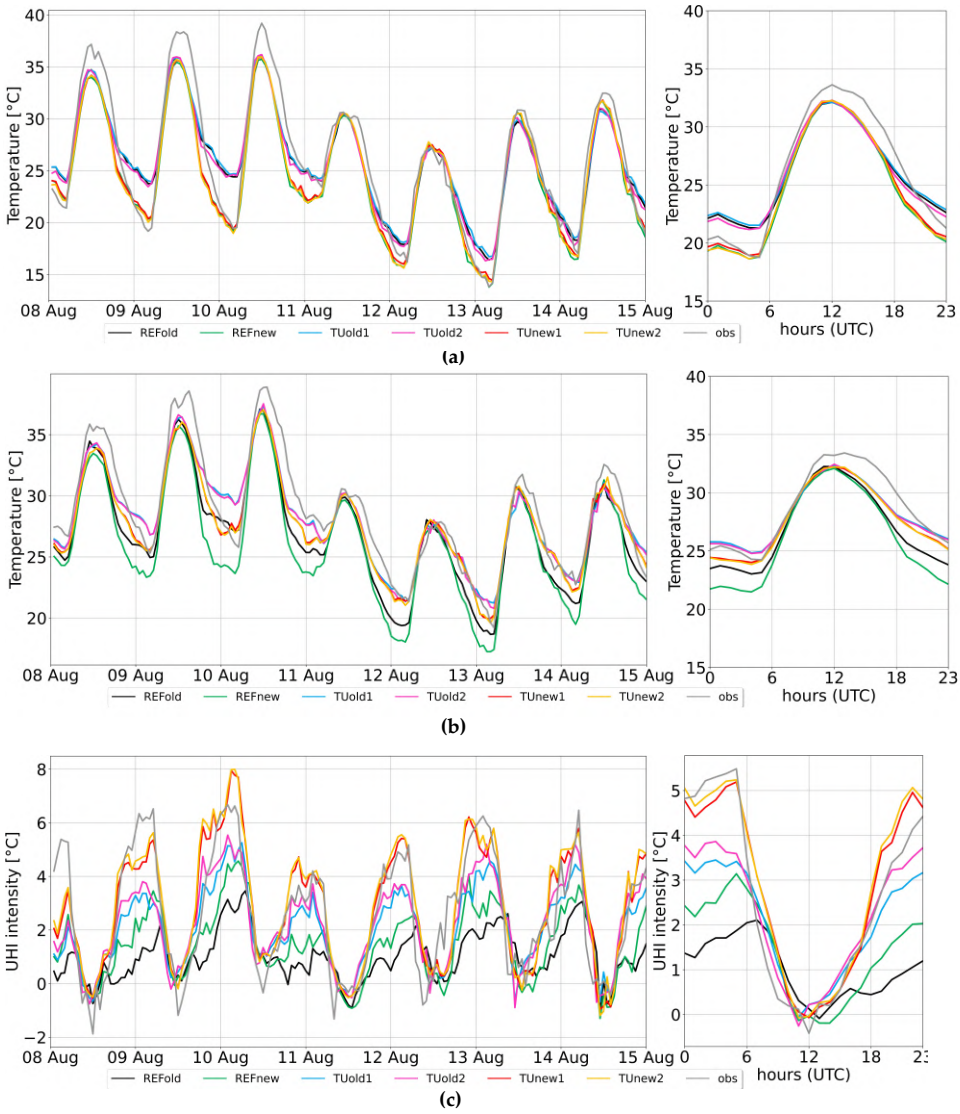

Figure C.1: Naples domain, Italy: **(a)** mean rural T2m, **(b)** mean urban T2m and **(c)** Urban Heat Island intensity during the week 8-14 August 2017. Subplots on the right show the mean daily cycles of the rural temperature and UHI intensity.

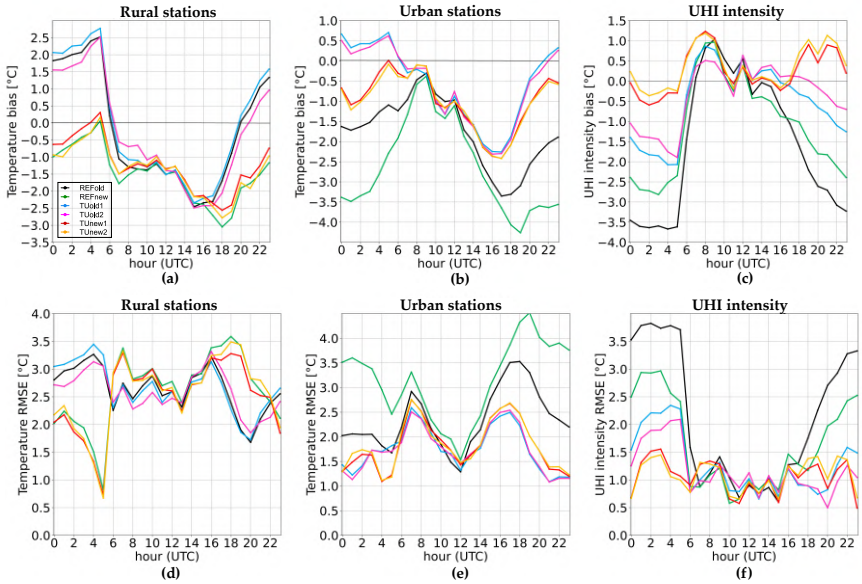

Figure C.2: Naples domain, Italy: mean biases and root-mean square errors of T2m, evaluated over rural **(a,d)** and urban **(b,e)** stations; mean biases and root-mean square errors of UHI intensity for urban stations **(c,f)**.

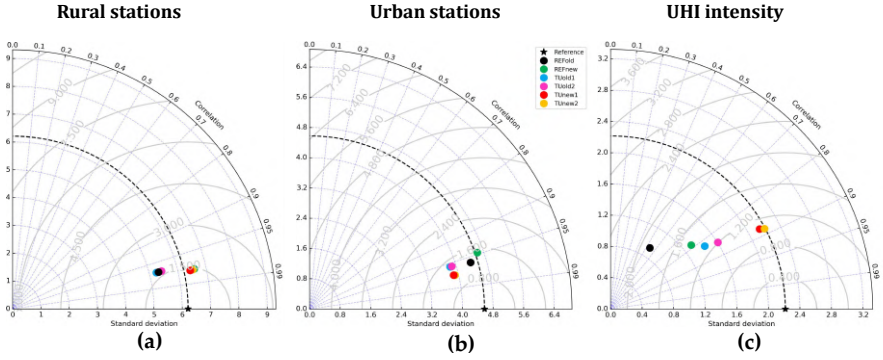

Figure C.3: Naples domain, Italy: taylor diagrams for rural stations **(a)**, urban stations **(b)** and UHI intensity **(c)**.

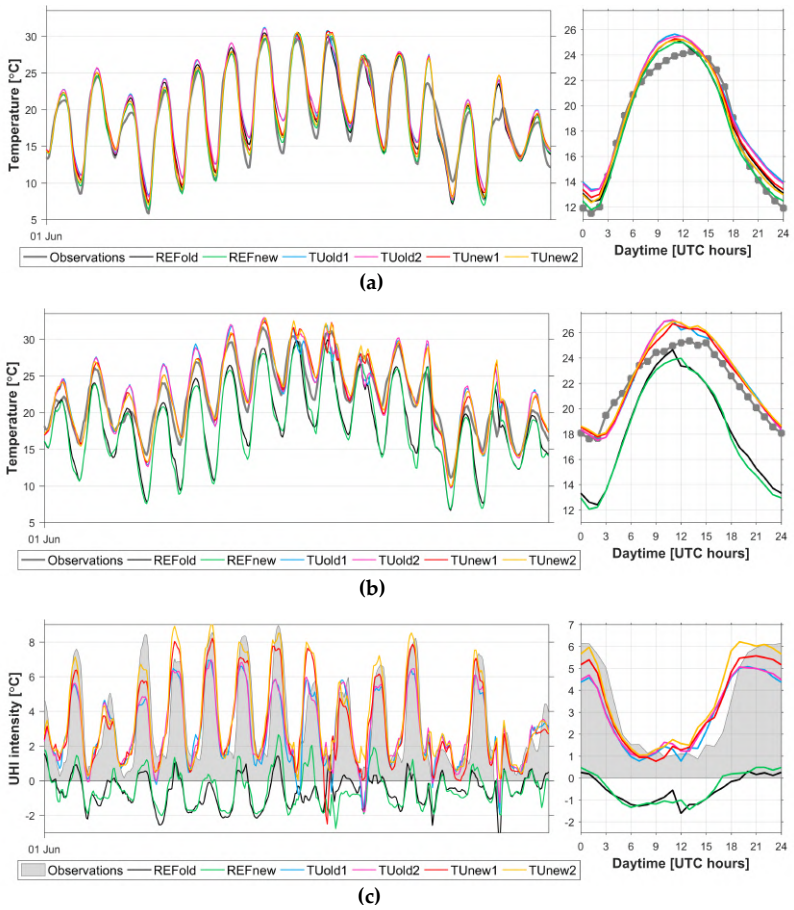

Figure C.4: Moscow domain, Russia: dynamics of observed and modelled values of the mean rural T2m, averaged over 9 selected rural stations in Moscow region **(a)**, T2m at Balchug weather station at the city center **(b)** and urban heat island intensity for this station **(c)** during the considered period of 1-16 June 2019. Subplots on the right show the mean daily cycles of the rural temperature and UHI intensity. Observed and modelled time series in left subplots are smoothed by a running mean with 3-hourly window.

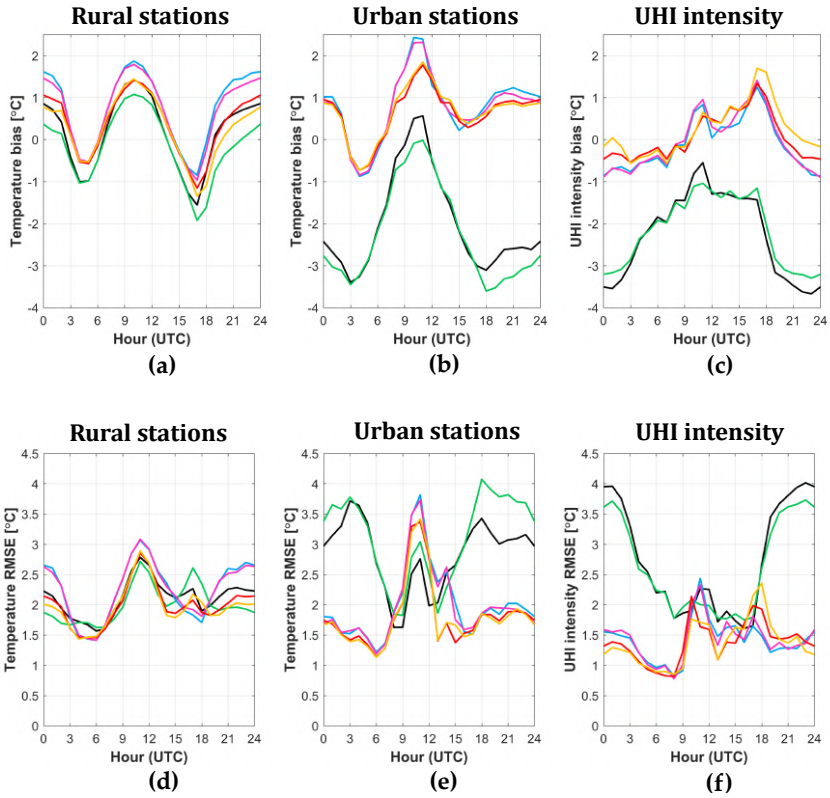

Figure C.5: Moscow domain, Russia: mean biases and root-mean square errors of T2m, evaluated over rural **(a,d)** and urban **(b,e)** Roshydromet weather stations in the Moscow study area; mean biases and root-mean square errors of UHI intensity for urban weather stations **(c,f)**.

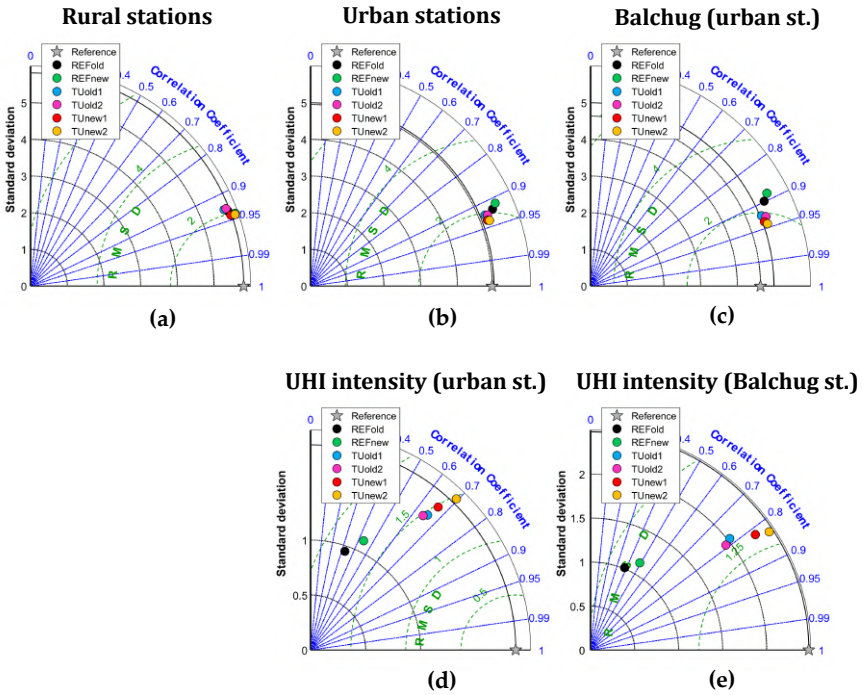

Figure C.6: Moscow domain, Russia: Taylor diagrams for 2-m temperature for rural **(a)**, urban **(b)** weather stations and Balchug weather station in the city center **(c)**, and for UHI intensity for urban weather stations **(d)** and for Balchug weather station in the city center **(e)**.

D

Appendix D: Supplementary material for Chapter 4

Figure D.1 shows the temperature, vertical velocity and heat flux fields for the three-dimensional (3D) free-slip cases. Panels e-f of Fig. D.1 show the spectra of the vertical velocity found for both the 3D no-slip and free-slip cases. Figures D.2 and D.3 show the horizontal power spectra of the kinetic energy, computed over the times $\tau_{conv} = 180 \div 220$ and for each case of the 3D no-slip and free-slip boundary conditions. Note that the kinetic energy spectrum of the case $k_b = 0.25$ exhibits a clear second (exogenous) peak at $k = 0.25$, both under no-slip and free slip conditions (see Fig. D.2-D.3). However, this is not due to convective motions (in fact this second peak is very low in the corresponding spectrum of the vertical velocity field $W(k)$, see Fig. D.1e-f), but to the horizontal velocities u and v. Near-boundary horizontal sections of the velocity fields (taken near the boundary layer at the bottom plate, at $z = 0.1$) exhibit structures that are correlated with the thermal boundary conditions and the exogenous scale clearly emerges, as shown in Fig. D.4.

In the 2D domain ($L = 32\pi$), the vertical sections corresponding to the whole fluid column (from $z = 0$ to $z = 1$) are plotted in Fig. D.5. For both the velocity conditions, the most representative cases are selected: $k_b = 0, 1, 2, 3, 6$ (no-slip) and $k_b = 0, 0.25, 0.5, 4$ (free-slip).

Figures D.6 and D.7 show the horizontal power spectra of the kinetic energy for all cases analyzed in 2D.

Figure D.8 shows the time-series of the Nusselt number for 3D and 2D simulations.

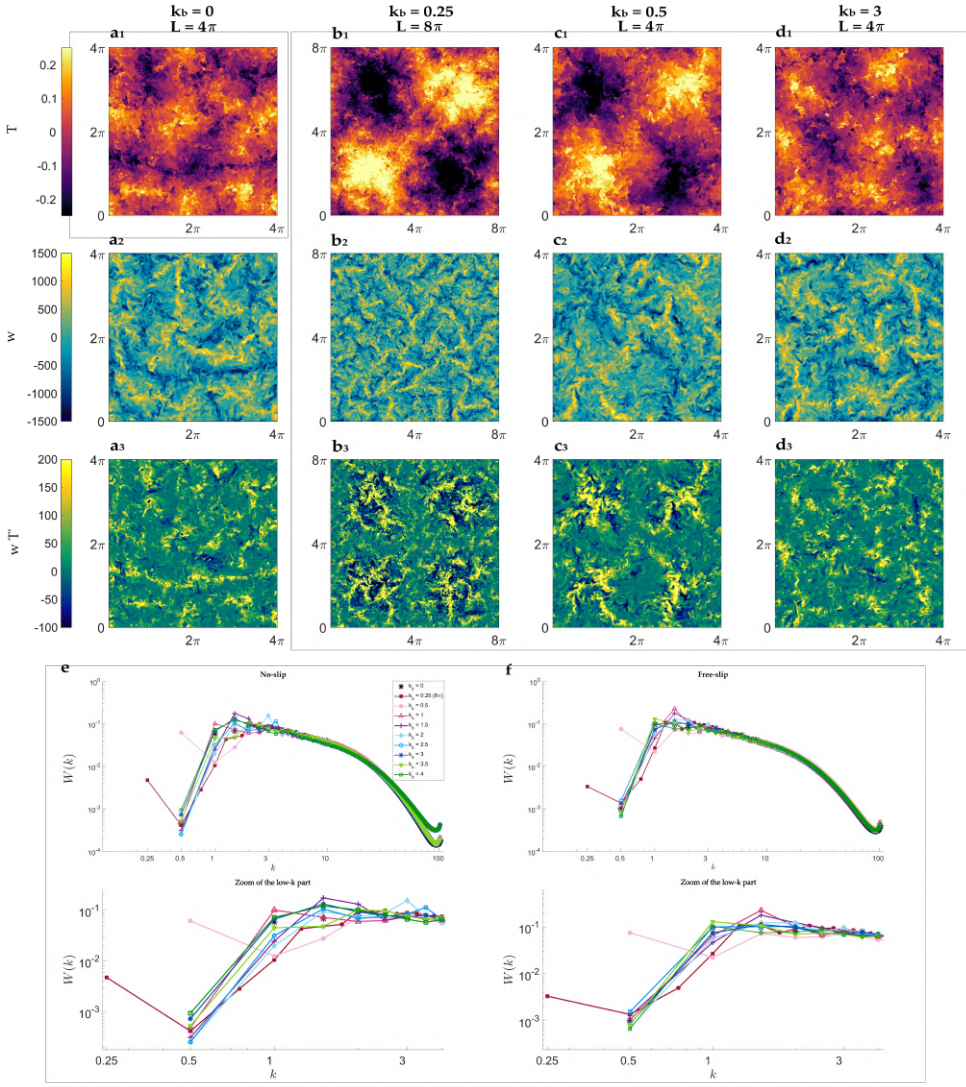

Figure D.1: 3D simulations, free-slip conditions: horizontal slices (at $z = 1/2$ and $\tau_{conv} = 180$) of the temperature perturbations T (first row, subscript 1), vertical velocity field w (second row, subscript 2) and vertical flux wT' (third row, subscript 3), for the cases $k_b = 0$ ($\mathbf{a_{1-3}}$), $k_b = 0.25$ and $L = 8\pi$ ($\mathbf{b_{1-3}}$), $k_b = 0.5$ ($\mathbf{c_{1-3}}$) and $k_b = 3$ ($\mathbf{d_{1-3}}$). Panels **e** and **f**: spectra (averaged over the vertical fluid column and times $\tau_{conv} = 180 \div 220$) of the no-slip (**e**) and free-slip (**f**) vertical velocity field $W(k)$, plotted as functions of the horizontal wave number k (for each one, also a zoom of the low-k part is shown). The benchmark case ($k_b = 0$) is marked with black asterisks.

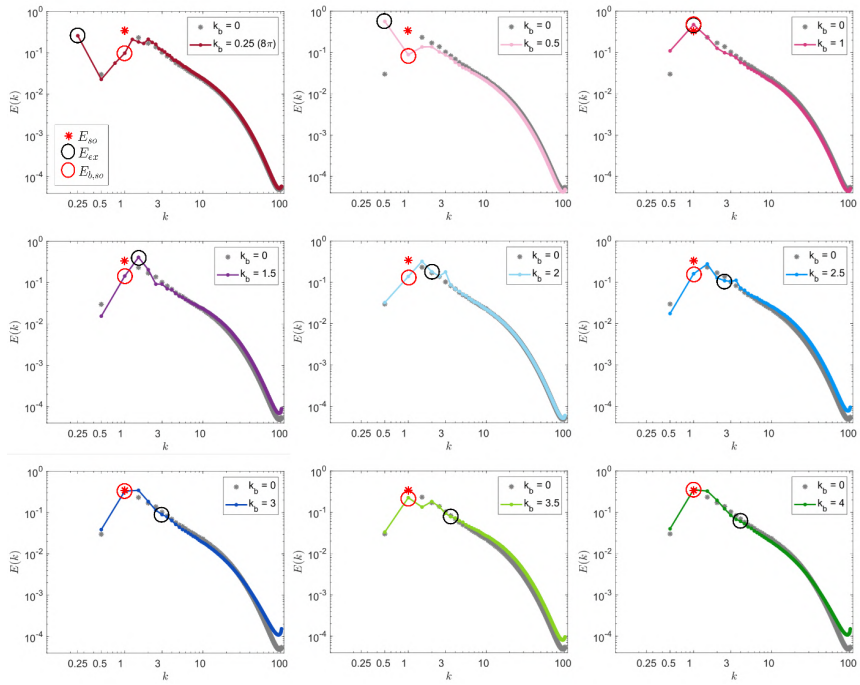

Figure D.2: 3D simulations: horizontal power spectra of the NO-SLIP kinetic energy $E(k)$. Each spectrum is averaged over the vertical fluid column and times $\tau_{conv} = 180 \div 220$ and is plotted as function of the horizontal wave number k. The spectrum for the homogeneous case ($k_b = 0$) is shown with gray asterisks for reference. The spectral values E_{so}, E_{ex} and $E_{(b,so)}$ are marked with a red asterisk, a black and a red circle, respectively.

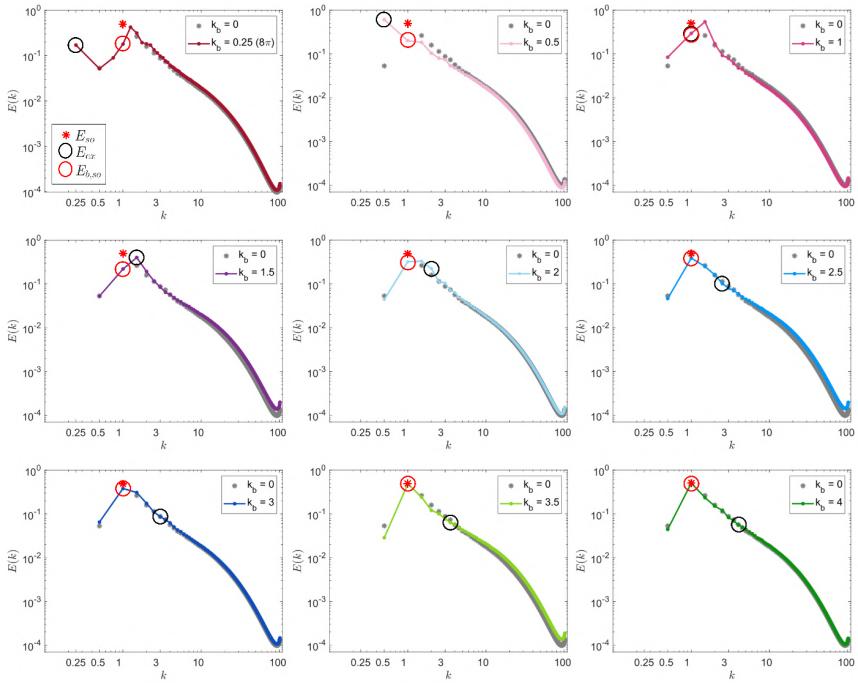

Figure D.3: 3D simulations: horizontal power spectra of the FREE-SLIP kinetic energy $E(k)$, averaged over the vertical fluid column and times $\tau_{conv} = 180 \div 220$. Symbols are as in caption of Fig. D.2.

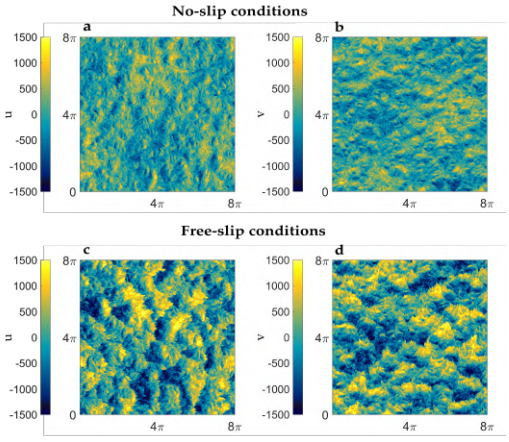

Figure D.4: 3D simulations: near-boundary slices at $\tau_{conv} = 180$ and $z = 0.1$ of the horizontal velocity components u (panels **a** and **c**) and v (panels **b** and **d**), under no- and free-slip boundary conditions (case $k_b = 0.25$ and $L = 8\pi$).

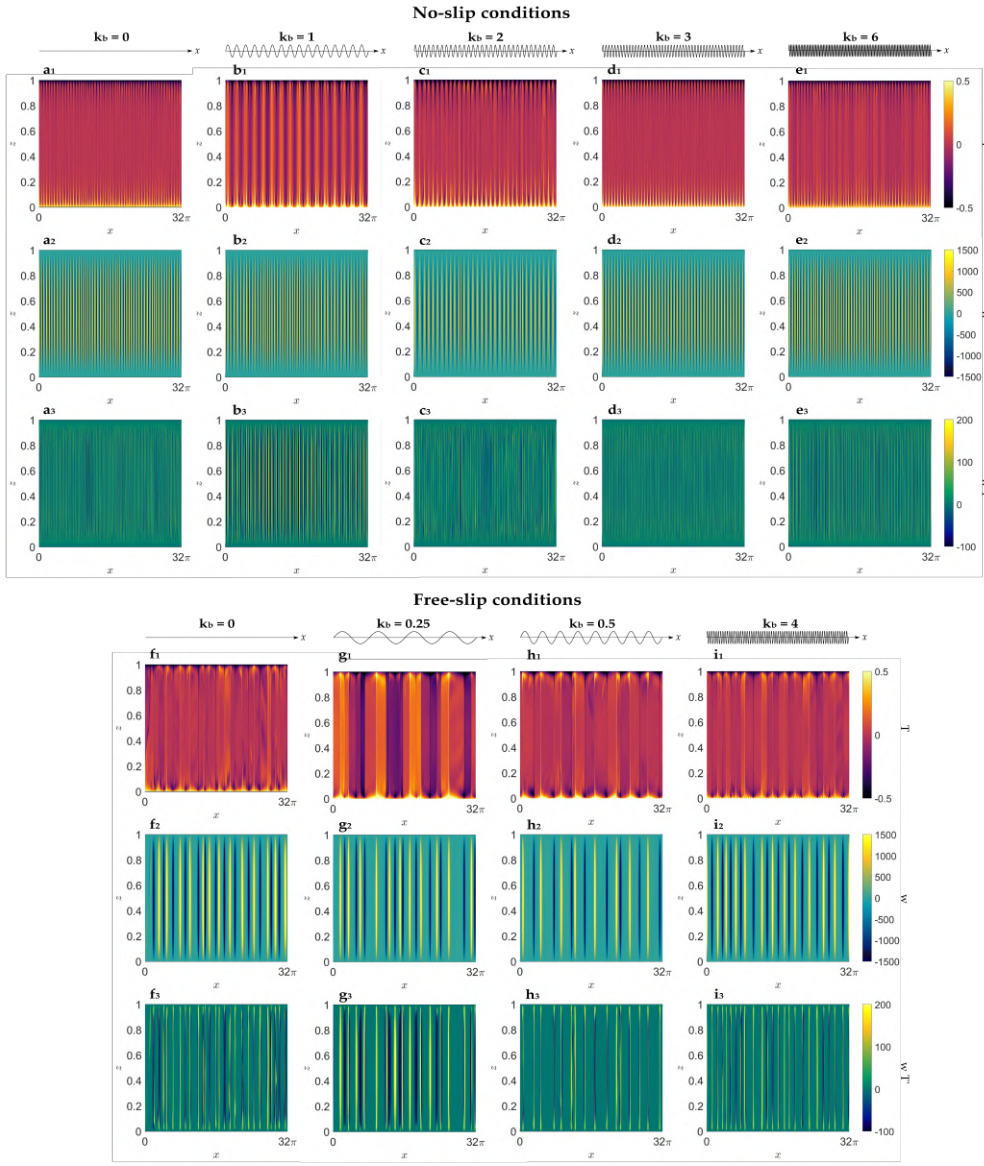

Figure D.5: Vertical slices of the 2D domain at $\tau_{conv} = 180$ of the temperature perturbations T (subscript 1), the vertical velocity field w (subscript 2) and the vertical flux wT' (subscript 3), for the no-slip cases $k_b = 0$ ($\mathbf{a_{1-3}}$), $k_b = 1$ ($\mathbf{b_{1-3}}$), $k_b = 2$ ($\mathbf{c_{1-3}}$), $k_b = 3$ ($\mathbf{d_{1-3}}$) and $k_b = 6$ ($\mathbf{e_{1-3}}$), and for the free-slip $k_b = 0$ ($\mathbf{f_{1-3}}$), $k_b = 0.25$ ($\mathbf{g_{1-3}}$), $k_b = 0.5$ ($\mathbf{h_{1-3}}$) and $k_b = 4$ ($\mathbf{i_{1-3}}$). A representation of the temperature boundary perturbations is shown above the temperature panels.

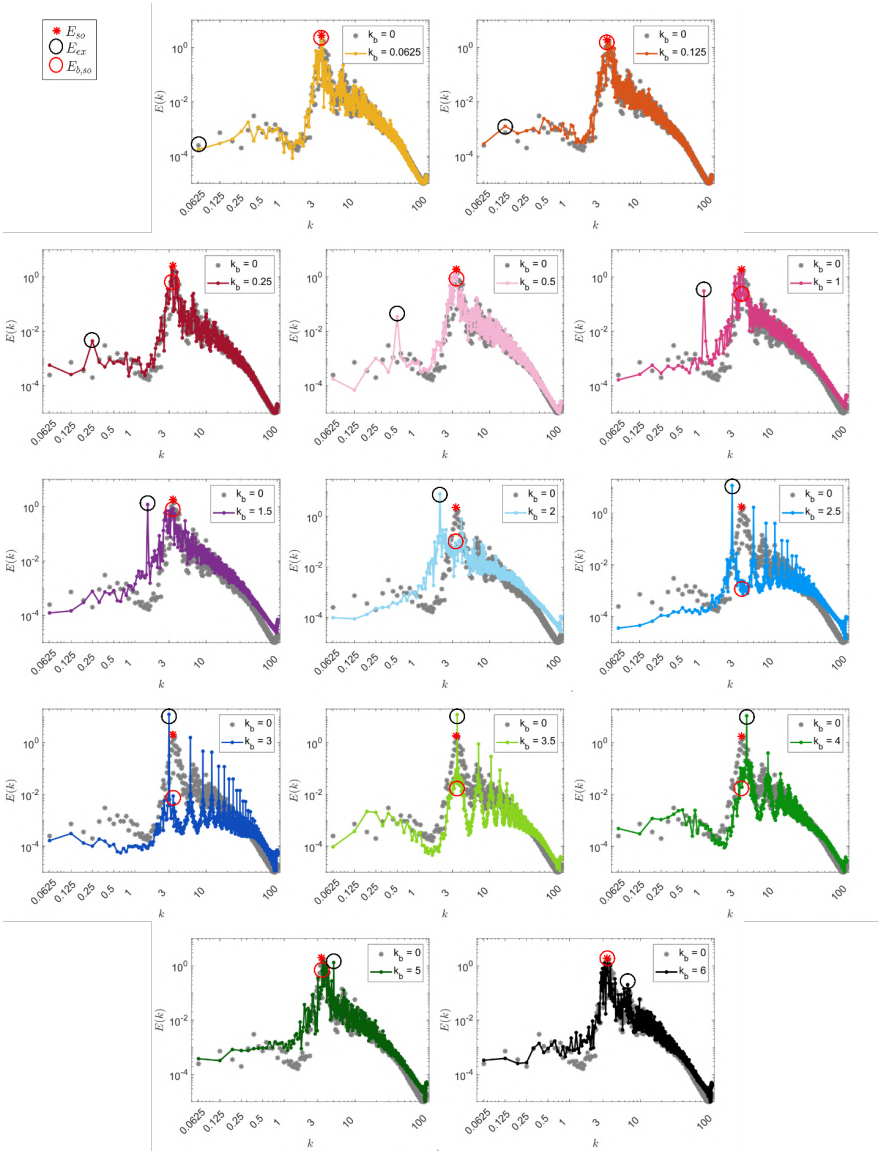

Figure D.6: No-slip 2D kinetic energy spectra, averaged over the vertical fluid column and times $\tau_{conv} = 180 \div 220$. The spectral values E_{so}, E_{ex} and $E_{(b,so)}$ are marked with a red asterisk, a black and a red circle, respectively.

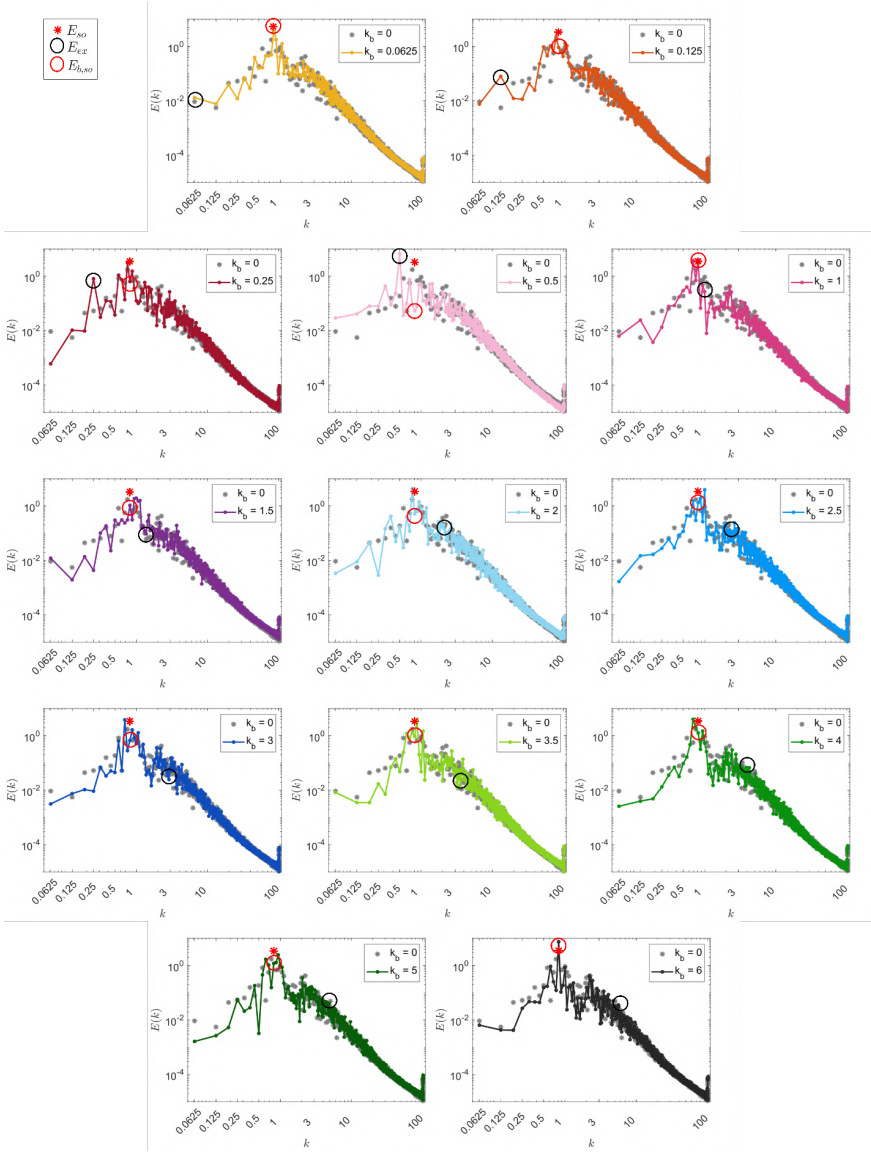

Figure D.7: Free-slip 2D kinetic energy spectra, averaged over the vertical fluid column and times $\tau_{conv} = 180 \div 220$. Symbols are as in caption of Fig. D.6.

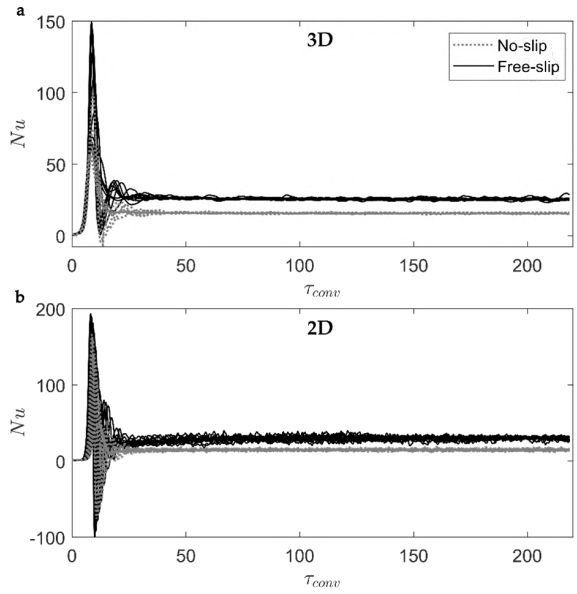

Figure D.8: Time-series of the volume-averaged Nusselt number Nu for 3D (panel **a**) and 2D (panel **b**) simulations.

References

1. Emanuel, K. A. *et al. Atmospheric convection* (Oxford University Press on Demand, 1994).
2. Storey, B. D., Zaltzman, B. & Rubinstein, I. Bulk electroconvective instability at high Péclet numbers. *Physical Review E* **76,** 041501 (2007).
3. Bejan, A. *Convection heat transfer* (John wiley & sons, 2013).
4. Spiegel, E. A. Convection in stars: I. Basic Boussinesq convection. *Annual Review of Astronomy and Astrophysics* **9,** 323 (1971).
5. Kippenhahn, R., Weigert, A. & Weiss, A. *Stellar structure and evolution* (Springer, 1990).
6. Busse, F. H. Convection driven zonal flows and vortices in the major planets. *Chaos: An Interdisciplinary Journal of Nonlinear Science* **4,** 123–134 (1994).
7. Miesch, M. S. The coupling of solar convection and rotation (invited review). *Helioseismic Diagnostics of Solar Convection and Activity,* 59–89 (2000).
8. Fearn, D. R. & Loper, D. E. Compositional convection and stratification of Earth's core. *Nature* **289,** 393–394 (1981).
9. Calkins, M. A., Noir, J., Eldredge, J. D. & Aurnou, J. M. The effects of boundary topography on convection in Earth's core. *Geophysical Journal International* **189,** 799–814 (2012).
10. Glatzmaier, G. A., Coe, R. S., Hongre, L. & Roberts, P. H. The role of the Earth's mantle in controlling the frequency of geomagnetic reversals. *Nature* **401,** 885–890 (1999).
11. Schubert, G., Turcotte, D. L. & Olson, P. *Mantle convection in the Earth and planets* (Cambridge University Press, 2001).
12. Marshall, J. & Schott, F. Open-ocean convection: Observations, theory, and models. *Reviews of Geophysics* **37,** 1–64 (1999).
13. Rahmstorf, S. Thermohaline circulation: The current climate. *Nature* **421,** 699–699 (2003).
14. Wallace, J. M. & Hobbs, P. V. *Atmospheric science: an introductory survey* (Elsevier, 2006).
15. Garratt, J. R. The atmospheric boundary layer. *Earth-Science Reviews* **37,** 89–134 (1994).
16. Stull, R. B. *An introduction to boundary layer meteorology* (Springer Science & Business Media, 1988).
17. Trenberth, K. E., Fasullo, J. T. & Shepherd, T. G. Attribution of climate extreme events. *Nature Climate Change* **5,** 725–730 (2015).
18. Nield, D. General heterogeneity effects on the onset of convection in a porous medium. *Emerging Topics in Heat and Mass Transfer in Porous Media,* 63–84 (2008).
19. Nield, D. A., Bejan, A., *et al. Convection in porous media* (Springer, 2006).
20. Richards, M. A. & Engebretson, D. C. Large-scale mantle convection and the history of subduction. *Nature* **355,** 437–440 (1992).
21. Davies, G. F. & Richards, M. A. Mantle convection. *The Journal of Geology* **100,** 151–206 (1992).
22. Sumita, I. & Olson, P. A laboratory model for convection in Earth's core driven by a thermally heterogeneous mantle. *Science* **286,** 1547–1549 (1999).

23. Zipser, E. J. & Liu, C. Extreme Convection vs. Extreme Rainfall: a Global View. *Current Climate Change Reports,* 1–10 (2022).

24. Li, H. *et al.* Development of a new forced convection heat transfer correlation for CO2 in both heating and cooling modes at supercritical pressures. *International Journal of Thermal Sciences* **50,** 2430–2442 (2011).

25. Nemati, H., Patel, A., Boersma, B. J. & Pecnik, R. The effect of thermal boundary conditions on forced convection heat transfer to fluids at supercritical pressure. *Journal of Fluid Mechanics* **800,** 531–556 (2016).

26. United Nations, Department of Economic and Social Affairs, Population Division. *World Urbanization Prospects 2018: The 2018 Revision (ST/ESA/SER.A/420)* (New York: United Nations, 2019).

27. Oke, T. R., Mills, G., Christen, A. & Voogt, J. A. *Urban Climates* (Cambridge University Press, 2017).

28. Howard, L. *The climate of London: deduced from meteorological observations made in the metropolis and at various places around it* (Harvey, Darton, J., and A. Arch, Longman, Hatchard, S. Highley [and] R. Hunter, 1833).

29. Lin, P., Lau, S. S. Y., Qin, H. & Gou, Z. Effects of urban planning indicators on urban heat island: a case study of pocket parks in high-rise high-density environment. *Landscape and Urban Planning* **168,** 48–60 (2017).

30. Li, X., Stringer, L. C., Chapman, S. & Dallimer, M. How urbanisation alters the intensity of the urban heat island in a tropical African city. *PLoS one* **16,** e0254371 (2021).

31. Jamei, Y., Rajagopalan, P. & Sun, Q. C. Spatial structure of surface urban heat island and its relationship with vegetation and built-up areas in Melbourne, Australia. *Science of the Total Environment* **659,** 1335–1351 (2019).

32. Touchaei, A. & Wang, Y. Characterizing urban heat island in Montreal (Canada)–Effect of urban morphology. *Sustainable Cities and Society* **19,** 395–402 (2015).

33. Kolokotroni, M. & Giridharan, R. Urban heat island intensity in London: An investigation of the impact of physical characteristics on changes in outdoor air temperature during summer. *Solar Energy* **82,** 986–998 (2008).

34. Oke, T. R. City size and the urban heat island. *Atmospheric Environment (1967)* **7,** 769–779 (1973).

35. Stewart, I. D. A systematic review and scientific critique of methodology in modern urban heat island literature. *International Journal of Climatology* **31,** 200–217 (2011).

36. Kim, S. W. & Brown, R. D. Urban heat island (UHI) intensity and magnitude estimations: A systematic literature review. *Science of the Total Environment,* 146389 (2021).

37. Lord Rayleigh. LIX. On convection currents in a horizontal layer of fluid, when the higher temperature is on the under side. *Philosophical Magazine* **32,** 529–546 (1916).

38. Avsec, D. *Tourbillons thermoconvectifs dans l'air* PhD thesis (Université de Paris, 1939).

39. Lappa, M. *Thermal convection: patterns, evolution and stability* (John Wiley & Sons, 2009).

40. Pandey, A., Scheel, J. D. & Schumacher, J. Turbulent superstructures in Rayleigh-Bénard convection. *Nature Communications* **9,** 1–11 (2018).

41. Parodi, A., von Hardenberg, J., Passoni, G., Provenzale, A. & Spiegel, E. A. Clustering of plumes in turbulent convection. *Physical Review Letters* **92,** 194503 (2004).

42. *Consortium for Small-scale Modeling (COSMO)* `http://www.cosmo-model.org/`.

43. **Bassani, F.**, Garbero, V., Poggi, D., Ridolfi, L., von Hardenberg, J. & Milelli, M. An innovative approach to select urban-rural sites for Urban Heat Island analysis: the case of Turin (Italy). *Urban Climate* **42,** 101099 (2022).

44. Landsberg, H. E. *The urban climate* (Academic press, 1981).

45. Tzavali, A., Paravantis, J. P., Mihalakakou, G., Fotiadi, A. & Stigka, E. Urban heat island intensity: A literature review. *Fresenius Environmental Bulletin* **24,** 4537–4554 (2015).

46. Arnfield, A. J. Two decades of urban climate research: a review of turbulence, exchanges of energy and water, and the urban heat island. *International Journal of Climatology: a Journal of the Royal Meteorological Society* **23,** 1–26 (2003).

47. Oke, T. R. The distinction between canopy and boundary-layer urban heat islands. *Atmosphere* **14,** 268–277 (1976).

48. Rizwan, A. M., Dennis, L. Y. & Chunho, L. A review on the generation, determination and mitigation of Urban Heat Island. *Journal of Environmental Sciences* **20,** 120–128 (2008).

49. Hoffmann, P. & Schlünzen, K. H. Weather pattern classification to represent the urban heat island in present and future climate. *Journal of Applied Meteorology and Climatology* **52,** 2699–2714 (2013).

50. Stewart, I. D. Landscape representation and the urban-rural dichotomy in empirical urban heat island literature, 1950–2006. *Acta Climatologica et Chorologica* **40,** 111–121 (2007).

51. Karl, T. R., Knight, R. W. & Plummer, N. Trends in high-frequency climate variability in the twentieth century. *Nature* **377,** 217–220 (1995).

52. Gough, W. Theoretical considerations of day-to-day temperature variability applied to Toronto and Calgary, Canada data. *Theoretical and Applied Climatology* **94,** 97–105 (2008).

53. Mohsin, T. & Gough, W. A. Characterization and estimation of urban heat island at Toronto: impact of the choice of rural sites. *Theoretical and Applied Climatology* **108,** 105–117 (2012).

54. Tam, B. Y., Gough, W. A. & Mohsin, T. The impact of urbanization and the urban heat island effect on day to day temperature variation. *Urban Climate* **12,** 1–10 (2015).

55. Wu, F.-T., Fu, C., Qian, Y., Gao, Y. & Wang, S.-Y. High-frequency daily temperature variability in China and its relationship to large-scale circulation. *International Journal of Climatology* **37,** 570–582 (2017).

56. Anderson, C. I., Gough, W. A. & Mohsin, T. Characterization of the urban heat island at Toronto: Revisiting the choice of rural sites using a measure of day-to-day variation. *Urban Climate* **25,** 187–195 (2018).

57. Milelli, M. Urban heat island effects over Torino. *COSMO Newsletter* **16,** 1–10 (2016).

58. Gough, W. A. Thermal signatures of peri-urban landscapes. *Journal of Applied Meteorology and Climatology* **59,** 1443–1452 (2020).

59. Stewart, I. D. & Oke, T. R. Local climate zones for urban temperature studies. *Bulletin of the American Meteorological Society* **93,** 1879–1900 (2012).

60. Jolliffe, I. T. & Cadima, J. Principal component analysis: a review and recent developments. *Philosophical Transactions of the Royal Society A: Mathematical, Physical and Engineering Sciences* **374,** 20150202 (2016).

61. Jolliffe, I. T. *Principal Component Analysis* (Springer New York, 2002).

62. Wilks, D. S. *Statistical methods in the atmospheric sciences* (Academic press, 2011).

63. Lorenz, E. N. Empirical orthogonal functions and statistical weather prediction (1956).

64. Hannachi, A., Jolliffe, I. T. & Stephenson, D. B. Empirical orthogonal functions and related techniques in atmospheric science: A review. *International Journal of Climatology: A Journal of the Royal Meteorological Society* **27,** 1119–1152 (2007).

65. Demšar, U., Harris, P., Brunsdon, C., Fotheringham, A. S. & McLoone, S. Principal component analysis on spatial data: an overview. *Annals of the Association of American Geographers* **103,** 106–128 (2013).

66. Demuzere, M., Bechtel, B., Middel, A. & Mills, G. *European LCZ map* `https://urlsand.esvalabs.com/?u=https%3A%2F%2Ffigshare.com%2Farticles%2Fdataset%2FEuropean_LCZ_map%2F13322450%2F1&e=78898b00&h=9a0f73a7&f=y&p=n`. [Online; accessed 15-June-2021]. 2020.

67. Ching, J. *et al.* WUDAPT: An urban weather, climate, and environmental modeling infrastructure for the anthropocene. *Bulletin of the American Meteorological Society* **99,** 1907–1924 (2018).

68. Köppen, W. & Geiger, R. Das geographische System der Klimate Handbuch der Klimatologie. *Ed. W. Köppen and R. Geiger* **1** (1936).

69. Demuzere, M., Bechtel, B., Middel, A. & Mills, G. Mapping Europe into local climate zones. *PloS one* **14,** e0214474 (2019).

70. Memon, R. A., Leung, D. Y. & Liu, C.-H. An investigation of urban heat island intensity (UHII) as an indicator of urban heating. *Atmospheric Research* **94,** 491–500 (2009).

71. Theeuwes, N. E., Steeneveld, G.-J., Ronda, R. J., Rotach, W. M. & Holtslag, A. A. Cool city mornings by urban heat. *Environmental Research Letters* **10** (2015).

72. Theeuwes, N. E., Steeneveld, G.-J., Ronda, R. J. & Holtslag, A. A. A diagnostic equation for the daily maximum urban heat island effect for cities in northwestern Europe. *International Journal of Climatology* **37,** 443–454 (2017).

73. Garbero, V., Milelli, M, Bucchignani, E., Mercogliano, P., Varentsov, M., Rozinkina, I., Rivin, G, Blinov, D., Wouters, H., Schulz, J.-P., Schättler, U., **Bassani, F.**, Demuzere, M. & Repola, F. Evaluating the urban canopy scheme TERRA_URB in the COSMO model for selected European cities. *Atmosphere* **12,** 237 (2021).

74. Oke, T. R. The energetic basis of the urban heat island. *Quarterly Journal of the Royal Meteorological Society* **108,** 1–24 (1982).

75. Johnson, D. Urban modification of diurnal temperature cycles in Birmingham, UK. *Journal of Climatology* **5,** 221–225 (1985).

76. Cassardo, C. *et al. The Urban Meteorological Station of Turin* in *11ˆ th Symposium on Acoustic Remote Sensing* (2002), 311–320.

77. Arpa Piemonte. *Annual Climatic Report (in Italian)* `https://www.arpa.piemonte.it/rischinaturali/tematismi/clima/rapporti-di-analisi/annuale.html`. [Online; accessed 22-November-2021]. 2020.

78. Rosenzweig, C. *et al.* Characterizing the urban heat island in current and future climates in New Jersey. *Global Environmental Change Part B: Environmental Hazards* **6,** 51–62 (2005).

79. Parker, D. E. Urban heat island effects on estimates of observed climate change. *Wiley Interdisciplinary Reviews: Climate Change* **1,** 123–133 (2010).

80. Founda, D. & Santamouris, M. Synergies between Urban Heat Island and Heat Waves in Athens (Greece), during an extremely hot summer (2012). *Scientific Reports* **7,** 1–11 (2017).

81. Giridharan, R. & Kolokotroni, M. Urban heat island characteristics in London during winter. *Solar Energy* **83,** 1668–1682 (2009).

82. Tan, J. *et al.* The urban heat island and its impact on heat waves and human health in Shanghai. *International Journal of Biometeorology* **54,** 75–84 (2010).

83. Santamouris, M. Heat island research in Europe: the state of the art. *Advances in Building Energy Research* **1,** 123–150 (2007).

84. Oh, J. W., Ngarambe, J., Duhirwe, P. N., Yun, G. Y. & Santamouris, M. Using deep-learning to forecast the magnitude and characteristics of urban heat island in Seoul Korea. *Scientific Reports* **10,** 1–13 (2020).

85. Pakarnseree, R., Chunkao, K. & Bualert, S. Physical characteristics of Bangkok and its urban heat island phenomenon. *Building and Environment* **143,** 561–569 (2018).

86. Oke, T. R. Canyon geometry and the nocturnal urban heat island: comparison of scale model and field observations. *Journal of Climatology* **1,** 237–254 (1981).

87. Milelli, M., **Bassani, F.**, Garbero, V., Poggi, D., von Hardenberg, J. & Ridolfi, L. Characterization of the Urban Heat and Dry Island effects in the Turin metropolitan area. *Urban Climate* **47,** 101397 (2023).

88. Gabriel, K. M. & Endlicher, W. R. Urban and rural mortality rates during heat waves in Berlin and Brandenburg, Germany. *Environmental Pollution* **159,** 2044–2050 (2011).

89. United Nations, Department of Economic and Social Affairs, Population Division. *World Urbanization Prospects: The 2018 Revision (ST/ESA/SER.A/420)* (New York: United Nations, 2019).

90. Deilami, K., Kamruzzaman, M. & Liu, Y. Urban heat island effect: A systematic review of spatio-temporal factors, data, methods, and mitigation measures. *International Journal of Applied Earth Observation and Geoinformation* **67,** 30–42 (2018).

91. Steeneveld, G. J., Koopmans, S., Heusinkveld, B. G., van Hove, L. W. A. & Holtslag, A. A. M. Quantifying urban heat island effects and human comfort for cities of variable size and urban morphology in the Netherlands. *Journal of Geophysical Research: Atmospheres* **116** (2011).

92. Liu, W., You, H. & Dou, J. Urban-rural humidity and temperature differences in the Beijing area. *Theoretical and Applied Climatology* **96,** 201–207 (May 2009).

93. Moriwaki, R., Watanabe, K. & Morimoto, K. Urban dry island phenomenon and its impact on cloud base level. *Journal of JSCE* **1,** 521–529 (2013).

94. Sundborg, A. Local Climatological Studies of the Temperature Conditions in an Urban Area. *Tellus* **2,** 222–232 (1950).

95. Chandler, T. J. London's urban climate. *The Geographical Journal* **128,** 279–298 (1962).

96. Bonacquisti, V., Casale, G., Palmieri, S. & Siani, A. A canopy layer model and its application to Rome. *Science of the Total Environment* **364,** 1–13 (2006).

97. Santamouris, M. Analyzing the heat island magnitude and characteristics in one hundred Asian and Australian cities and regions. *Science of the Total Environment* **512,** 582–598 (2015).

98. Zhang, X., Steeneveld, G.-J., Zhou, D., Duan, C. & Holtslag, A. A. A diagnostic equation for the maximum urban heat island effect of a typical Chinese city: A case study for Xi'an. *Building and Environment* **158,** 39–50 (2019).

99. Rotach, M. *et al.* BUBBLE - An urban boundary layer meteorology project. *Theoretical and Applied Climatology* **81,** 231–261 (July 2005).

100. Changnon, S. *METROMEX: A Review and Summary* ISBN: 9781935704294. `https://books.google.it/books?id=SaXCDAAAQBAJ` (American Meteorological Society, 2016).

101. Leach, M. *Final Report for the Joint Urban 2003 Atmospheric Dispersion Study in Oklahoma City: Lawrence Livermore National Laboratory participation* (University of North Texas Libraries, 2005).

102. Colacino, M. & Lavagnini, A. Evidence of the urban heat island in Rome by climatological analyses. *Archives for meteorology, geophysics, and bioclimatology, Series B* **31,** 87–97 (1982).

103. Zinzi, M., Carnielo, E. & Mattoni, B. On the relation between urban climate and energy performance of buildings. A three-years experience in Rome, Italy. *Applied Energy* **221,** 148–160 (2018).

104. Guattari, C., Evangelisti, L. & Balaras, C. A. On the assessment of urban heat island phenomenon and its effects on building energy performance: A case study of Rome (Italy). *Energy and Buildings* **158,** 605–615 (2018).

105. Di Sabatino, S., Barbano, F., Brattich, E. & Pulvirenti, B. The Multiple-Scale Nature of Urban Heat Island and Its Footprint on Air Quality in Real Urban Environment. *Atmosphere* **11.** ISSN: 2073-4433. `https://www.mdpi.com/2073-4433/11/11/1186` (2020).

106. Busato, F., Lazzarin, R. M. & Noro, M. Three years of study of the Urban Heat Island in Padua: Experimental results. *Sustainable Cities and Society* **10,** 251–258 (2014).

107. Petralli, M. *et al.* Role of green areas in Urban Heat Island mitigation: a case study in Florence (Italy). *Rivista Italiana di Agrometeorologia* **1** (Jan. 2006).

108. Bacci, P. & Maugeri, M. The urban heat island of Milan. *Il Nuovo Cimento C* **15,** 417–424 (1992).

109. Martinelli, A., Kolokotsa, D.-D. & Fiorito, F. Urban heat island in Mediterranean coastal cities: The case of Bari (Italy). *Climate* **8,** 79 (2020).

110. Garzena, D., Acquaotta, F. & Fratianni, S. Analysis of the long-time climate data series for Turin and assessment of the city's urban heat island. *Weather* **74,** 353–359 (2019).

111. Dell'Anna, F., Bravi, M., Marmolejo-Duarte, C., Bottero, M. C. & Chen, A. EPC Green Premium in Two Different European Climate Zones: A Comparative Study between Barcelona and Turin. *Sustainability* **11.** ISSN: 2071-1050. `https://www.mdpi.com/2071-1050/11/20/5605` (2019).

112. Kadygrov, E. N., Ganshin, E. V., Miller, E. A. & Tochilkina, T. A. Ground-based microwave temperature profilers: Potential and experimental data. *Atmospheric and Oceanic Optics* **28,** 598–605 (2015).

113. Welch, B. L. The generalization of 'STUDENT'S'problem when several different population varlances are involved. *Biometrika* **34,** 28–35 (1947).

114. Simona, F., Cassardo, C. & Cremonini, R. Climatic characterization of Föhn episodes in Piedmont, Italy. *Geografia Fisica e Dinamica Quaternaria* **32** (Jan. 2009).

115. Flamant, C. *et al.* Föhn/cold-pool interactions in the Rhine valley during MAP IOP 15. *Quarterly Journal of the Royal Meteorological Society* **132,** 3035–3058 (2006).

116. Ketzler, G. The diurnal temperature cycle and its relation to boundary-layer structure during the morning transition. *Boundary-Layer Meteorology* **151,** 335–351 (2014).

117. Chow, W. T. & Svoma, B. M. Analyses of nocturnal temperature cooling-rate response to historical local-scale urban land-use/land cover change. *Journal of Applied Meteorology and Climatology* **50,** 1872–1883 (2011).

118. Gaffin, S., Rosenzweig, C. & Khanbilvardi, R. e. a. Variations in New York city's urban heat island strength over time and space. *Theoretical and Applied Climatology* **94,** 1–11 (2008).

119. Camilloni, I. & Barrucand, M. Temporal variability of the Buenos Aires, Argentina, urban heat island. *Theoretical and Applied Climatology* **107,** 47–58 (2011).

120. Cuadrat, J. M., Vicente-Serrano, S. & Saz, M. A. Influence of different factors on relative air humidity in Zaragoza, Spain. *Frontiers in Earth Science* **3,** 10. ISSN: 2296-6463. `https://www.frontiersin.org/article/10.3389/feart.2015.00010` (2015).

121. Ping, Y., Ren, G., Pengcheng, Y. & Jingmian, D. Tempo-spatial Pattern of Wind Speed and Urban Stilling Island in Beijing City. *Journal of Meteorological Research* **34,** 597 (Aug. 2020).

122. Wang, X. & Gong, Y. The impact of an urban dry island on the summer heat wave and sultry weather in Beijing City. *Chinese Science Bulletin* **55,** 1657–1661 (2010).

123. Hilberg, S. Diurnal temperature and moisture cycles. *Summary of METROMEX* **2,** 25–42 (1978).

124. Lee, D. O. Urban—rural humidity differences in London. *International Journal of Climatology* **11,** 577–582. https://rmets.onlinelibrary.wiley.com/doi/abs/10.1002/joc.3370110509 (1991).

125. Montávez, J. P., Rodríguez, A. & Jiménez, J. I. A study of the urban heat island of Granada. *International Journal of Climatology: A Journal of the Royal Meteorological Society* **20,** 899–911 (2000).

126. Giannaros, T. M. & Melas, D. Study of the urban heat island in a coastal Mediterranean City: The case study of Thessaloniki, Greece. *Atmospheric Research* **118,** 103–120. ISSN: 0169-8095. https://www.sciencedirect.com/science/article/pii/S0169809512001810 (2012).

127. Morris, C. J. G., Simmonds, I. & Plummer, N. Quantification of the Influences of Wind and Cloud on the Nocturnal Urban Heat Island of a Large City. *Journal of Applied Meteorology* **40,** 169–182 (2001).

128. Oke, T. in *Wind climate in cities* 81–107 (Springer, 1995).

129. Hidalgo, J., Masson, V., Baklanov, A., Pigeon, G. & Gimeno, L. Advances in Urban Climate Modeling. *Annals of the New York Academy of Sciences* **1146,** 354–374 (2008).

130. Kamardin, A. P., Gladkikh, V. A., Nevzorova, I. V. & Odintsov, S. L. *"Cold lens" above an urban heat island in the atmospheric boundary layer* in *27th International Symposium on Atmospheric and Ocean Optics, Atmospheric Physics* (eds Matvienko, G. G. & Romanovskii, O. A.) **11916** (SPIE, 2021), 1134–1140. https://doi.org/10.1117/12.2602473.

131. Duckworth, F. S. & Sandberg, J. S. The effect of cities upon horizontal and vertical temperature gradients. *Bulletin of the American Meteorological Society* **35,** 198–207 (1954).

132. Bornstein, R. D. Observations of the urban heat island effect in New York City. *Journal of Applied Meteorology and Climatology* **7,** 575–582 (1968).

133. Lokoshchenko, M. *et al.* Vertical Extension of the Urban Heat Island above Moscow. *Doklady Earth Sciences* **466,** 70–74 (Jan. 2016).

134. Varentsov, M., Wouters, H., Platonov, V. & Konstantinov, P. Megacity-Induced Mesoclimatic Effects in the Lower Atmosphere: A Modeling Study for Multiple Summers over Moscow, Russia. *Atmosphere* **9.** ISSN: 2073-4433. https://www.mdpi.com/2073-4433/9/2/50 (2018).

135. Sparks, N. & Toumi, R. Numerical simulations of daytime temperature and humidity crossover effects in London. *Boundary-Layer Meteorology* **154,** 101–117 (2015).

136. Bucchignani, E. *et al. Analysis and Evaluation of TERRA_URB Scheme: PT AEVUS Final Report. Technical Report No. 40.* http://www.cosmo-model.org/content/model/documentation/techReports/docs/techReport40.pdf. 2019.

137. Reba, M. & Seto, K. C. A systematic review and assessment of algorithms to detect, characterize, and monitor urban land change. *Remote Sensing of Environment* **242,** 111739 (2020).

138. Pachauri, R. *et al.* AR5 Synthesis Report: Climate Change 2014—IPCC (Synthesis Report No. 5). *The Intergovernmental Panel on Climate Change: Geneva, Switzerland* (2014).

139. Koffi, B. & Koffi, E. Heat waves across Europe by the end of the 21st century: multiregional climate simulations. *Climate Research* **36,** 153–168 (2008).

140. Schatz, J. & Kucharik, C. J. Urban climate effects on extreme temperatures in Madison, Wisconsin, USA. *Environmental Research Letters* **10,** 094024 (2015).

141. De Ridder, K. *et al.* Urban heat island intensification during hot spells—The case of Paris during the summer of 2003. *Urban Science* **1,** 3 (2016).

142. Konstantinov, P. I., Varentsov, M. & Malinina, E. Modeling of thermal comfort conditions inside the urban boundary layer during Moscow's 2010 summer heat wave (case-study). *Urban Climate* **10,** 563–572 (2014).

143. Van Hove, L. *et al.* Temporal and spatial variability of urban heat island and thermal comfort within the Rotterdam agglomeration. *Building and Environment* **83,** 91–103 (2015).

144. Tan, J. *et al.* The urban heat island and its impact on heat waves and human health in Shanghai. *International Journal of Biometeorology* **54,** 75–84 (2010).

145. Lo, Y. E. *et al.* UK climate projections: Summer daytime and nighttime urban heat island changes in England's major cities. *Journal of Climate* **33,** 9015–9030 (2020).

146. Wouters, H. *et al.* Heat stress increase under climate change twice as large in cities as in rural areas: A study for a densely populated midlatitude maritime region. *Geophysical Research Letters* **44,** 8997–9007 (2017).

147. Zhao, L. *et al.* Global multi-model projections of local urban climates. *Nature Climate Change* **11,** 152–157 (2021).

148. Mote, T. L., Lacke, M. C. & Shepherd, J. M. Radar signatures of the urban effect on precipitation distribution: A case study for Atlanta, Georgia. *Geophysical Research Letters* **34** (2007).

149. Baik, J.-J., Kim, Y.-H., Kim, J.-J. & Han, J.-Y. Effects of boundary-layer stability on urban heat island-induced circulation. *Theoretical and Applied Climatology* **89,** 73–81 (2007).

150. Li, Y. *et al.* Strong intensification of hourly rainfall extremes by urbanization. *Geophysical Research Letters* **47,** e2020GL088758 (2020).

151. Doan, Q.-V. *et al.* Urban-induced modifications to the diurnal cycle of rainfall over a tropical city. *Quarterly Journal of the Royal Meteorological Society* **147,** 1189–1201 (2021).

152. Dou, J., Wang, Y., Bornstein, R. & Miao, S. Observed spatial characteristics of Beijing urban climate impacts on summer thunderstorms. *Journal of Applied Meteorology and Climatology* **54,** 94–105 (2015).

153. Dimitrova, R. *et al.* Modeling the impact of urbanization on local meteorological conditions in Sofia. *Atmosphere* **10,** 366 (2019).

154. Martilli, A., Roth, M., Chow, W. T., *et al.* Summer average urban-rural surface temperature differences do not indicate the need for urban heat reduction (2020).

155. Zhou, D. *et al.* Satellite remote sensing of surface urban heat islands: Progress, challenges, and perspectives. *Remote Sensing* **11,** 48 (2018).

156. Garuma, G. F. Review of urban surface parameterizations for numerical climate models. *Urban Climate* **24,** 830–851 (2018).

157. Chen, F. *et al.* The integrated WRF/urban modelling system: development, evaluation, and applications to urban environmental problems. *International Journal of Climatology* **31,** 273–288 (2011).

158. Sharma, A. *et al.* Urban meteorological modeling using WRF: a sensitivity study. *International Journal of Climatology* **37,** 1885–1900 (2017).

159. Baklanov, A. *et al.* On the parameterisation of the urban atmospheric sublayer in meteorological models. *Atmospheric Chemistry and Physics Discussions* **5,** 12119–12176 (2005).

160. Baklanov, A. *et al.* Towards improving the simulation of meteorological fields in urban areas through updated/advanced surface fluxes description. *Atmospheric Chemistry and Physics* **8,** 523–543 (2008).

161. Bohnenstengel, S., Evans, S., Clark, P. A. & Belcher, S. Simulations of the London urban heat island. *Quarterly Journal of the Royal Meteorological Society* **137,** 1625–1640 (2011).

162. Iriza, A., Dumitrache, R. & Stefan, S. Numerical modelling of the Bucharest urban heat island with the WRF-urban system. *Romanian Journal of Physics* **62,** 1–14 (2017).

163. Vogel, J. & Afshari, A. Comparison of urban heat island intensity estimation methods using urbanized WRF in Berlin, Germany. *Atmosphere* **11,** 1338 (2020).

164. Ribeiro, I., Martilli, A., Falls, M., Zonato, A. & Villalba, G. Highly resolved WRF-BEP/BEM simulations over Barcelona urban area with LCZ. *Atmospheric Research* **248,** 105220 (2021).

165. Doms, G. *et al.* A description of the nonhydrostatic regional COSMO model. *Part II: Physical Parameterization* **154** (2011).

166. Wouters, H. *et al.* The efficient urban canopy dependency parametrization (SURY) v1. 0 for atmospheric modelling: description and application with the COSMO-CLM model for a Belgian summer. *Geoscientific Model Development* **9,** 3027–3054 (2016).

167. Bohnenstengel, S., Hamilton, I., Davies, M. & Belcher, S. Impact of anthropogenic heat emissions on London's temperatures. *Quarterly Journal of the Royal Meteorological Society* **140,** 687–698 (2014).

168. Varentsov, M., Wouters, H., Platonov, V. & Konstantinov, P. Megacity-induced mesoclimatic effects in the lower atmosphere: A modeling study for multiple summers over Moscow, Russia. *Atmosphere* **9,** 50 (2018).

169. Varentsov, M., Grishchenko, M. & Wouters, H. *Simultaneous Assessment of the Summer Urban Heat Island in Moscow Megacity Based on in Situ Observations, Thermal Satellite Images and Mesoscale Modeling* `https://ges.rgo.ru/jour/article/view/903`. 2019.

170. Rivin, G. *et al.* The system for numerical prediction of weather events (including severe ones) for Moscow megacity: The prototype development. *Russian Meteorology and Hydrology* **44,** 729–738 (2019).

171. Rivin, G. *et al.* Development of the high-resolution operational system for numerical prediction of weather and severe weather events for the Moscow region. *Russian Meteorology and Hydrology* **45,** 455–465 (2020).

172. Wouters, H., Demuzere, M., De Ridder, K. & van Lipzig, N. P. The impact of impervious water-storage parametrization on urban climate modelling. *Urban Climate* **11,** 24–50 (2015).

173. Demuzere, M. *et al.* Impact of urban canopy models and external parameters on the modelled urban energy balance in a tropical city. *Quarterly Journal of the Royal Meteorological Society* **143,** 1581–1596 (2017).

174. Trusilova, K. *et al.* The urban land use in the COSMO-CLM model: a comparison of three parameterizations for Berlin (2016).

175. Brousse, O. *et al.* Using Local Climate Zones in Sub-Saharan Africa to Tackle Urban Health Issues. *Urban Climate* **27,** 227–242 (2019).

176. Brousse, O. *et al.* The Local Climate Impact of an African City during Clear-Sky Conditions—Implications of the Recent Urbanization in Kampala (Uganda). *International Journal of Climatology* **40,** 4586–4608 (2020).

177. Trusilova, K. *et al.* Implementation of an urban parameterization scheme into the regional climate model COSMO-CLM. *Journal of Applied Meteorology and Climatology* **52,** 2296–2311 (2013).

178. Mussetti, G. *et al.* Simulating urban climate at sub-kilometre scale for representing the intra-urban variability of Zurich, Switzerland. *International Journal of Climatology* **40,** 458–476 (2020).

179. Li, Y., Schubert, S., Kropp, J. P. & Rybski, D. On the influence of density and morphology on the Urban Heat Island intensity. *Nature Communications* **11,** 1–9 (2020).

180. Mussetti, G. *et al.* COSMO-BEP-Tree v1. 0: a coupled urban climate model with explicit representation of street trees. *Geoscientific Model Development* **13,** 1685–1710 (2020).

181. Schubert, S., Grossman-Clarke, S. & Martilli, A. A double-canyon radiation scheme for multi-layer urban canopy models. *Boundary-Layer Meteorology* **145,** 439–468 (2012).

182. Steppeler, J. *et al.* Meso-gamma scale forecasts using the nonhydrostatic model LM. *Meteorology and Atmospheric Physics* **82,** 75–96 (2003).

183. Baldauf, M. *et al.* Operational convective-scale numerical weather prediction with the COSMO model: Description and sensitivities. *Monthly Weather Review* **139,** 3887–3905 (2011).

184. Buzzi, M. *Challenges in operational numerical weather prediction at high resolution in complex terrain* PhD thesis (ETH Zurich, 2008).

185. Paulson, C. A. The mathematical representation of wind speed and temperature profiles in the unstable atmospheric surface layer. *Journal of Applied Meteorology and Climatology* **9,** 857–861 (1970).

186. Guo, X. & Zhang, H. A performance comparison between nonlinear similarity functions in bulk parameterization for very stable conditions. *Environmental Fluid Mechanics* **7,** 239–257 (2007).

187. Louis, J.-F. A parametric model of vertical eddy fluxes in the atmosphere. *Boundary-Layer Meteorology* **17,** 187–202 (1979).

188. Wouters, H., De Ridder, K. & van Lipzig, N. P. Comprehensive parametrization of surface-layer transfer coefficients for use in atmospheric numerical models. *Boundary-Layer Meteorology* **145,** 539–550 (2012).

189. Mellor, G. L. & Yamada, T. Development of a turbulence closure model for geophysical fluid problems. *Reviews of Geophysics* **20,** 851–875 (1982).

190. Schättler, U., Doms, G. & Schraff, C. A Description of the Nonhydrostatic Regional COSMO-Model. Part VII: User's Guide. *Deutscher Wetterdienst* **226** (2018).

191. Schulz, J.-P. Introducing sub-grid scale orographic effects in the COSMO model. *COSMO Newsletter* **9,** 29–36 (2008).

192. Cerenzia, I., Tampieri, F. & Tesini, M. S. Diagnosis of turbulence schema in stable atmospheric conditions and sensitivity tests. *COSMO Newsletter* **14,** 1–11 (2014).

193. Varentsov, M., Samsonov, T., Kislov, A. & Konstantinov, P. Simulations of Moscow agglomeration heat island within the framework of the regional climate model Cosmo-CLM. *Vestnik Moskovskogo universiteta. Seriya 5, Geografiya,* 25–37 (2018).

194. Schulz, J.-P., Vogel, G., Becker, C., Kothe, S. & Ahrens, B. *Evaluation of the ground heat flux simulated by a multi-layer land surface scheme using high-quality observations at grass land and bare soil* in *EGU General Assembly Conference Abstracts* (2015), 6549.

195. Schulz, J.-P. & Vogel, G. Improving the processes in the land surface scheme TERRA: Bare soil evaporation and skin temperature. *Atmosphere* **11,** 513 (2020).

196. Viterbo, P. & Beljaars, A. C. An improved land surface parameterization scheme in the ECMWF model and its validation. *Journal of Climate* **8,** 2716–2748 (1995).

197. Flanner, M. G. Integrating anthropogenic heat flux with global climate models. *Geophysical Research Letters* **36** (2009).

198. Asensio, H., Messmer, M., Luthi, D., Osterried, K. & Jucker, J. *External Parameters for Numerical Weather Prediction and Climate Application EXTPAR v5_4, User and Implementation Guide.* `http://www.cosmo-model.org/content/support/software/ethz/EXTPAR_user_and_implementation_manual.pdf`. [Online; accessed 05-August-2022]. 2020.

199. Elvidge, C. D. *et al.* Global distribution and density of constructed impervious surfaces. *Sensors* **7,** 1962–1979 (2007).

200. European Environment Agency. *EEA Fast Track Service Precursor on Land Monitoring—Degree of Soil Sealing.* `https://www.eea.europa.eu/data-and-maps/data/eea-fast-track-service-precursor-on-land-monitoring-degree-of-soil-sealing`. [Online; accessed 05-August-2022].

201. Bicheron, P. *et al. Globcover: products description and validation report* 2008.

202. Kislov, A., Varentsov, M. & Tarasova, L. Role of spring soil moisture in the formation of large-scale droughts in the East European Plain in 2002 and 2010. *Izvestiya, Atmospheric and Oceanic Physics* **51,** 405–411 (2015).

203. Canadell, J. *et al.* Maximum rooting depth of vegetation types at the global scale. *Oecologia* **108,** 583–595 (1996).

204. Persson, H. & Baitulin, I. O. *Plant root systems and natural vegetation* in (1996).

205. Schenk, H. J. & Jackson, R. B. The global biogeography of roots. *Ecological Monographs* **72,** 311–328 (2002).

206. Akkermans, T. *et al.* Validation and comparison of two soil-vegetation-atmosphere transfer models for tropical Africa. *Journal of Geophysical Research: Biogeosciences* **117** (2012).

207. Varentsov, M., Samsonov, T. & Demuzere, M. Impact of urban canopy parameters on a megacity's modelled thermal environment. *Atmosphere* **11,** 1349 (2020).

208. Stewart, I. D. & Kennedy, C. A. Metabolic heat production by human and animal populations in cities. *International Journal of Biometeorology* **61,** 1159–1171 (2017).

209. Samsonov, T. & Varentsov, M. Computation of city-descriptive parameters for high-resolution numerical weather prediction in Moscow megacity in the framework of the COSMO model. *Russian Meteorology and Hydrology* **45,** 515–521 (2020).

210. Lokoshchenko, M. Urban 'heat island' in Moscow. *Urban Climate* **10,** 550–562 (2014).

211. **Bassani, F.**, Poggi, D., Ridolfi, L. & von Hardenberg, J. Rayleigh-Bénard convection with thermal boundary inhomogeneities. *Physical Review E* **105,** 025108 (2022).

212. Siggia, E. D. High Rayleigh number convection. *Annual Review of Fluid Mechanics* **26,** 137–168 (1994).

213. Getling, A. V. & Spiegel, E. A. Rayleigh-Bénard convection: structures and dynamics. *Physics Today* **52,** 59 (1999).

214. Bodenschatz, E., Pesch, W. & Ahlers, G. Recent developments in Rayleigh-Bénard convection. *Annual Review of Fluid Mechanics* **32,** 709–778 (2000).

215. Ahlers, G., Grossmann, S. & Lohse, D. Heat transfer and large scale dynamics in turbulent Rayleigh-Bénard convection. *Reviews of Modern Physics* **81,** 503 (2009).

216. Lohse, D. & Xia, K.-Q. Small-scale properties of turbulent Rayleigh-Bénard convection. *Annual Review of Fluid Mechanics* **42,** 335–364 (2010).

217. Chillà, F. & Schumacher, J. New perspectives in turbulent Rayleigh-Bénard convection. *European Physical Journal E* **35,** 1–25 (2012).

218. Chandrasekhar, S. *Hydrodynamic and hydromagnetic stability* (Courier Corporation, 2013).

219. Goluskin, D. *Internally heated convection and Rayleigh-Bénard convection* (Springer, 2016).

220. Shishkina, O. Rayleigh-Bénard convection: The container shape matters. *Physical Review Fluids* **6,** 090502 (2021).

221. Jaupart, C. & Mareschal, J.-C. in *Treatise on Geophysics (Second Edition)* (ed Schubert, G.) Second, 217–253 (Elsevier, Oxford, 2015). ISBN: 978-0-444-53803-1. `https://www.sciencedirect.com/science/article/pii/B9780444538024001147`.

222. Wang, F., Huang, S.-D. & Xia, K.-Q. Thermal convection with mixed thermal boundary conditions: effects of insulating lids at the top. *Journal of Fluid Mechanics* **817,** R1 (2017).

223. Maykut, G. A. Large-scale heat exchange and ice production in the central Arctic. *Journal of Geophysical Research: Oceans* **87,** 7971–7984 (1982).

224. Wang, Z., Calzavarini, E., Sun, C. & Toschi, F. How the growth of ice depends on the fluid dynamics underneath. *Proceedings of the National Academy of Sciences* **118** (2021).

225. Zhao, L., Lee, X., Smith, R. B. & Oleson, K. Strong contributions of local background climate to urban heat islands. *Nature* **511,** 216–219 (2014).

226. Ripesi, P., Biferale, L., Sbragaglia, M. & Wirth, A. Natural convection with mixed insulating and conducting boundary conditions: low- and high-Rayleigh-number regimes. *Journal of Fluid Mechanics* **742,** 636–663 (2014).

227. Bakhuis, D., Ostilla-Mónico, R., Van Der Poel, E. P., Verzicco, R. & Lohse, D. Mixed insulating and conducting thermal boundary conditions in Rayleigh–Bénard convection. *Journal of Fluid Mechanics* **835,** 491–511 (2018).

228. Ostilla-Mónico, R. & Amritkar, A. Regime crossover in Rayleigh-Bénard convection with mixed boundary conditions. *Journal of Fluid Mechanics* **903,** 39 (2020).

229. Vasiliev, A. & Sukhanovskii, A. Turbulent convection in a cube with mixed thermal boundary conditions: low Rayleigh number regime. *International Journal of Heat and Mass Transfer* **174,** 121290 (2021).

230. Kelly, R. & Pal, D. Thermal convection with spatially periodic boundary conditions: resonant wavelength excitation. *Journal of Fluid Mechanics* **86,** 433–456 (1978).

231. Yoo, J.-S. & Kim, M.-U. Two-dimensional convection in a horizontal fluid layer with spatially periodic boundary temperatures. *Fluid Dynamics Research* **7,** 181 (1991).

232. Hartlep, T., Tilgner, A. & Busse, F. H. Large scale structures in Rayleigh-Bénard convection at high Rayleigh numbers. *Physical Review Letters* **91,** 064501 (2003).

233. Von Hardenberg, J., Parodi, A., Passoni, G., Provenzale, A. & Spiegel, E. Large-scale patterns in Rayleigh-Bénard convection. *Physics Letters A* **372,** 2223–2229 (2008).

234. Stevens, R. J., Blass, A., Zhu, X., Verzicco, R. & Lohse, D. Turbulent thermal superstructures in Rayleigh-Bénard convection. *Physical Review Fluids* **3,** 041501 (2018).

235. Krug, D., Lohse, D. & Stevens, R. Coherence of temperature and velocity superstructures in turbulent Rayleigh–Bénard flow. *Journal of Fluid Mechanics* **887** (Mar. 2020).

236. Passoni, G., Alfonsi, G. & Galbiati, M. Analysis of hybrid algorithms for the Navier–Stokes equations with respect to hydrodynamic stability theory. *International Journal for Numerical Methods in Fluids* **38,** 1069–1089 (2002).

237. Von Hardenberg, J., Goluskin, D., Provenzale, A. & Spiegel, E. Generation of large-scale winds in horizontally anisotropic convection. *Physical Review Letters* **115,** 134501 (2015).

238. Von Hardenberg, J. *RBsolve: Pseudospectral Rayleigh-Bénard Solver*. `https://github.com/jhardenberg/rbsolve`.

239. *HPC@POLITO, a project of Academic Computing within the Department of Control and Computer Engineering at the Politecnico di Torino.* `http://www.hpc.polito.it`.

240. Wang, Q., Chong, K. L., Stevens, R. J., Verzicco, R. & Lohse, D. From zonal flow to convection rolls in Rayleigh–Bénard convection with free-slip plates. *Journal of Fluid Mechanics* **905** (2020).

241. Wang, Q., Verzicco, R., Lohse, D. & Shishkina, O. Multiple states in turbulent large-aspect-ratio thermal convection: What determines the number of convection rolls? *Physical Review Letters* **125,** 074501 (2020).

242. Hughes, G. O. & Griffiths, R. W. Horizontal convection. *Annual Review of Fluid Mechanics* **40,** 185–208 (2008).

243. Stern, M. *Ocean Circulation Physics* ISBN: 9780126667509. `https://books.google.it/books?id=0EqpnQEACAAJ` (Academic Press, 1975).

244. Griffiths, R. W., Hughes, G. O. & Gayen, B. Horizontal convection dynamics: insights from transient adjustment. *Journal of Fluid Mechanics* **726,** 559–595 (2013).

245. Rossby, H. *On thermal convection driven by non-uniform heating from below: an experimental study* in *Deep Sea Research and Oceanographic Abstracts* **12** (1965), 9–16.

246. Scotti, A. & White, B. Is horizontal convection really "non-turbulent?" *Geophysical Research Letters* **38** (2011).

247. Shishkina, O., Grossmann, S. & Lohse, D. Heat and momentum transport scalings in horizontal convection. *Geophysical Research Letters* **43,** 1219–1225 (2016).

248. Goluskin, D., Johnston, H., Flierl, G. R. & Spiegel, E. A. Convectively driven shear and decreased heat flux. *Journal of Fluid Mechanics* **759,** 360–385 (2014).

249. Van Der Poel, E. P., Ostilla-Mónico, R., Verzicco, R. & Lohse, D. Effect of velocity boundary conditions on the heat transfer and flow topology in two-dimensional Rayleigh-Bénard convection. *Physical Review E* **90,** 013017 (2014).

250. Demuzere, M. *WUDAPT-to-COSMO* `https://github.com/matthiasdemuzere/WUDAPT-to-COSMO/blob/eb4d232dbb56f712dd2b486cb555b5e3c3c209fb/utils.py#L290`. 2020.